Transport effects on coastal productivity and harmful algal blooms

Hally B. Stone

A dissertation
submitted in partial fulfillment of the
requirements for the degree of

Doctor of Philosophy

University of Washington
2020

Reading Committee:
Neil S. Banas, Chair
Parker MacCready
Evelyn J. Lessard

Program Authorized to Offer Degree:
Oceanography

University of Washington

Abstract

Transport effects on coastal productivity and harmful algal blooms

Hally B. Stone

Chairs of the Supervisory Committee:
Neil S. Banas
Oceanography
Parker MacCready
Oceanography

This dissertation examines the effect of transport on coastal productivity and harmful algal blooms in coastal upwelling systems in three parts, using the Pacific Northwest coastal ocean (also referred to as the Northern California Current System) and the greater California Current System (CCS) as a case study. These three studies utilize a combination of observations and model output. Chapter 2 investigates the effects of upwelling variability and large-scale advection on slope and shelf water properties in the Northern CCS using both Eulerian and Lagrangian analyses in a 7-year ROMS hindcast model. Results suggest that variability in the depth of the California Undercurrent as well as in alongshore local and remote wind stress are responsible for about 50% of shelf bottom water variability, and that the shelf and slope

experience similar large-scale alongcoast advection patterns. These results were then combined with observations of dissolved oxygen and dissolved inorganic carbon concentrations to approximate the relative effects of variability in upwelling and in large-scale advection on shelf and slope water properties. Next, in Chapter 3, we examine the relationship between phytoplankton productivity, wind patterns, and retention in the Northern and Central CCS using chlorophyll concentration and wind stress derived from satellite observations, as well as particle tracking experiments conducted in the same ROMS model. Results from this analysis suggest that while there is a dome-shaped relationship between mean chlorophyll concentration and wind stress for the whole system, the Central and Northern CCS have significantly different relationships. However, results from the particle tracking experiments suggest that the effect of wind intermittency on retention is minimal in the Northern CCS on a 1° latitude-wide scale. Lastly, we present a revised hypothesis to describe the relationship between chlorophyll concentration and wind stress in the CCS that includes the influence of non-upwelling-derived nutrients in the Northern CCS. Finally, in Chapter 4 we use similar particle tracking experiments combined with observations of *Pseudo-nitzschia* cells at Pacific Northwest coastal beaches and meridional wind stress to test whether the model reproduces the observed beaching patterns of *Pseudo-nitzschia* cells. With the goal of improving how the model is used to forecast beaching events, we test a suite of beaching criteria as well as two resolutions of the model. Results suggest that allowing for multiple coastal proximity events as well as using the loosest beaching criteria resulted in the most successfully simulated HAB events in the medium-resolution version of the model, and that the high-resolution version of the model performed best overall. All together, these three studies help elucidate the numerous effects that transport, both positive and negative, can have on the biology of the coastal ocean.

TABLE OF CONTENTS

LIST OF FIGURES

LIST OF TABLES

ACKNOWLEDGEMENTS

Thank you to my advisors, Neil Banas and Parker MacCready, without whom this work would not have been possible. Neil, thank you for choosing me as your first graduate student, for encouraging me to pursue my interests in non-academic career paths, and for generally just being an excellent mentor and advisor. I've really enjoyed learning from you and working with you these past seven years. Parker, thank you for taking me on as your student when Neil abandoned me for Scotland. I've really appreciated your encouragement, perspective, advice, and humor. I'm going to miss our not-so-science-y lab lunch meetings and discussions of which color map is truly the best.

Thank you to my committee members, past and present, for your guidance throughout my time in graduate school. I would especially like to thank Evelyn Lessard and Lorenz Hauser for serving on my doctoral supervisory committee. Thank you to all of the UW Oceanography staff, especially Su Tipple and David Darr, who made so much of this work possible. I would also like to thank the fellows of the IGERT Program on Ocean Change, a wonderfully welcoming community that expanded my support network outside of the School of Oceanography. Thank you in particular to Terrie Klinger for leading us and for all of your support over the years.

To all of the fantastic UW Oceanography graduate students, past and present – thanks for welcoming me into this awesome and supportive community and for making these past seven years so incredibly fun! I'm going to miss all of our First Fridays, tOAStERs, and BBTs. In particular, thank you to those who showed me the ropes, especially Anna McLaskey and Sarah Dewey, who is also one of my science policy buddies. Sarah, thank you for encouraging me to pursue the science policy path and always being my champion. Thank you to my other science policy buddy, Max Showalter, for going through all of the applications and interviews with me – I'm excited to continue working with you in DC!

Thank you to my officemates, Jake Steinberg and Elizabeth Brasseale, for the camaraderie in OSB 331B, as well as to our recent office neighbors, Katy Christensen and Sarah Ragen, in OSB 331A – you've been a welcome and fun addition to our little corner of OSB. Elizabeth, thank you in particular for being an officemate, lab mate, cohort-mate, and one of my best friends. Thank you to my lab mates, both in Seattle and in Glasgow, especially Erin Broatch and Elizabeth, for all of our conversations and community. To my 2013 cohort, especially Elizabeth, Jake, Shirley Leung, Marta Wolfshorndl, and Elisa Bonnin – it's been a long and fun road and it's been such a pleasure to go through graduate school with you. Thank you for all of the support, fun, and beers over the years. Also, thank you to Erik Fredrickson, who doesn't fit into any of these other categories, for being a friend-turned-classmate and for all of the homebrew and baked goods.

Thank you to my family, Wes, Cinda, Sam, and Taylor Stone, who have been incredibly supportive of all of my pursuits throughout my life, even when they take me far away from home. The countless phone calls and visits have made the trials of grad school so much more bearable. I also want to thank the Rutherfords, my new local family, who have been welcoming and supportive these past seven years – it's been really fun getting to know you.

Most importantly, thank you to my incredibly supportive partner, Garrett Rutherford. Thank you for fun adventures during our breaks from schooling, for listening to me debug MATLAB code and practice countless talks, and for all of the many other wonderful things. I can't wait to see what adventures we have in the future. Finally, I would be remiss if I didn't mention Benji and Peppa – thank you for your unconditional love and support.

DEDICATION

For Garrett, who’s been there through it all.

Chapter 1. INTRODUCTION

This dissertation explores some of the effects of transport on coastal productivity and harmful algal blooms within a coastal upwelling system. The research described in this dissertation uses the Pacific Northwest coastal ocean (also referred to as the Northern California Current System) and greater California Current System as its study region; however, many of these results may be generally applicable to other coastal upwelling systems. These systems are found worldwide and are known as Eastern Boundary Current (or Upwelling) Systems as they lie on the eastern boundary of ocean basins.

1.1 BACKGROUND

Like many Eastern Boundary Current Systems, the California Current System (CCS) is a highly productive region. In 2016, commercial and recreational fisheries supported 269,000 jobs and contributed $34.5 billion to the economies of Washington, Oregon, and California (National Marine Fisheries Service, 2017). All of these jobs and financial contributions are supported by the fisheries within the CCS, which in turn are fueled by the highly productive phytoplankton found along the coast.

The high productivity within the CCS is supported by coastal upwelling, a process through which nutrient-rich subsurface water is transported to the surface by wind. When wind blows southward over the ocean's surface, it induces Ekman transport offshore that in turn induces transport of deep, nutrient-rich water up to the surface over the shelf to fill the void (Huyer, 1983). This nutrient-rich water supports phytoplankton growth, with the wind's strength dictating how much of this nutrient-rich water is upwelled to the surface. In the Northern CCS, the upwelling mechanism is enhanced by the presence of canyons, which act as a funnel to allow for deeper, more nutrient-rich water to upwell at weaker wind strengths (Connolly & Hickey, 2014; Hickey, 1997). Additional nutrients to support the high productivity within the Northern CCS are supplied by outflow from the Salish Sea and river discharge (Davis et al., 2014; Hickey & Banas, 2008).

While transport, especially wind-driven Ekman transport, is generally good for phytoplankton and fisheries, it can also be bad for coastal fisheries. The West Coast often experiences harmful algal blooms of *Pseudo-nitzschia*, a diatom that sometimes produces a neurotoxin called domoic acid, that periodically close coastal beaches to fishing activities, such as clam digging and similar shellfish harvest (Trainer et al., 2012). These beach closures have significant, negative impacts on people whose livelihoods depend on commercial and recreational fisheries. For example, in Long Beach, Washington, the tourism industry surrounding razor clamming at local beaches is a crucial part of the local economy, so closures due to harmful algal blooms like the massive event in 2015 can significantly and negatively affect the economy of the entire town (Ritzman et al., 2018). Such events can be localized or widespread, with clusters of events followed by large gaps in the historical record, suggesting that these events are driven by large-scale ocean-atmosphere climate variability (McCabe et al., 2016; McKibben et al., 2017).

In addition to conveying harmful algal blooms to coastal beaches, transport of water masses can bring harmful water into the system. In the CCS, both acidic and hypoxic events have been linked to upwelling of low dissolved oxygen, nutrient- and carbon dioxide-rich water onto the shelf. These conditions have the potential to persist throughout the upwelling season, further exacerbated by local respiration of organic matter (e.g., Connolly et al. (2010); Feely et al. (2008); Grantham et al. (2004); Harris et al. (2013)). A cruise of the U.S. West Coast in 2007 mapping the depth of the aragonite saturation horizon found that it is moving closer to the ocean’s surface within the coastal ocean, even reaching the surface at times off the coast of Oregon (Feely et al., 2008). Below this horizon, organisms that build their bodies out of carbonate struggle to calcify. Continued acidification threatens lower trophic levels, like krill larvae, whose development is impaired under high concentration of carbon dioxide (McLaskey et al., 2016), as well as shellfish, as high-acidity events as short as 48 hours can be lethal to some shellfish larvae (Barton et al., 2012). Furthermore, the low dissolved oxygen that accompanies this acidic water also threatens biology. While fin fish and crustaceans can, to some extent, escape intrusions of hypoxic water, less mobile creatures like bivalves are usually unable to move away from these intrusions. The impact of hypoxia varies across organisms, but generally, oxygen concentrations of less than 0.5 mL/L result in mass mortality, with mortality beginning at concentrations below 1.0 mL/L (Diaz & Rosenberg, 1995). One such event resulted in a massive die-off of organisms, including economically-important organisms like rockfish and Dungeness crab (Grantham et al., 2004).

Lastly, large-scale transport of water masses can further affect coastal biology. This transport includes intrusions of northern water (Freeland et al., 2003; Kosro, 2003). In addition to being colder and fresher than the typical southern water found in the area, this northern water is more oxygenated and less acidic than southern water (Peterson et al., 2013). These intrusions of northern water via large-scale advection have also been known to transport different communities of zooplankton than are typically found in the region (Keister et al., 2011).

1.2 CHAPTER SUMMARIES

This dissertation addresses some of the effects of transport on coastal productivity and harmful algal blooms through three studies using a combination of observations and model output. In

Chapter 2, we use a comprehensive, well-validated regional model of the Northern CCS to investigate the effect of variability in alongcoast advection from the north and south and in the depth and composition of the California Undercurrent on mid-shelf bottom water properties using two approaches. First, an Eulerian analysis is used to characterize variability in mid-shelf bottom water properties and California Undercurrent depth and composition. Second, a Lagrangian analysis is used to characterize variability in water origin on the upper slope and adjacent shelf. Lastly, we extrapolate our findings to infer how variability in California Undercurrent depth and in alongcoast advection may affect oxygen and dissolved inorganic carbon variability in this region based on mean oxygen and dissolved inorganic carbon fields from other studies. A version of this chapter was originally published in the *Journal of Geophysical Research: Oceans* in 2018 (Stone et al., 2018).

In Chapter 3, we investigate the relationship between phytoplankton productivity, wind patterns, and retention in the Northern and Central CCS. First, we analyze the relationship between chlorophyll concentration and wind patterns using chlorophyll concentration and wind stress derived from satellite observations to see if the dome-shaped relationship described in Botsford et al. (2003) applies to the CCS as a whole and whether the Northern CCS is comparable or exhibits different behavior. Then, we investigate how retention affects the relationship between chlorophyll concentration and wind stress in the Northern CCS using results from particle tracking experiments conducted in the same regional model utilized in Chapter 2.

Lastly, Chapter 4 investigates the negative side of phytoplankton and transport to understand how species of *Pseudo-nitzschia*, a type of harmful algae, is transported to coastal beaches in the Pacific Northwest. In this chapter, we compare results from particle tracking experiments, conducted in the same regional model used in Chapter 2 and Chapter 3, with measurements of

Pseudo-nitzschia cell concentrations at beaches and wind stress observations to test whether the model reproduces the observed beaching patterns of *Pseudo-nitzschia* cells that originate in the Juan de Fuca eddy. As part of this analysis, we test various beaching criteria, as well as a higher-resolution model, to identify which criterion and model resolution produces results that best match observations and therefore are most appropriate to use in the forecasting model.

Chapter 2. THE EFFECT OF ALONGCOAST ADVECTION ON PACIFIC NORTHWEST SHELF AND SLOPE WATER PROPERTIES IN RELATION TO UPWELLING VARIABILITY

A version of this chapter was published by the *Journal of Geophysical Research: Oceans*.

Stone, H. B., Banas, N. S., & MacCready, P. (2018). The Effect of Alongcoast Advection on Pacific Northwest Shelf and Slope Water Properties in Relation to Upwelling Variability. *Journal of Geophysical Research: Oceans*, *123*(1), 265–286. https://doi.org/10.1002/2017JC013174

2.1 INTRODUCTION

In eastern boundary current upwelling systems like the California Current System (CCS), upwelled water is a significant source of nutrients for organisms on the continental shelf (e.g., Hickey and Banas (2003); MacFadyen et al. (2008)). Water upwelled onto CCS shelves is derived from the California Undercurrent (CUC), a warm, salty, low-oxygen, high-inorganic carbon, and high-nutrient poleward current (Hickey, 1979; MacFadyen et al., 2008; Pierce et al., 2000; Thomson & Krassovski, 2010). Changes in the equatorial sourcewaters of the CUC have been suggested to drive long-term trends in the composition of water upwelling onto the shelf in the CCS (Bograd et al., 2015; Meinvielle & Johnson, 2013). At the same time, a number of processes on regional and local scales have been observed or hypothesized to drive interannual variability in the water supplied to the shelf by upwelling, from local and remote wind-driven dynamics (e.g., Battisti and

Hickey (1984); Connolly et al. (2014); Hickey et al. (2006, 2016)) to large-scale alongcoast advection (e.g., Freeland et al. (2003); Kosro (2003)). This study uses a 7-year ROMS model hindcast to directly compare the effects of these processes in the Northern CCS (north of 42°N; NCCS): in particular, the effect of variability in the depth and composition of the CUC and in alongcoast advection on mid-shelf bottom water properties, in comparison with local and remote wind forcing, as well as an estimation of how these mechanisms may impact mid-shelf bottom water chemistry.

2.1.1 *Northern California Current System*

Large-scale circulation in the NCCS includes the California Current, the California Undercurrent, and the wintertime Davidson Current (Hickey, 1979). The California Current is an equatorward surface current, present year-round, that extends seaward about 1000 km from the shelf break. It is strongest at the surface, with a mean velocity of 10 cm s^{-1}, and offshore, it extends to about 500 m depth, and within 300 km of the coast, it extends to about 150 m (Hickey, 1979, 1989). The California Undercurrent (CUC) is a seasonal narrow (usually 10-20 km wide) subsurface current that flows poleward over the upper slope (core ~ 250 m depth) with mean poleward velocities of ~ 10 cm s^{-1}, which strengthens over the upwelling season (Hickey, 1979; Pierce et al., 2000; Thomson & Krassovski, 2010).

In the NCCS, upwelling, driven by equatorward alongshore winds, typically occurs during the summer into the fall and downwelling, driven by poleward alongshore winds, occurs in winter. Event-scale (several days) upwelling and downwelling can occur within each season. Both local and remote wind forcing drive upwelling and downwelling, with remote wind (alongshore winds at and south of about 42˚N) forcing playing a large role in upwelling due to the relatively weak local winds in the NCCS (Battisti & Hickey, 1984; Connolly et al., 2014; Hickey et al., 2006, 2016; Hickey & Banas, 2003). In particular, Battisti and Hickey (1984) show that off of Washington during the summer, over 35% of the energy in alongshelf currents generated from remote forcing originates between Cape Mendocino (40.4˚N) and San Francisco, California (37.8˚N), with the most energetic wind found at 39˚N.

During the upwelling season, equatorward winds drive Ekman transport offshore in the upper 10-30 m, and equatorward flow develops over the shelf (Hickey, 1989; Lentz, 1992). The water column interior experiences equatorward flow over much of the shelf, with poleward flow developing at depth over the outer shelf and mid-shelf as the upwelling season progresses (Hickey, 1989). The onshore return flow, compensating the offshore flow at the surface, occurs higher in the water column as the season progresses, while in the bottom boundary layer (bottom 5-15 m), flow is onshore in the beginning of the upwelling season, and weakens and transitions to offshore flow later in the season (Hickey, 1989; McCabe et al., 2015). This change in the direction of cross-shelf flow is a consequence of changing the sea level gradient from equatorward (lower sea level in the south) to poleward (higher sea level in the south; McCabe et al. (2015)). During the downwelling season, alongshore flow over the shelf is poleward. Northward winds push the surface Ekman transport onshore, while flow in the bottom boundary layer is offshore (Hickey, 1989).

Hickey et al. (2016) provides a thorough analysis of interannual variability and alongcoast structure of measured mid-shelf water properties in the NCCS from a suite of moored sensors deployed from 2000-2006. Results showed that while winter subsurface water properties on the shelf were strongly correlated with local winds, summer water properties were more strongly correlated with remote winds. Furthermore, Hickey et al. (2016) found that the alongcoast wind gradient can drive variability within the NCCS upwelling system. In particular, they link the unusually warm and fresh summer water properties observed in 2004 to the loss of the alongcoast wind gradient that year, as well as weaker remote and local winds, resulting in a shallower, warmer, and fresher CUC. The upwelling regime is further complicated by variable bathymetry, with enhanced upwelling through canyons, particularly in the northern-most portions of the NCCS (Alford & MacCready, 2014; Connolly & Hickey, 2014; Hickey, 1997).

2.1.2 *California Undercurrent*

As shown in previous studies (e.g., Hickey (1979); Pierce et al. (2000); Thomson and Krassovski (2010)) the CUC is a seasonal feature of the CCS, flowing over the continental slope between 150 – 300 m depth. The CUC originates in the equatorial Pacific, thus carrying with it warm and salty Pacific Equatorial Water (PEW; Hickey (1979); Pierce et al. (2000); Thomson and Krassovski (2010)). Thomson and Krassovski (2010) tracked the poleward extension of the CUC over several decades and found that in the NCCS it contains about 35-40% PEW. The CUC develops at the onset of the upwelling season, strengthening through the summer into the fall (Hickey, 1979). Once the winds transition to downwelling favorable in the winter, the CUC shoals and is replaced by or becomes the Davidson Current, the surface-intensified poleward flow over the slope (Hickey, 1979). The CUC is affected by coastal-trapped waves, which are driven by remote winds, the baroclinic component of the alongshore pressure gradient force, and sea level variability south of the NCCS (Connolly et al., 2014).

Variability in the CUC manifests in its depth, strength, and composition. In addition to its seasonal movement in the water column, the vertical position of the CUC has interannual and latitudinal variation (Thomson & Krassovski, 2010). The CUC's composition can change as it flows poleward losing heat and salt, the components of PEW, through along-isopycnal stirring in part due to anti-cyclonic eddies (cuddies) at CUC depth (Pelland et al., 2013; Pierce et al., 2000; Thomson & Krassovski, 2010). The composition can also vary interannually, such as the slightly fresher composition of the CUC observed in 2004 (Hickey et al., 2016).

2.1.3 *Alongcoast advection*

Variability in large-scale alongcoast advection may drive water property variability in the NCCS. Typically, water that upwells onto the shelf is from the CUC, which carries PEW from the south (e.g., MacFadyen et al. (2008)), though the source depth of water upwelled onto the shelf can vary both seasonally (typically shoaling throughout the upwelling season) and interannually (e.g., Chhak and Di Lorenzo (2007); Jacox et al. (2015); Di Lorenzo et al. (2008); Peterson et al. (2013)). However, occasional intrusions of subarctic water from the north onto the shelf in the NCCS have also been observed, bringing water that is colder and fresher than the typical summertime properties (Freeland et al., 2003; Grantham et al., 2004; Huyer, 2003; Kosro, 2003). Variations in transport on this scale are at least in part linked to modes of ocean-climate decadal variability, such as the North Pacific Gyre Oscillation (NPGO) and Pacific Decadal Oscillation (PDO). The NPGO is correlated with geostrophic transport in the North Pacific Current (Di Lorenzo et al., 2009), and Peterson et al. (2013) found the NPGO is a particularly strong predictor of hypoxia in the NCCS, attributing this link to changes in advection. The PDO is also correlated with anomalies in alongcoast advection that bring subarctic copepod communities into the NCCS during negative-PDO years and subtropical copepod communities during positive-PDO years (Keister et al., 2011), though a similar relationship between PDO and hypoxia in the NCCS was not found (Peterson et al., 2013).

This paper uses a comprehensive regional model of the NCCS developed by the University of Washington Coastal Modeling Group to investigate the effect of variability in the depth and composition of the CUC and in alongcoast advection from the north and south on mid-shelf bottom water properties. This model has been well validated with an extensive, multi-year observational dataset as part of the PNWTOX (Pacific Northwest Toxins) study (Davis et al., 2014; Giddings et al., 2014; Siedlecki et al., 2015). Compared to the recent observational study of interannual variability in mid-shelf water properties described in Hickey et al. (2016), the advantages of using a model to study water property variability is that both of the upper slope and shelf are sampled, the spatial resolution is higher, with 1.5 km resolution over the slope and shelf, and the model covers a somewhat longer time period (2003-2009). We will first use an Eulerian analysis to characterize variability in mid-shelf bottom water properties and CUC depth and composition, and then use Lagrangian analysis to characterize variability in water origin on the upper slope and adjacent shelf. Lastly, using mean oxygen and dissolved inorganic carbon (DIC) fields from other studies, we will extrapolate our findings to infer how variability in CUC depth and in alongcoast advection may affect oxygen and DIC variability in this region.

2.2 METHODS

2.2.1 *Model description and validation*

For this study, we used the Cascadia model developed by the University of Washington Coastal Modeling Group (Giddings et al., 2014; Sutherland et al., 2011). The model was implemented using ROMS (Regional Oceanic Modeling System: Shchepetkin and McWilliams (2005)), a free surface, hydrostatic, primitive equation model. The model domain (Figure 2.1) includes the Salish Sea and coastal ocean of Washington, northern Oregon, and southern British Columbia. The horizontal resolution of the model is 1.5 km over shelf and slope, expanding out to a maximum of 4.5 km offshore. Vertically, the model has 40 *S*-coordinate layers with stretching parameters set to better resolve the near-bottom and the upper water column. Ocean initial state and forcing on the southern and western boundaries were taken from the global Navy Coastal Ocean Model (NCOM; Barron et al. (2006, 2007)). Tides were specified by the quarter-degree TPXO7.2 inverse global tidal model (Egbert & Erofeeva, 2002). Rivers were forced by daily discharge data from the Columbia River, Fraser River, and 14 Puget Sound rivers using data from the USGS and Environment Canada (Giddings et al., 2014). All atmospheric forcing was derived from the fifth-generation Mesoscale Model (MM5) from Pennsylvania State University - National Center for Atmospheric Research (transitioning to the Weather Research and Forecasting model (WRF) in April 2008) regional atmospheric forecast model (Mass et al., 2003).

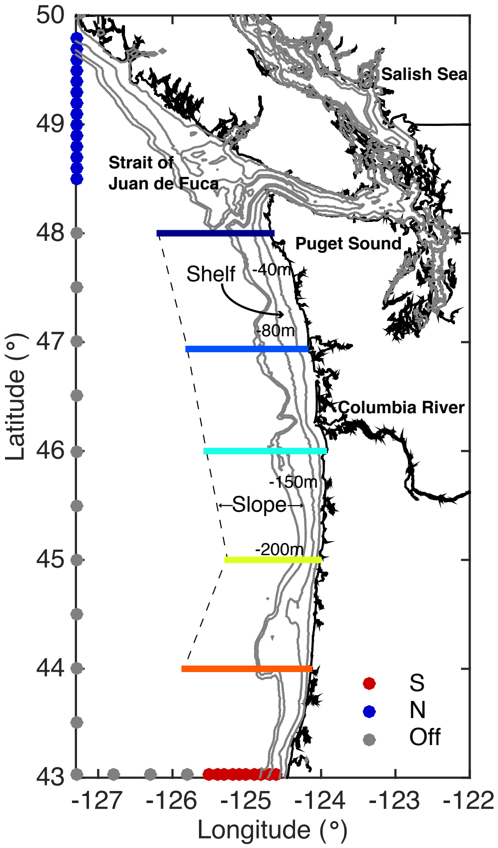

Figure 2.1. Model domain and particle tracking release points. Colored lines indicate latitudes where gridded analysis was conducted. Dots indicate particle release points and are colored by origin, with northern (N) particles in blue, southern (S) particles in red, and offshore (Off) particles in grey. Also plotted in grey are the 40 m, 80 m, 150 m, and 200 m isobaths. The "shelf" (between 40 m and 80 m isobaths) and "slope" (between 150 m isobath and 1° longitude offshore of the 150 m isobath) regions are indicated on the figure, along with geographical regions described in the text.

Giddings et al. (2014) used observational data to validate the physical model on event to seasonal scales. Overall, the model's temperature, salinity, and sea surface elevation had high Willmott Skill Scores ($WS \geq 0.92$; Willmott (1982)), based on comparison with data from 2264 CTD casts in 2005. Comparisons of satellite images with monthly sea-surface temperature model fields showed that spatial patterns associated with coastal upwelling and downwelling are well represented by the model. Additionally, comparison of velocity structure over the shelf between moored sensor data at selected sites and the model showed that coastal-trapped waves, an important feature in this region, are well captured, with the expected event-scale variability associated with coastal-trapped waves evident in along-stream velocity at both the surface (WS = 0.85; correlation coefficient (R) = 0.75) and at 30 m depth (WS = 0.86; R = 0.83). Comparison of density and velocity data from 20 glider cross-sections spanning 2005 – 2007 with model data showed that the location, magnitude, and seasonal variability of the model's CUC was in good qualitative agreement with observations, with the model consistently producing the CUC, with similar magnitude, location, and seasonal development as found in observations. The model's skill decreases beyond the shelf break where it is poorly constrained due to sparse data. Additionally, there is insufficient mixing within the Salish Sea and Strait of Juan de Fuca, likely because the model is unable to resolve their extreme bathymetry, leading to warmer (~2˚C) summer temperatures in the Juan de Fuca eddy and Strait of Juan de Fuca, though this bias is confined to the top ~20 m. Also, there is a deep salinity bias in the model (about 0.2 psu) that is inherited from NCOM boundary conditions (Giddings et al., 2014). More detailed validation, including specific model skill metrics, and further model description can be found in Giddings et al. (2014). The Cascadia model also includes a coupled biogeochemical model (Davis et al., 2014; Siedlecki et al., 2015) that has demonstrated significant skill at predicting nutrients (nitrate concentrations, WS = 0.93) and oxygen (oxygen concentrations, WS (2006) = 0.81, WS (2007) = 0.91) fluctuations on event to seasonal scales—a further indirect validation of the model physics—although the biogeochemical model is not used here because it was run for a more limited range of years.

2.2.2 *Eulerian analysis*

A hindcast of physical parameters, including temperature, salinity, and velocity, spanning 2002 – 2009 was produced using the Cascadia model. Each individual year 2002 – 2009 was run in ROMS initialized from NCOM, and then each year 2003 – 2009 was re-run initialized from the previous year's ROMS run. The year 2002 was thus discarded as spin-up. The hourly output of the Cascadia model was low-pass filtered to daily values (Godin low pass filter; Emery and Thomson (2004)). Depth-longitude slices of salinity (*S*) and potential temperature (θ) were extracted along each latitude from 44˚N to 48˚N for each year spanning 2003 – 2009. A 30-day Hanning filter was then applied to these data, resulting in monthly values, for each of the depth-longitude slices. In this study, we use the monthly values obtained from the 30-day Hanning filter as monthly means. To capture mid-shelf bottom water, the mean was obtained over the bottom 8 *S*-layers of the model domain between the 40 m and 80 m isobaths at each latitude slice. These depth intervals correspond to ~10 m above bottom at the 80 m isobath tapering down to ~5 m above bottom at the 40 m isobath (Figure 2.2a). We will refer to this section of the mid-shelf bottom as the "shelf" for the remainder of this chapter.

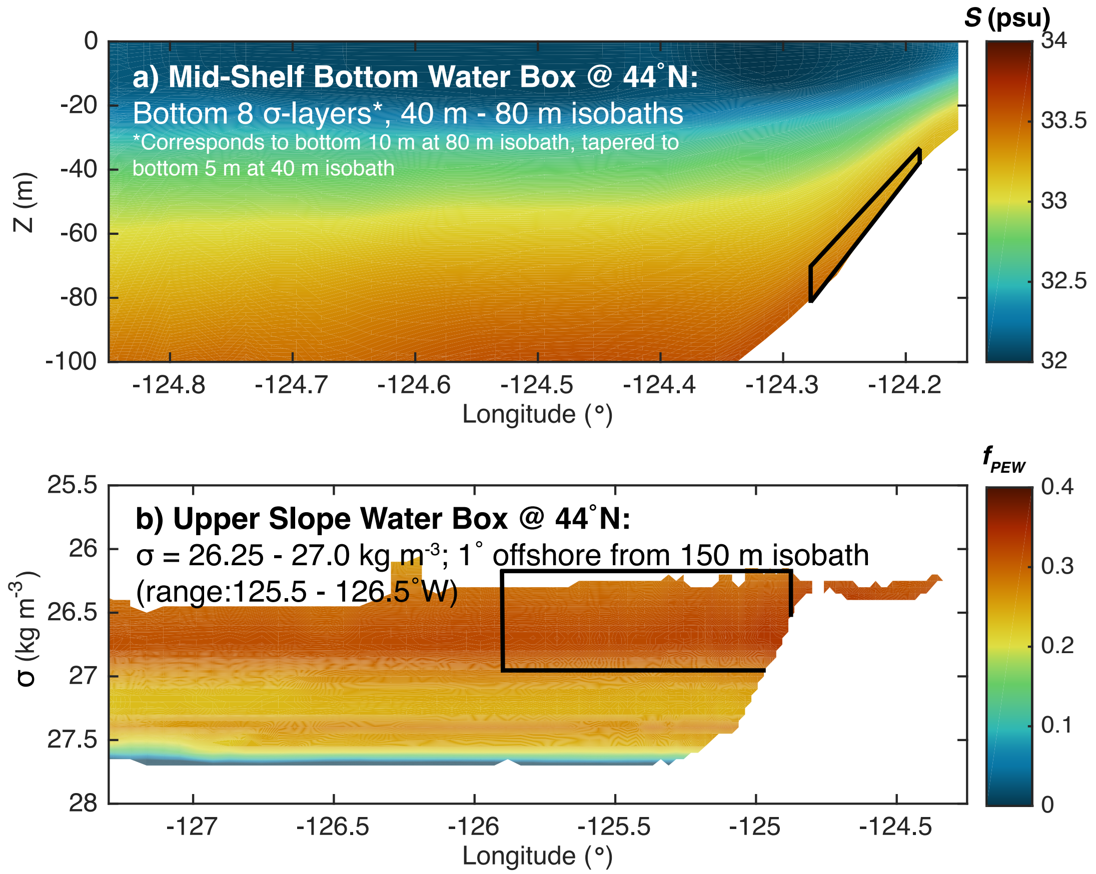

Figure 2.2. Example of (a) mid-shelf bottom water at 44˚N and (b) upper slope water definitions at 44˚N. The mid-shelf bottom water box encompasses the bottom 8 *S*-layers in the model between the 40 m – 80 m isobaths, corresponding to 10 m above the 80 m isobath and 5 m above the 40 m isobath, and this definition is depicted on top of salinity contours (*S*; psu). The upper slope water box is based on density and spans σ_t = 26.25 – 27.0 kg m^{-3}, from the 150 m isobath to 1˚ longitude offshore of the 150 m isobath (varies with latitude, ranging from 125.5˚W to 126.5˚W; ~100 km), and this definition is depicted on top of fraction of Pacific Equatorial Water (f_{PEW}) contours. In this chapter, “shelf” refers to the mid-shelf bottom definition and “slope” refers to the upper slope definition.

To capture CUC water, whose core depth changes both seasonally (Hickey, 1979) and with latitude (Thomson & Krassovski, 2010), model output was interpolated first onto a z-position grid (-3000 m to 0 m, with 10-m intervals) and then onto a σ_t grid (15 kg m^{-3} to 30 kg m^{-3}, with 0.05-kg m^{-3} intervals). Then, an upper slope water box was defined as from the 150 m isobath to 1˚

longitude offshore of the 150 m isobath (western boundary ranging from 125.5°W to 126.5°W, depending on latitude; Figure 2.1), and from $\sigma_t = 26.25$ kg m^{-3} to 27.0 kg m^{-3} (Figure 2.2b). This definition is based on Thomson and Krassovski (2010) (see Figure 2 in Thomson and Krassovski (2010)). We will refer to this section of the upper slope as the "slope" for the remainder of the chapter. As with the shelf water, the mean was taken over this slope water box, yielding time series at each latitude (44°N – 48°N), spanning 2003-2009, of potential temperature (θ), salinity (S), fraction of Pacific Equatorial Water (f_{PEW}), and z-position of the $\sigma_t = 26.5$ kg m^{-3} isopycnal ($z_{26.5}$), representing the depth of the CUC core in the water column. However, if the overall composition of the CUC changes so that its core lies above the $\sigma_t = 26.5$ kg m^{-3} isopycnal, which happened in 2004 (Hickey et al., 2016), then $z_{26.5}$ would not represent the depth of the CUC core. The convention for $z_{26.5}$ is that positive changes in its position indicate a movement upward in the water column. The f_{PEW} in the slope water was calculated by interpolation along isopycnals between the Pacific Equatorial Water (PEW) and Pacific Subarctic Upper Water (PSUW) end-members defined by Thomson and Krassovski (2010). Note that due to modification of water properties by freshwater input, surface heating, and local mixing processes, f_{PEW} on the shelf falls outside the temperature – salinity curves of the PEW and PSUW definition (Thomson & Krassovski, 2010), precluding its use in shelf water analysis. In the analysis below, we thus compare f_{PEW} on the slope with salinity on the shelf (S_{shelf}).

Interannual anomalies were calculated from each of these time series by removing the seasonal cycle (monthly means) of each property on the shelf and slope. Mean seasonal cycles of salinity and temperature on the shelf and slope (Figure 2.3) are consistent with observed seasonal cycles, with cold, salty water present on the shelf (Figure 2.3a, c) during the upwelling season (e.g., Hickey (1989); Hickey et al. (2016); Huyer (1977)), though the shelf water is fresher in the model than in observations (about 0.5 psu) due to the salinity bias inherited from NCOM (Giddings et al., 2014), as well as differences between measurement locations in observations and method of averaging with the model output. There was a smaller seasonal cycle in slope water salinity and temperature, with slightly colder and fresher water during the upwelling season. While the expected trend of warmer and saltier slope water during the upwelling season (due to PEW present over the slope; e.g., Hickey (1979); Pierce et al. (2000); Thomson and Krassovski (2010)) is not evident in the model, this departure is likely due to the method of capturing the CUC by density rather than by depth, resulting in a slope water box with a constant density and seasonal variability in its vertical position. Additionally, compared with the interannual anomalies, the seasonal variation in the model slope water properties is small (Figure 2.3b, d), and whether or not it is removed from the record has a negligible effect on the analysis (change in $R^2 < 0.01$). Moreover, the deep salinity bias due to NCOM in turn biases the calculated f_{PEW} of the slope water by ~0.05. However, because this analysis addresses interannual anomalies rather than mean fields, this bias will not have a significant impact on our results.

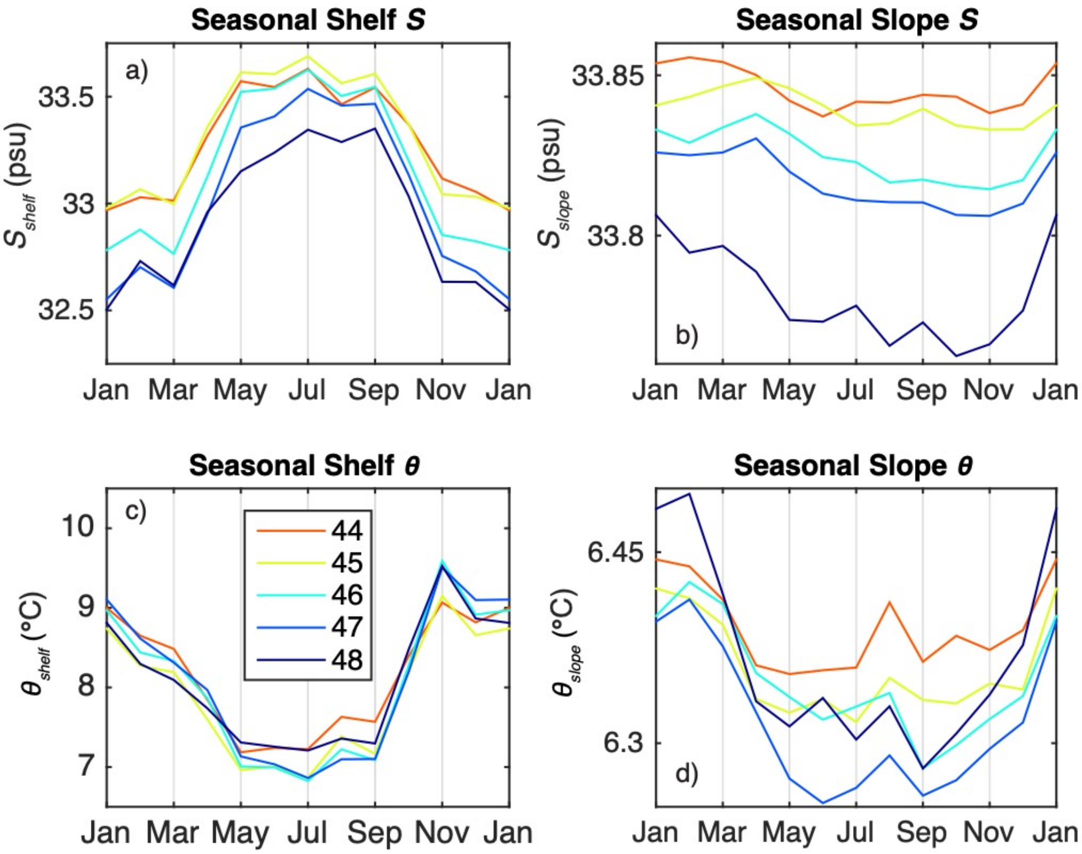

Figure 2.3. Seasonal salinity for the shelf (S_{shelf}; psu; a) and slope (S_{slope}; psu; b), and seasonal temperature for the shelf (θ_{shelf}; ˚C; c) and slope (θ_{slope}; ˚C; d) with color denoting latitude. Note difference in vertical scales for the shelf and slope water properties.

2.2.3 *Wind stress*

Meridional wind stress (τ_y) was used in this analysis to represent the strength of upwelling. Wind stress was derived from MM5/WRF model winds (Mass et al., 2003), which were also used in the atmospheric forcing of the model. The MM5/WRF model winds generally reproduce observed winds well in the study domain, including high correlation with moored sensors (0.66 - 0.93), little bias in wind direction in summer, and good agreement with model and observed wind magnitude in fall (ratio model/observed wind strength = 0.99 ± 0.13; Tinis et al. (2006)). However, the model winds have a 35˚ clockwise bias in wind direction in fall and the magnitude of summer model winds is higher than observed (ratio model/observed wind strength = 1.56 ± 0.65; Tinis et al. (2006)). Local meridional wind stress was calculated from meridional and zonal wind speed at each latitude (44˚N – 48˚N) at 125˚W. Remote wind forcing was represented by meridional wind stress at 40˚N, 125˚W: near the region of maximum forcing of coastal trapped waves (Battisti & Hickey, 1984). Meridional wind stress was calculated from 3-hourly meridional and zonal wind speeds, and the resulting stresses were averaged to daily values. Then the same 30-day Hanning filter used with Cascadia model output was applied to the wind stress data to derive monthly values. As above, the mean seasonal cycle was removed from the time series to obtain interannual anomalies.

2.2.4 *Lagrangian analysis*

Within the Cascadia model run, 3 million particles were released at 38 points along the model boundaries (see Figure 2.1) at every tenth of the full water column depth, once daily from January 2002 to November 2008. For the purpose of this study, we only used particles that were released in the top 600 m of the water column. To avoid double counting, particles that exited the domain within the first three days of their release were excluded, as well as particles that were released when flow at the model boundary was outward. After application of these criteria, about 203,500 particles remained for use in this analysis, an average of 70 particles per day. Each particle's position in latitude, longitude, and depth was tracked each day until it moved outside the model boundaries or was "beached" on land, defined as being close enough to land that a bilinear interpolation of the ROMS land mask (1 for ocean, 0 for land) at its location was less than 0.5

(Banas et al., 2015). Based on these criteria, average particle lifetime was 61 ± 78 days. Vertical motion includes a random-displacement scheme for vertical diffusion (Banas, McDonald, et al., 2009; Visser, 1997).

Analysis included particles that were found on the shelf or over the slope at any time during the 2003 – 2008 record. In this context, the shelf was defined as the bottom half of the water column over the region between the 40 m and 80 m isobaths. We included the bottom half of the column, rather than just the bottom 1/8 of the water column as was used in the Eulerian analysis, to ensure that there would be enough particles to produce statistically significant results. The slope was defined as the water column between 150 m and 500 m over the region between the 150 m isobath and 1˚ longitude from the 150 m isobath (ranging from 125.5˚W to 126.5˚W, depending on latitude; Figure 2.1). The shelf and slope were divided into 1° latitude bands for analysis centered on the sections in the previous analysis, e.g., with 44˚N represented by the region between 43.5˚N and 44.5˚N. On average, there were 42 ± 19 particles in each 1° shelf band and 1783 ± 550 particles in each 1˚ slope band at each time step. Once any particle moved into the Salish Sea (eastward of 124˚W in the Strait of Juan de Fuca; see Figure 2.1), it was eliminated from analysis. Analysis of these "Salish Sea" particles showed that inclusion of outflow from the Salish Sea results in more particles of deep origin (~ 14% more) on the shelf near the Strait of Juan de Fuca (48˚N); however, they have very little (< 1%) influence on water origin in the rest of the domain. All particles were then divided into categories based on where they entered the model domain. These categories are "Southern" (at 43˚N, between the coast and 125.5˚W: Figure 2.1), "Northern" (at 127˚W, between 48.5˚N and 50˚N: Figure 2.1), and "Offshore" (everywhere else on the model boundary: Figure 2.1). The Northern and Southern particles were also divided into "shallow" particles (entering above 150 m depth) and "deep" particles (entering below 150 m depth). Figure

2.4 depicts an example of deep particle tracks colored by water origin for particles that end up within the slope box at 47˚N for September 12-18, 2004 and 2007.

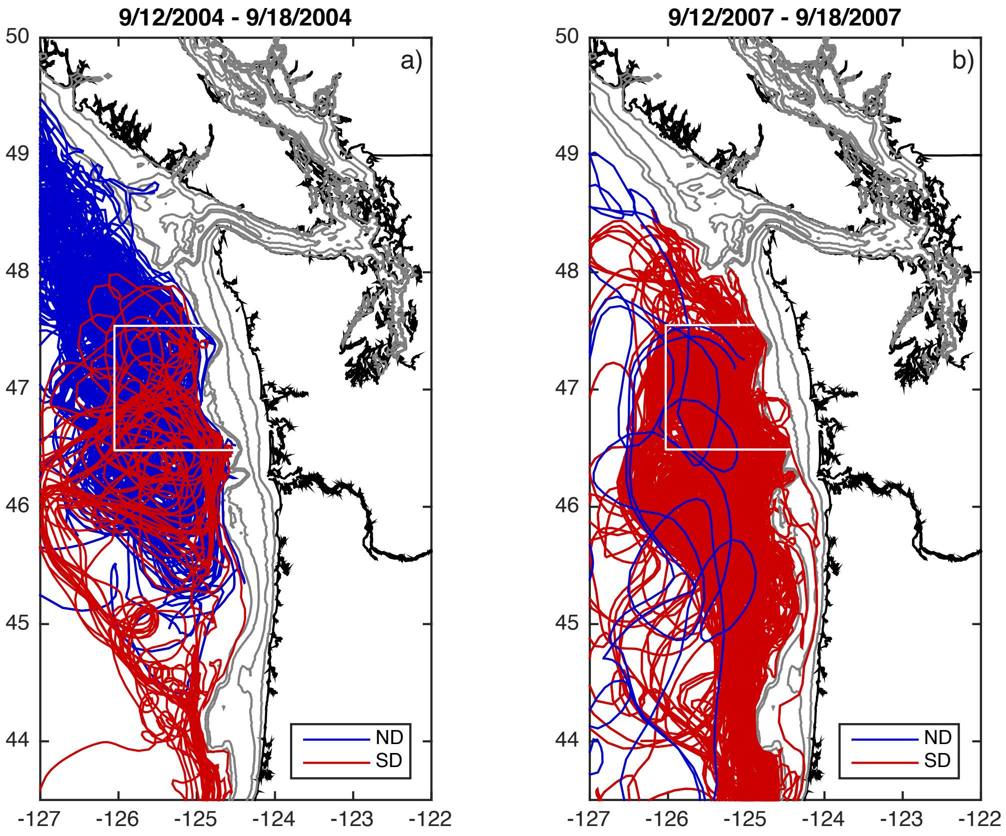

Figure 2.4. Tracks of deep particles (released below 150 m depth) that were found on the slope at 47.5˚N (between 46.5˚N and 47˚N; 126˚W to the 150 m depth; white box) during one week in mid-September 2004 (a) and in mid-September 2007 (b). Particle tracks are colored by source: ND = Northern deep water (blue); SD = Southern deep water (red). Release locations of particles are indicated in Figure 2.1.

From here, the fraction of particles (*f*) from each origin in each region was calculated at every time step (daily). These daily values were integrated over 30-day periods. The seasonal cycle and interannual anomalies for the particle origin fractions in each region were calculated as described above in the Eulerian analysis. Note that the particle release, originally performed for a different application, does not include 2009 and therefore comparisons between the gridded and Lagrangian analyses only span 2003 – 2008.

As mentioned previously, the entire bottom half of the water column rather than the bottom 1/8 of the water column was included over the shelf to ensure that there were enough particles at each time step to generate statistically significant results. However, due to the dynamics of flow over the shelf, the bottom half of the water column includes both the bottom boundary layer (offshore flow developing later in the upwelling season) and a portion of the interior flow (onshore flow developing over the upwelling season), rather than only the bottom boundary layer as in the Eulerian analysis of shelf water. While the alongshelf flow dominates the cross-shelf flow, this definition leads to a bias in the fraction of "Southern" particles (f_s) of about 20% in the bottom half compared to the bottom 1/8 of the water column. Over the entire record, on average, the f_s of the bottom half of the water column was 0.43 while the f_s of the bottom 1/8 of the water column was 0.52. The effect of this bias on our results is reduced by removal of the mean seasonal cycle when calculating interannual anomalies, and its effect on the R^2 of correlations found in this study is < 0.05 in all cases.

2.3 RESULTS

2.3.1 *Eulerian analysis: shelf water*

As expected for any Eastern Boundary Current System, the shelf (bottom 1/8 of the water column between the 40 m and 80 m isobaths) water experienced a seasonal cycle in its water properties. During the upwelling season, salinity (S_{shelf}) was at its highest, with a mean seasonal high of 33.57 psu (Figure 2.3a), and temperature (θ_{shelf}) was at its lowest, with a mean seasonal low of 6.99˚C

(Figure 2.3c). The standard deviation of the seasonal variation for S_{shelf} was 0.32 psu and 0.83˚C for θ_{shelf}. The interannual anomalies in salinity (S'_{shelf}) and temperature (θ'_{shelf}) in shelf water had standard deviations ~0.8 of their seasonal variation (Figure 2.5). Additionally, there was little difference across latitudes in either salinity or temperature anomalies. Hickey et al. (2016) also found similar anomalies in near-bottom shelf water both seasonally and interannually across a similar latitudinal range using observational data. However, the interannual anomalies observed by Hickey et al. (2016) differed significantly between the summer and winter over their observed time period, with very little variability among summer months and high variability in winter months. This pattern was also evident in the model (Figure 2.5), with standard deviations during winter months nearly twice those during summer months. All variable symbols and their definitions are outlined in Table 2.1.

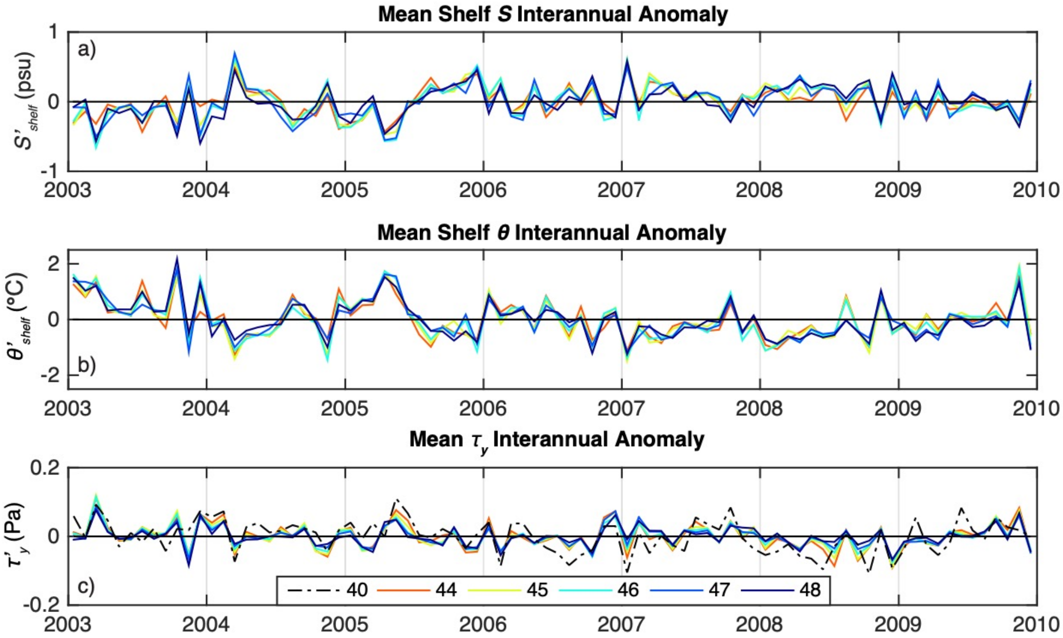

Figure 2.5. Time series of interannual anomalies in modeled shelf water properties: (a) salinity (S'_{shelf}; psu) and (b) potential temperature (θ'_{shelf}; ˚C), and (c) meridional wind stress (τ'_y; Pa). Color denotes latitude, with remote wind stress at 40˚N plotted in dashed black in (c). Ticks mark the beginning of each year.

Table 2.1. Definitions of all analyzed Eulerian and Lagrangian variables[1].

Variable Symbol	**Description**
Eulerian	
τ_y^{local}	Meridional local wind stress: measured at each latitude (44˚N-48˚N), 125˚W (Pa)
τ_y^{remote}	Meridional remote wind stress: measured at 40˚N, 125˚W (Pa)
$z_{26.5}$	Depth of the $\sigma_t = 26.5$ kg m^{-3} isopycnal (m)
f_{PEW}	Fraction of Pacific Equatorial Water (PEW)
S_{shelf}	Salinity (psu) on the shelf (bottom 1/8 of the water column between 40 m – 80 m isobaths)
θ_{shelf}	Potential temperature (˚C) on the shelf (bottom 1/8 of the water column between 40 m – 80 m isobaths)
S_{slope}	Salinity (psu) on the slope ($\sigma_t = 26.25 – 27.0$ kg m^{-3} isopycnals, between 150 m isobath and 1˚ longitude offshore of the 150 m isobath)
θ_{slope}	Potential temperature (˚C) on the slope ($\sigma_t = 26.25 – 27.0$ kg m^{-3} isopycnals, between 150 m isobath and 1˚ longitude offshore of the 150 m isobath)
Lagrangian	
f_S^{shelf}	Fraction of southern water (released at 43˚N, between coast and 125.5˚W) on the shelf (bottom half of the water column between 40 m – 80 m isobaths)
f_{Sh}^{shelf}	Fraction of shallow water (released above 150 m depth) on the shelf (bottom half of the water column between 40 m – 80 m isobaths)
f_S^{slope}	Fraction of southern water (released at 43˚N, between coast and 125.5˚W) on the slope (150-500 m depth, between 150 m isobath and 1˚ longitude offshore of the 150 m isobath)
f_{Sh}^{slope}	Fraction of shallow water (released above 150 m depth) on the slope (150-500 m depth, between 150 m isobath and 1˚ longitude offshore of the 150 m isobath)

In general, the anomalies in shelf salinity and temperature were inversely correlated ($R^2 = 0.72 \pm 0.05$), i.e., with cold and salty conditions coinciding (Figure 2.6a). (All correlations mentioned in this paper are significant at the 95% confidence level, with the degrees of freedom (df) calculated using the autocorrelation method, and all significant cross-correlations among variables are outlined in Table 2.2.) The delayed upwelling in 2005, described by Hickey et al. (2006) and Pierce et al. (2006), is apparent in the transition from negative to positive salinity anomalies and from positive to negative temperature anomalies in late May 2005 (Figure 2.5). In addition, the unusually warmer and fresher water found on the NCCS shelf in July through October 2004 (Figure 2.5) was also observed in moored array data at several sites by Hickey et al. (2016).

---

[1] In text, anomalies are indicated by ‘.

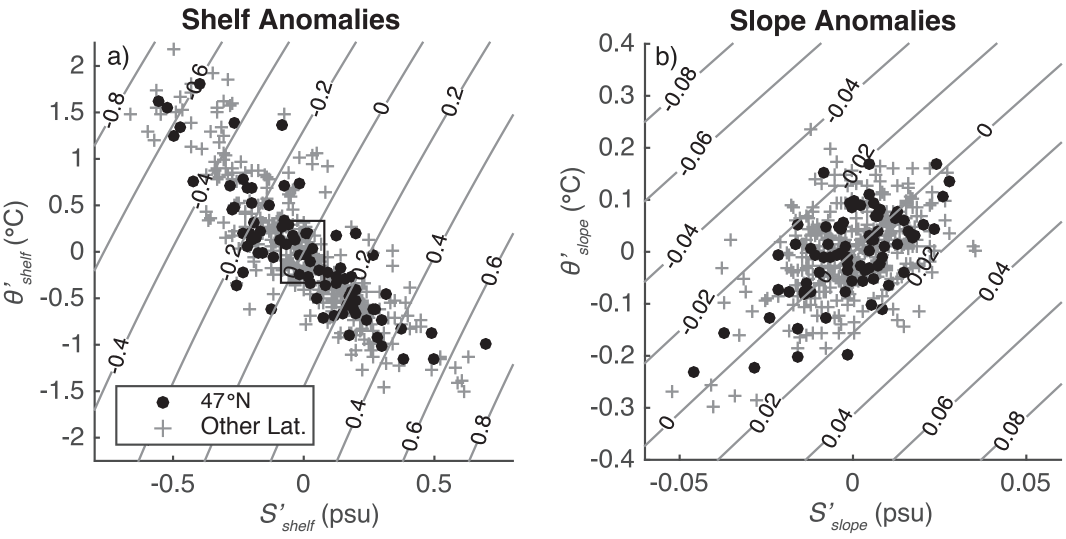

Figure 2.6. (a) Interannual anomalies in shelf salinity (S'_{shelf}; psu) plotted against interannual anomalies in shelf temperature (θ'_{shelf}; ˚C; $R^2 = 0.72 \pm 0.05$, degrees of freedom (df) = 66.8), and (b) interannual anomalies in slope salinity (S'_{slope}; psu) plotted against interannual anomalies in slope temperature (θ'_{slope}; ˚C; $R^2 = 0.30 \pm 0.07$, df = 23.2; not significant at 45˚N or 48˚N). Circles denote values at 47˚N, + denote all other latitudes, and the isopycnals (anomalies from the record mean shelf and slope density) are plotted in grey. R^2 and df are the mean for all data at 95% confidence. The box on the shelf anomalies plot depicts the range of the slope anomalies within the range of the shelf anomalies.

Table 2.2. Significant cross-correlations of interannual anomalies in all analyzed variables. Local wind stress (τ'^{local}_{y}), remote wind stress (τ'^{remote}_{y}), depth of the 26.5 kg m^{-3} isopycnal ($z'_{26.5}$), fraction of PEW (f'_{PEW}), shelf salinity (S'_{shelf}), shelf temperature (θ'_{shelf}), slope salinity (S'_{slope}), slope temperature (θ'_{slope}), fraction of southern source water on the shelf (f'^{shelf}_{S}), fraction of shallow source water on the shelf (f'^{shelf}_{Sh}), fraction of southern water on the slope (f'^{slope}_{S}), and fraction of shallow water on the slope (f'^{slope}_{Sh}). Correlations are significant at the 95% confidence interval and apply to all latitudes unless otherwise indicated.

	τ'^{local}_{y}	τ'^{remote}_{y}	$z'_{26.5}$	f'_{PEW}	S'_{shelf}	θ'_{shelf}	S'_{slope}	θ'_{slope}	f'^{shelf}_{S}	f'^{shelf}_{Sh}	f'^{slope}_{S}	f'^{slope}_{Sh}
τ'^{local}_{y}	--											
τ'^{remote}_{y}	0.37	--										
$z'_{26.5}$	—	—	--									
f'_{PEW}	—	—	*0.21*[2]	--								
S'_{shelf}	0.44	0.34	*0.18*[3]	—	--							
θ'_{shelf}	0.35	0.25	*0.22*[4]	*0.11*[d]	0.72	--						
S'_{slope}	—	—	—	0.59	—	—	--					
θ'_{slope}	—	—	*0.36*[5]	0.83	—	0.16	*0.30*[6]	--				
f'^{shelf}_{S}	—	—	—	—	—	—	—	—	--			
f'^{shelf}_{Sh}	—	—	—	—	—	—	—	—	*0.19*[7]	--		
f'^{slope}_{S}	—	—	—	—	—	—	—	—	*0.43*[e]	—	--	
f'^{slope}_{Sh}	—	—	—	—	—	—	—	—	*0.21*[8]	*0.10*[9]	*0.36*[h]	--

2.3.2 *Eulerian analysis: slope water*

As expected, the slope (σ_t = 26.25 – 27.0 kg m^{-3} isopycnals, between 150 m isobath and 1° longitude offshore of the 150 m isobath) water properties did not show as pronounced a seasonal cycle as did the water on the shelf (Figure 2.3b, d). The standard deviation of interannual anomalies in slope salinity (S'_{slope}), temperature (θ'_{slope}), and fraction of PEW (f'_{PEW}) were about 1.6 times as

---

[2] Significant at 95% confidence interval for 45°N, 46°N, and 48°N.

[3] Significant at 95% confidence interval for 44°N, 45°N, and 48°N.

[4] Significant at 95% confidence interval for 44°N – 46°N, and 48°N.

[5] Significant at 95% confidence interval for 45°N – 48°N.

[6] Significant at 95% confidence interval for 44°N, 46°N, and 47°N.

[7] Significant at 95% confidence interval for 44°N and 45°N.

[8] Significant at 95% confidence interval for 46°N – 48°N.

[9] Significant at 95% confidence interval for 45°N, 46°N, and 48°N.

large as the standard deviation in their seasonal variation (Figure 2.7). Over the record, the mean f'_{PEW} over all latitudes is about 0.31, which is about 0.05 less than observations by Thomson and Krassovski (2010). This difference can be attributed to the salinity bias in the model, as described in Sec 2.2 above. Both slope salinity (S_{slope}) and temperature (θ_{slope}) decreased in the summer, as well as with latitude, with a greater seasonal decrease in temperature (Figure 2.3b, d), and S'_{slope} and θ'_{slope} are significantly correlated ($R^2 = 0.30 \pm 0.07$; not significant at 45°N or 48°N; Figure 2.6b). Thus, cold and fresh conditions generally coincide on the slope, indicative of advection or change along isopycnals, in contrast to the shelf where cold and salty conditions coincide, indicative of advection or change across isopycnals, as mentioned above (Figure 2.6). Note that the scale of these anomalies on the shelf is an order of magnitude larger than on the slope, and the anomalies in slope water properties are contained within the scatter in anomalies of shelf water (small box embedded in Figure 2.6a).

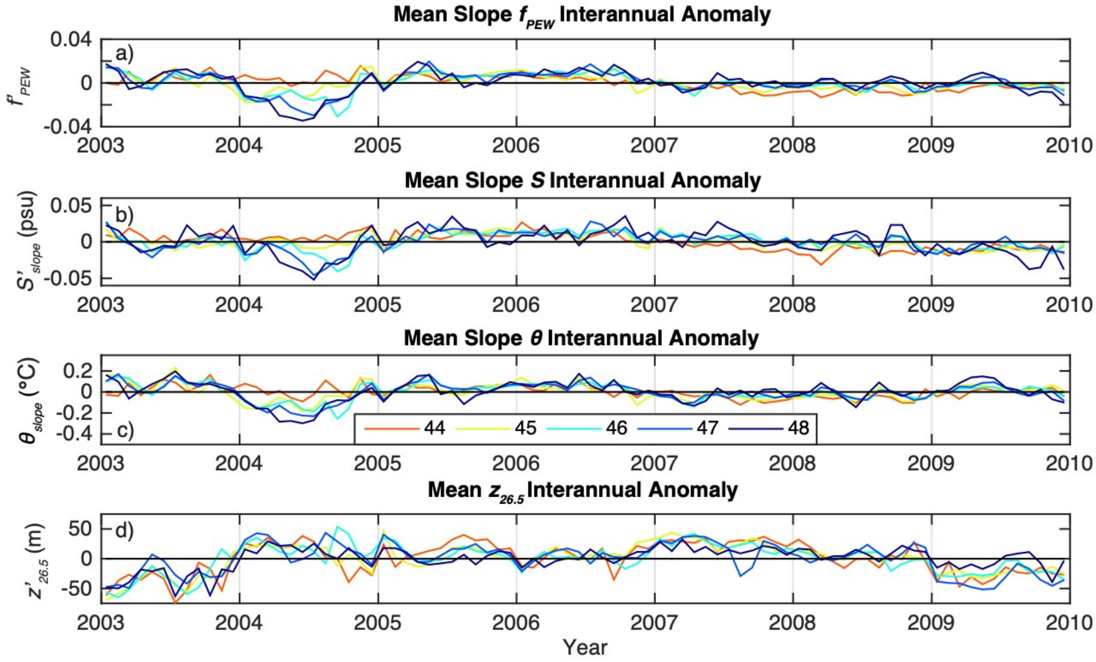

Figure 2.7. Time series of interannual anomalies in modeled slope water properties: (a) Pacific Equatorial Water (PEW) fraction (f'_{PEW}), (b) salinity (S'_{slope}; psu), (c) potential temperature (θ'_{slope}; ˚C), and (d) z-position of $\sigma_t = 26.5$ kg m^{-3} isopycnal ($z'_{26.5}$; m), representative of CUC core depth. Color denotes latitude. Ticks mark the beginning of each year.

Throughout most of the time series, S'_{slope}, θ'_{slope}, and f'_{PEW} vary similarly at all latitudes. However, in 2004 there is an unusual poleward gradient in water properties over the slope, with anomalously cold, fresh, and low f_{PEW} in the north (Figure 2.7). This cold, fresh, low f_{PEW} water could be indicative of an intrusion of subarctic water from the north (e.g., Kosro (2003)) and could explain the poleward gradient in water properties over the slope. Lagrangian analysis corroborates this interpretation, indicating an anomalously high fraction of water from the north over the slope during the late upwelling season in 2004 (Figure 2.4; Section 2.3.5below).

The 26.5 kg m^{-3} isopycnal represents the core of the CUC (Thomson & Krassovski, 2010); thus $z_{26.5}$ represents the z-position of the CUC and suggests the vertical movement of the CUC in the water column. Seasonally, $z_{26.5}$ varied by about 26 m, with a shoaling of $z_{26.5}$ during the upwelling season (not shown). The mean $z_{26.5}$ over all latitudes ranged from -210 m to -184 m over the seasonal cycle. However, the standard deviation in interannual anomalies in the depth of the 26.5 kg m^{-3} isopycnal ($z'_{26.5}$) was about three times as large as the standard deviation of its seasonal variation.

2.3.3 *Eulerian analysis: relationships between water properties and wind stress*

Interannual anomalies in shelf salinity (S'_{shelf}) were significantly correlated with interannual anomalies in local wind stress ($\tau'_y{}^{local}$; Figure 2.8a; Table 2.2) and remote (40˚N) wind stress ($\tau'_y{}^{remote}$; Figure 2.8b; Table 2.2). The correlations suggest that, over all latitudes, on average, local wind variability accounted for about 44% ± 10% of shelf salinity variability, while remote wind variability accounted for about 34% ± 9% of shelf salinity variability (Table 2.2). August values are displayed in these figures to highlight the upwelling season, although the local and remote wind stress correlations include the entire year.

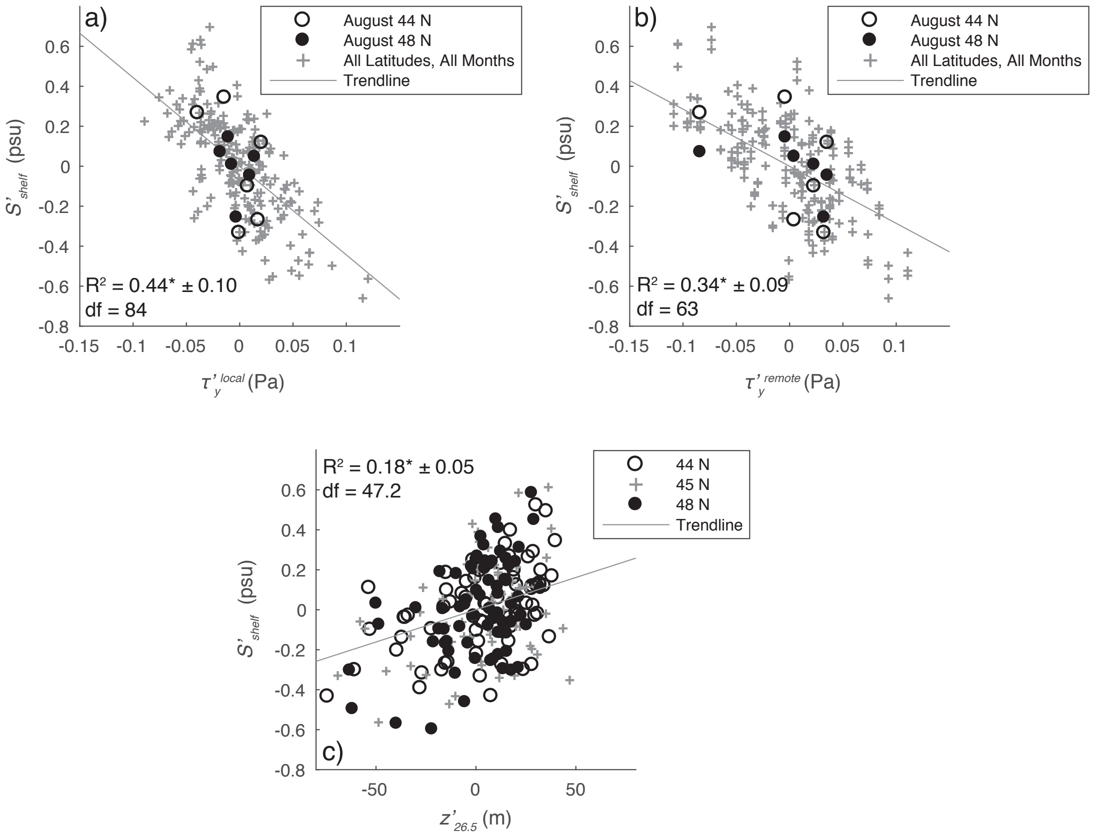

Figure 2.8. Interannual anomalies in shelf salinity (S'_{shelf}; psu) plotted against (a) interannual anomalies in local wind stress ($\tau'_y{}^{local}$; Pa), (b) interannual anomalies in remote wind stress ($\tau'_y{}^{remote}$; Pa), and (c) interannual anomalies in CUC core depth ($z'_{26.5}$; m). For a) and b), open circles denote August values at 44˚N, filled circles denotes August values at 48˚N, + denote all latitudes during all months of the year, and the trend line is plotted in grey. R^2 and df are the mean for all data at 95% confidence. For c), open circles denote values at 44˚N, + denote values at 45˚N, filled circles denote values 48˚N, and the trend line is plotted in grey. R^2 and df are the mean for 44˚N, 45˚N, and 48˚N at 95% confidence.

Likewise, interannual anomalies in shelf salinity (S'_{shelf}) were significantly correlated with interannual anomalies in CUC z-position ($z'_{26.5}$; Figure 2.8c; Table 2.2). For 44˚N, 45˚N, and 48˚N, variability in $z'_{26.5}$ accounted for 18% ± 5% of S'_{shelf} variability, such that when the CUC is shallower, the shelf water is saltier. Correlations of S'_{shelf} and $z'_{26.5}$ at 46˚N and 47˚N were not significant (Table 2.2).

Similar to shelf salinity anomalies, temperature anomalies (θ'_{shelf}) were significantly correlated with $\tau'_y{}^{local}$ ($R^2 = 0.35 \pm 0.07$; Table 2.2) and $\tau'_y{}^{remote}$ ($R^2 = 0.25 \pm 0.04$; Table 2.2) and with anomalies in $z'_{26.5}$ ($R^2 = 0.22 \pm 0.09$, excluding 47°N; Table 2.2). Additionally, θ'_{shelf} was weakly, but significantly, correlated with fraction of PEW (f'_{PEW}, $R^2 = 0.11 \pm 0.01$, excluding 47°N; Table 2.2). As expected, $\tau'_y{}^{local}$ and $\tau'_y{}^{remote}$ were significantly correlated, with an average $R^2 = 0.37 \pm 0.11$ (Table 2.2).

Slope temperature anomalies (θ'_{slope}) were also significantly correlated with $z'_{26.5}$ ($R^2 = 0.36 \pm 0.09$, excluding 44°N; Table 2.2) and f'_{PEW} ($R^2 = 0.83 \pm 0.07$; Table 2.2). Similarly, slope salinity anomalies (S'_{slope}) were correlated with f'_{PEW} ($R^2 = 0.59 \pm 0.11$; Table 2.2). Also, interannual anomalies in $z'_{26.5}$ and f'_{PEW} were correlated at 45°N, 46°N, and 48°N, with an average $R^2 = 0.21 \pm 0.01$ with a deeper undercurrent carrying a greater PEW fraction (Table 2.2). No other significant correlations were found among shelf water properties, slope water properties, or wind stress.

To better account for cross-correlation among the three forcing variables discussed above (local wind stress ($\tau'_y{}^{local}$) remote wind stress ($\tau'_y{}^{remote}$) and CUC core depth ($z'_{26.5}$)), a Generalized Linear Model (GLM; Nelder and Wedderburn (1972)) was constructed for the interannual shelf salinity anomalies (S'_{shelf}) record at each latitude, based on anomalies in the three forcing variables. The interannual variability in shelf salinity was reasonably well reconstructed by the GLM, with an average $R^2 = 0.58 \pm 0.08$ for all latitudes. The best fit was at 48°N with $R^2 = 0.69$ (Figure 2.9).

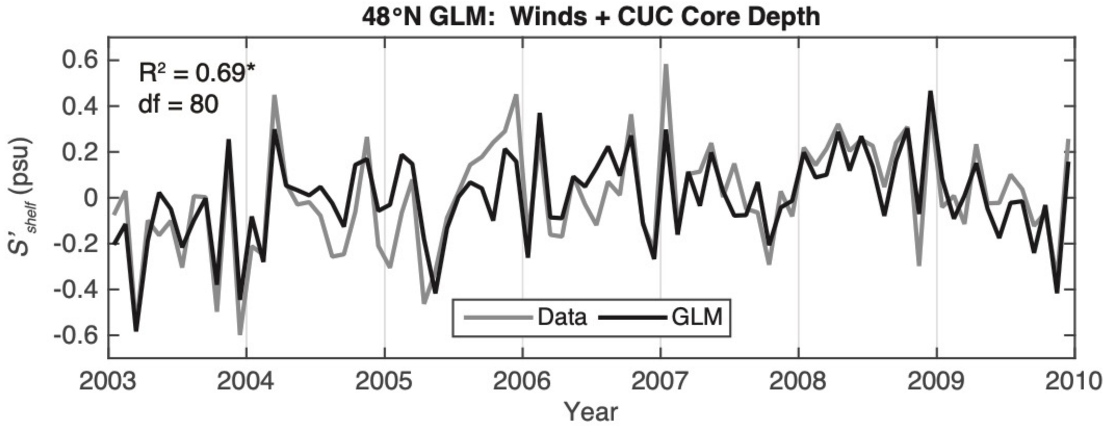

Figure 2.9. Time series of interannual anomalies in shelf salinity (*S'*$_{shelf}$; psu) at 48˚N (grey) plotted with time series of GLM of interannual anomalies in shelf salinity (*S'*$_{shelf}$; psu) at 48˚N (black), recreated using interannual anomalies in local wind stress ($\tau'_y{}^{local}$; Pa), remote wind stress ($\tau'_y{}^{remote}$; Pa), and CUC core depth ($z'_{26.5}$; m). R^2 =0.69 (significant at 95% confidence), degrees of freedom = 80.

2.3.4 *Lagrangian analysis: shelf*

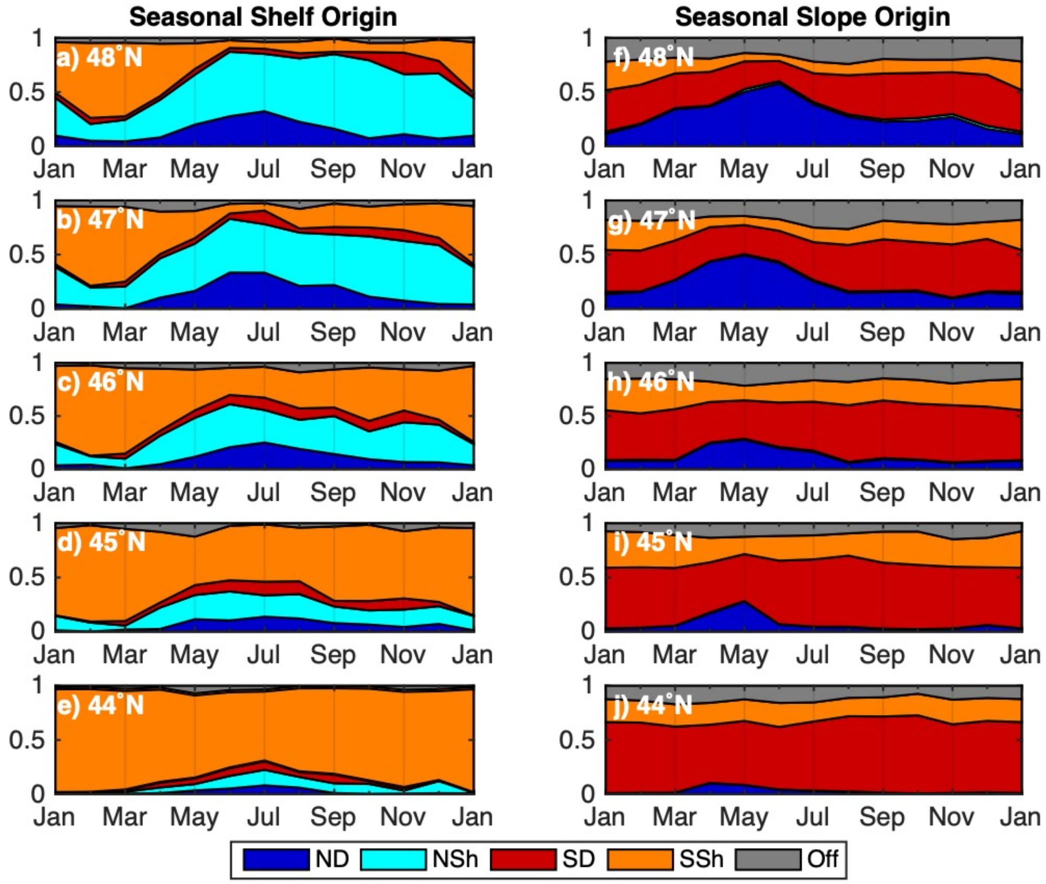

Figure 2.10. Seasonal fraction of shelf water (a-e) and of slope water (f-j) for each latitude (44˚N – 48˚N) colored by origin. ND = Northern Deep water (blue); NSh = Northern Shallow water (cyan); SD = Southern Deep water (red); SSh = Southern Shallow water (orange); Off = Offshore water (grey). Deep and shallow releases were divided by the 150 m depth contour. Release locations of particles are indicated in Figure 2.1. Ticks mark the beginning of each month.

The shelf (bottom half of the water column between 40 m and 80 m isobaths) experienced high variability in water origin both seasonally (Figure 2.10a-e) and interannually (Figure 2.11a-e). The standard deviations in interannual anomalies in water origin were about 1.4 times the standard deviations in the seasonal variation. Throughout the entire record, shelf water was mostly composed of shallow water (NSh and SSh, Figure 2.11a-e), although there were occasional intrusions of northern deep water (ND, Figure 2.11a-e) that are consistent with the timing of deep northern water intrusions on the slope (ND, Figure 2.11f-j). At northern latitudes, northern water (ND and NSh, Figure 2.10a-e) dominated the water on the shelf during the upwelling season, consistent with the equatorward coastal jet associated with upwelling. At southern latitudes, southern water (SD and SSh, Figure 2.10a-e) dominated the water on the shelf, with a small increase in northern water during the upwelling season. There are also small amounts of southern deep water present on the shelf during the late summer into fall (SD, Figure 2.10a-e), and this pattern is more evident in some years, like 2005, than in others, like 2004 (SD, Figure 2.11a-e). During the winter shelf water transitioned to mostly southern water (SD and SSh, Figure 2.10a-e), consistent with the poleward flow associated with downwelling, as well as the larger-scale Davidson Current.

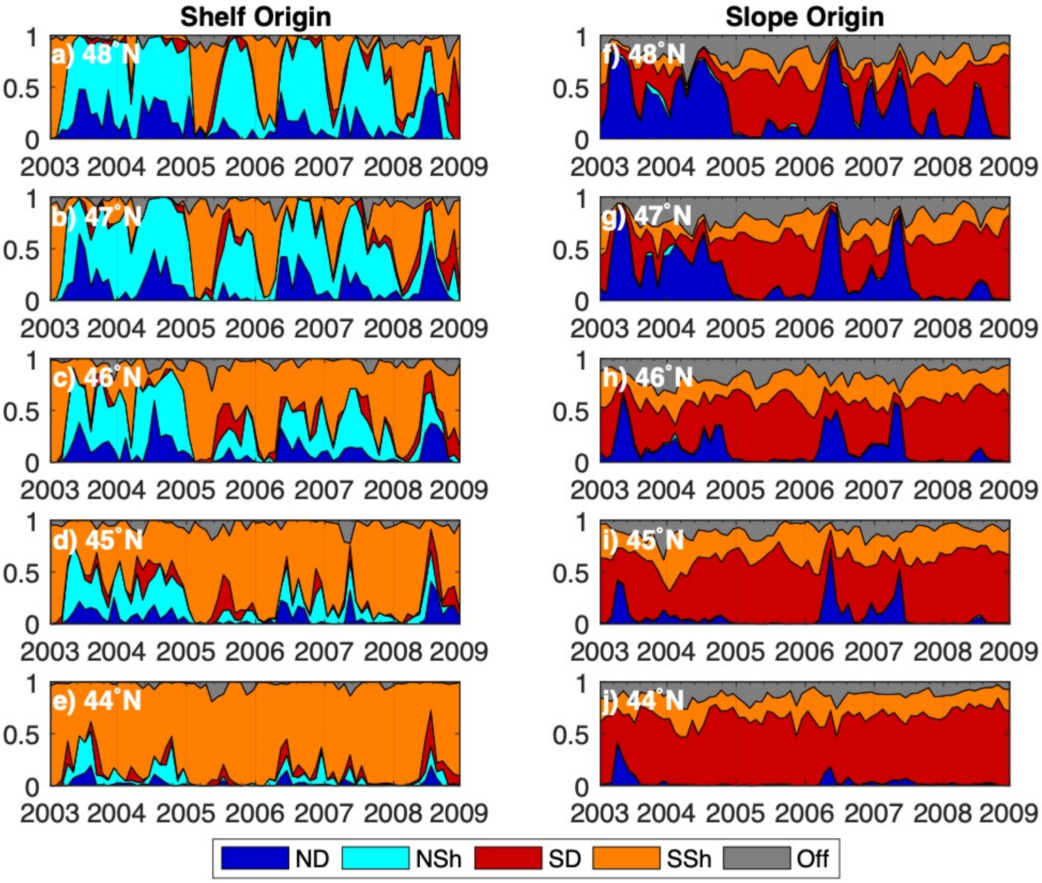

Figure 2.11. Full monthly-averaged time series of fraction of shelf water (a-e) and of slope water (f-j) for each latitude (a-e; 44˚N – 48˚N) colored by origin, colors as in Figure 2.10. The seasonal cycle was not removed. Deep and shallow releases were divided by the 150 m depth contour. Release locations of particles are indicated in Figure 2.1. Ticks mark the beginning of each year.

2.3.5 *Lagrangian analysis: slope*

On the slope (150 m to 500 m depth; between 150 m isobath and 1˚ longitude offshore of 150 m isobath), water origin varied more interannually (Figure 2.11f-j) than it did seasonally (Figure 2.10f-j). The standard deviations in interannual anomalies in slope water origin were about 1.8 as large as the standard deviations in their seasonal variation. Throughout the entire record, the slope was mostly composed of deep water (ND and SD) as compared to shallow water (NSh and SSh,

Figure 2.11f-j). Southern deep water (SD, Figure 2.10f-j) increased over the upwelling season, ultimately dominating the water on the slope, while northern deep water increased during the winter into the spring when the CUC is absent (ND, Figure 2.10f-j). This seasonal pattern is expected, and suggests the CUC gradually flushing out northern water over the upwelling season as it develops each year. The increase in northern deep water on the slope during winter into spring (ND, Figure 2.10f-j) could be indicative of the Washington Undercurrent, a deep equatorward current that sometimes flows over the Washington slope during winter months (Hickey, 1989). The increase in northern water present on the slope with latitude is consistent with hydrographic results from Thomson and Krassovski (2010).

2.3.6 *Lagrangian analysis: relationships between water sources*

Interannual anomalies in the fraction of southern water (shallow (SSh) and deep (SD) combined) in the slope water (f'^{slope}_{S}) and over the shelf (f'^{shelf}_{S}) were significantly correlated over most of the model domain (45˚N – 48˚N), with average $R^2 = 0.43 \pm 0.10$, although the correlation at 44°N was not significant (Figure 2.12; Table 2.2). The intrusions of northern water on the slope (Figure 2.11f-j) coincided with intrusions of northern water on the shelf (Figure 2.11a-e). The strong intrusion of northern deep water of 2004 (ND, Figure 2.4, Figure 2.11f-j) may have been responsible for the unusual poleward gradient in water properties, with colder, fresher water to the north, over the slope in 2004 (Figure 2.7). The difference in water origin on the slope in the anomalous 2004 year as compared to a typical year like 2007 is especially apparent in the tracks of particles colored by water origin in Figure 2.4.

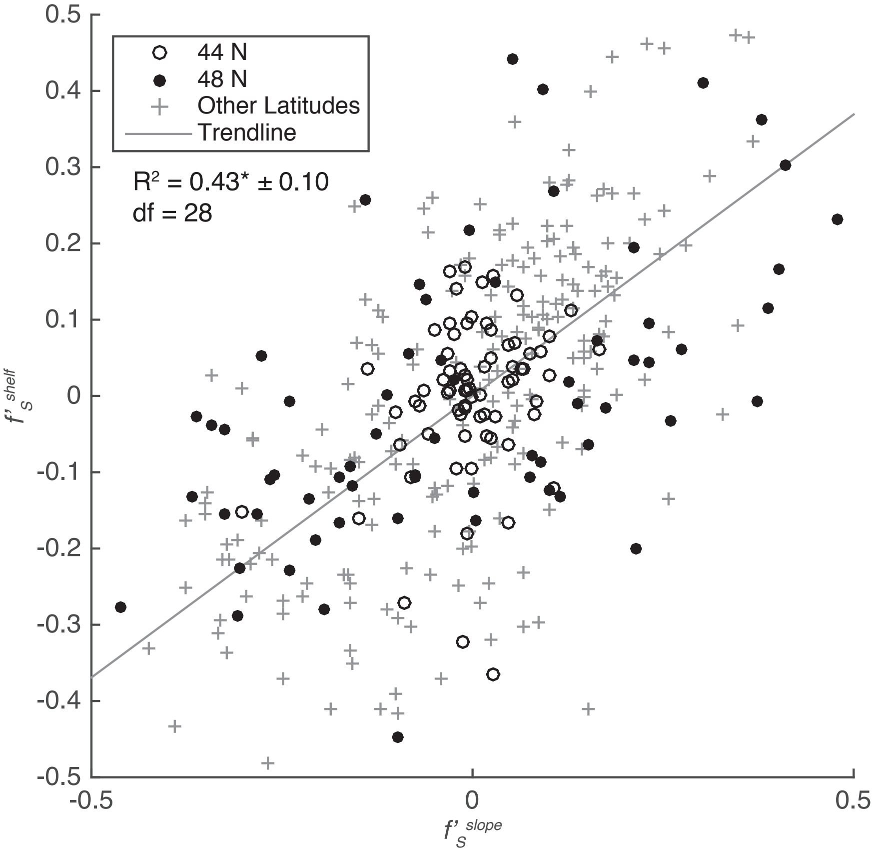

Figure 2.12. Interannual anomalies in fraction of southern water on the shelf ($f'_S{}^{shelf}$) plotted against interannual anomalies in fraction of southern water on the slope ($f'_S{}^{slope}$). Open circles denote values at 44˚N, filled circles denote values at 48˚N, + denote other latitudes, and the trend line is plotted in grey. R^2 and df are for all data excluding 44°N at 95% confidence.

The anomalies in the fraction of southern water (f'_S) represents north and south water masses since the offshore fraction (f'_{Off}) has a smaller interannual variation on both the shelf and slope (standard deviation = 0.05, 0.07, respectively) as compared to the southern fraction (f'_S; standard deviation = 0.20, 0.17, respectively) and northern fraction (f'_N; standard deviation = 0.21, 0.15, respectively) on the shelf and slope. So, any loss in southern water is largely replaced by northern water, as expected. Weaker correlations that were significant within some, but not all, of the model domain between f'_S and anomalies in fraction of shallow water (f'_{Sh}) are outlined in Table 2.2. The Lagrangian metrics f'_S and f'_{Sh} were not significantly correlated with any variable from the Eulerian analysis discussed previously, for either the slope or the shelf, for a combination of numerical and dynamical reasons, as discussed below.

2.4 DISCUSSION

2.4.1 *Upwelling system dynamics*

Interannual anomalies in shelf (bottom 1/8 of the water column between the 40 m and 80 m isobaths) salinity (S'_{shelf}) and temperature (θ'_{shelf}) were significantly correlated with each other ($R^2 = 0.72 \pm 0.05$), with an inverse relationship, aligned approximately orthogonal to isopycnals (Figure 2.6a). This relationship suggests that variation in the strength, vertical structure, and apparent source depth of upwelling largely drives the relationship between salinity and temperature on the shelf. Slope ($\sigma_t = 26.25 - 27.0$ kg m^{-3} isopycnals, between 150 m isobath and 1° longitude offshore of the 150 m isobath) water properties, including salinity (S'_{slope}), temperature (θ'_{slope}), and fraction of PEW (f'_{PEW}), did not vary nearly as much as properties on the shelf: the variance in shelf water properties was about 10 times the variance in slope water properties, and variance in slope water properties are contained within the scatter of shelf water properties (Figs. 5, 6, 7). Additionally, while S'_{slope} and θ'_{slope} were weakly correlated ($R^2 = 0.30 \pm 0.07$; not significant at 45°N or 48°N), they display the opposite relationship, varying from cold, fresh water to warm, salty water (Figure 2.6b). This relationship suggests that variation in slope water properties is driven by changes in water origin or advection along isopycnal surfaces, like alongcoast advection or changes in the composition of the CUC. This incompatibility in temperature-salinity relationships between shelf and slope water would explain why neither S'_{slope} nor f'_{PEW} were significantly correlated with S'_{shelf}

(R^2 = 0.04 ± 0.04, R^2 = 0.01 ± 0.01, respectively), while θ'_{shelf} and θ'_{slope} were significantly correlated (R^2 = 0.16 ± 0.04; Table 2.2). Therefore, interannual variability in slope water composition does not appear to be the primary driver of variability in shelf salinity and temperature. This is not necessarily the case for other tracers with different vertical and alongcoast gradients, however, and we consider the implications of these temperature/salinity patterns for dissolved oxygen and dissolved inorganic carbon in Section 2.4.3 below.

From the results of the Generalized Linear Model recreation of the shelf salinity record, it can be concluded that together, interannual variability in both local and remote alongshore wind stress and in depth of the CUC core account for more than half of the interannual variability in shelf water salinity. Variability in local and remote wind stress represent the variability in the strength and persistence of upwelling, with stronger upwelling leading to saltier shelf water. The vertical position of the CUC in the water column might also reflect variability in the alongshore wind patterns because the CUC is, in part, driven by the gradient in alongshore wind stress. Hickey et al. (2016) highlight 2004, a year with warmer and fresher shelf water and a shallower, warmer, and fresher CUC, and link these anomalies to weaker remote and local winds along the coast and a loss of the alongshore wind stress gradient. Thus, we conclude that variability in shelf water properties is largely caused by variability in local and remote wind stress, both directly and through the wind's role in setting the vertical position of the CUC.

As discussed previously, there is a significant, though weak, correlation between CUC core depth and shelf salinity in most, but not all, of the model domain. This correlation is strongest near the boundaries and weakens in the model interior, with no significant correlation at 46˚N and 47˚N (R^2 = 0.08 and 0.03, respectively). The lack of significant correlation at 46˚N and 47˚N may be due to local topography, including shelf break canyons, or other local shelf processes. While canyons in the region, specifically the Quinault Canyon (46˚N) and Astoria Canyon (47˚N), enhance upwelling to the shelf, the development of the CUC can shut down this enhancement later in the upwelling season, except during periods of wind relaxation (Connolly & Hickey, 2014; Hickey, 1989, 1997), to an extent that we speculate could depend on CUC core depth. This complicated interaction between the CUC and enhanced canyon upwelling, as well as the highly three-dimensional circulation in the region overall, makes it difficult to isolate the exact cause of the reduced correlation.

While anomalies in shelf salinity (S'_{shelf}) are significantly correlated with variability in the depth of the CUC core ($z'_{26.5}$), they are not significantly correlated with anomalies in slope water composition, in particular, fraction of PEW (f'_{PEW}) and salinity (S'_{slope}). This lack of correlation is consistent with the fact, as noted above, that temperature and salinity anomalies have incompatible relationships on the shelf and slope (Figure 2.6). Consequently, on the interannual timescale, the vertical position of the CUC might matter more to shelf water properties than its composition. However, it is possible that other local processes could be obscuring the direct influence of slope water, a possibility supported by the link between slope and shelf water origin through large-scale advection, as discussed in the next section (2.4.2).

2.4.2 *Large-scale alongcoast advection*

The correlation of slope (150 m to 500 m depth; between 150 m isobath and 1˚ longitude offshore of 150 m isobath) and shelf (bottom half of the water column between 40 m and 80 m isobaths) water shows that both are affected by large-scale advection of water through the northern and southern boundaries ($f'_S{}^{slope}$ and $f'_S{}^{shelf}$, $R^2 = 0.43 \pm 0.10$, excluding 44˚N; Figure 2.12). Furthermore, slope and shelf water properties are more strongly linked interannually through large-scale advection processes north and south ($f'_S{}^{slope}$ and $f'_S{}^{shelf}$, $R^2 = 0.43 \pm 0.10$; excluding 44˚N; Figure 2.12) than they are directly linked to each other through their composition (S'_{slope} and S'_{shelf}, $R^2 = 0.04 \pm 0.04$, not significant).

Freeland et al. (2003) measured colder and fresher water between 30 and 150 m depth in summer 2002 along both the Newport Hydrographic Line and Line-P, suggesting an intrusion of subarctic water at depths spanning both the mid-shelf and part of the upper slope. They attribute this invasion of northern water to a stronger equatorward California Current and weaker poleward Alaska and Davidson Currents during spring 2002, although variability in downwelling and mixing during the winter, as well as enhanced flow of the North Pacific Current, may have also played a role.

At more northern latitudes (47-48°N), northern water is evident in both shelf and slope water, but at the southern end of the domain (44°N), Lagrangian results showed that northern water is more present on the shelf than on the slope (Figure 2.11). Nevertheless, on the slope, intrusions of northern water can extend south to 45˚N so that in some years, the WA slope water is not composed of southern water. For example, there is much more northern deep water present on the slope at 47˚N in September 2004 than there was in September 2007, when southern water dominates the region (Figure 2.4). Similarly, Rivas and Samelson (2011), using a Lagrangian analysis in a different model, found that north of Cape Blanco (~43˚N), there is more water of northern origin in the Oregon upwelling zone (water column east of the 200 m isobath) than water of southern origin.

Interannual anomalies in shelf salinity and the fraction of southern water on the shelf were not significantly correlated at the 95% confidence level (S'_{shelf} and $f'_S{}^{shelf}$, $R^2 < 0.07$), nor were interannual anomalies in wind stress and fraction of southern water on the shelf or slope ($\tau'_y{}^{local}$,

$\tau'_y{}^{remote}$, $f'_S{}^{shelf}$, and $f'_S{}^{slope}$, $R^2 < 0.06$). Somewhat surprisingly, interannual anomalies in fraction of PEW and fraction of southern water over the slope were also not significantly correlated (f'_{PEW} and $f'_S{}^{slope}$, $R^2 = 0.11 \pm 0.06$), despite the fact that both statistics attempt to represent the same feature: variations in the California Undercurrent. Changes in f_{PEW} might occur through processes like mixing and eddy shedding since f_{PEW} is calculated from temperature and salinity. When Thomson and Krassovski (2010) mapped the CUC by its PEW signature from Oregon to Alaska, they saw a steady, poleward decrease in f_{PEW} through along-isopycnal mixing. Pierce et al. (2000) describes examples of eddies shedding from the CUC, and Pelland et al. (2013) estimates that this generation of anti-cyclonic eddies, or "cuddies", accounts for about 44% of heat and salt loss as the CUC moves poleward. However, $f_S{}^{slope}$ on the slope cannot be altered through these processes due to the methods of particle tracking: when "southern" model particles mix with other water, they are not transformed into "northern" particles. Likewise, if PEW is advected north with the CUC and then re-enters the model domain from the north during a subarctic intrusion, the Lagrangian analysis would not count this PEW as "southern" in the calculation of f_S.

2.4.3 *Applications to biology and chemistry*

As seen in the GLM analysis, variability in local and remote wind stress and in CUC depth contribute to anomalies in the density of water over the shelf. These processes are all part of upwelling variability, which includes strength, vertical structure, and apparent source depth of upwelling, and may lead to changes in shelf water chemistry. The mean change in upwelling variability and its subsequent effects on salinity, oxygen, and dissolved inorganic carbon (DIC) concentrations are summarized in Table 2.3. We denote anomalies associated with upwelling variability, or across-isopycnal or vertical variation, with a subscript z, in contrast to anomalies associated with alongcoast variations (subscript y). Because the variation in shelf salinity is almost entirely across-isopycnal, ΔS_z is approximately equal to the magnitude of standard deviation of shelf salinity (ΔS_z = 0.23 psu; Table 2.3). The scale of variation in shelf oxygen (ΔO_z) associated with across-isopycnal salinity/temperature variation can be estimated as follows:

$$\Delta O_z = \frac{\partial O}{\partial z} \Delta z \tag{2.1}$$

where $\partial O/\partial z$ is the gradient of oxygen with depth and Δz is the variation in depth of upwelling source water reflected in ΔS_z. Rewriting in terms of the vertical salinity gradient $\partial S/\partial z$,

$$\Delta O_z = \frac{\partial O}{\partial z}\left(-\frac{\partial S}{\partial z}\right)^{-1} \Delta S_z \tag{2.2}$$

Using mean dissolved oxygen profiles along the Newport Hydrographic Line (44.65˚N) in Pierce et al. (2012) and salinity profiles from the model, $\Delta O_z \approx -28$ µmol kg^{-1}, with a decrease in oxygen concentration with stronger upwelling, which might include deeper apparent depth of upwelled water, stronger upwelling-favorable winds, or shoaling CUC (Table 2.3). This value is comparable to observed and modeled interannual anomalies in dissolved oxygen on the Washington shelf (Connolly et al., 2010; Siedlecki et al., 2015).

Table 2.3. Change in salinity (*S*) and inferred change in oxygen (O_2) and dissolved inorganic carbon (DIC) due to vertical advection (Δ_z) and alongcoast advection (Δ_y). Signs reported are for positive change in Δ_z and Δ_y.

	Δ_z (stdev)	Δ_y (stdev)	Δ_y (2004 event)[10]
S (psu)	0.23	0.01	0.03
O_2 (μmol kg^{-1})	-28	-6	-16 ± 6
DIC (μmol kg^{-1})	29	9	25 ± 9

Likewise, the scale of anomalies in DIC associated with observed anomalies in shelf salinity can be estimated as

$$\Delta DIC_z = \frac{\partial DIC}{\partial z}\left(-\frac{\partial S}{\partial z}\right)^{-1} \Delta S_z \tag{2.3}$$

Combining mean profiles of DIC along the Newport Hydrographic Line (44.65˚N) from Feely and Sabine (2011) with model salinity, $\Delta DIC_z \approx 29$ μmol kg^{-1}, with an increase in DIC concentration with stronger upwelling (Table 2.3). These results suggest that depending on the vertical structure of the water column, stronger upwelling could raise the hypoxic boundary (DO < 60 μmol kg^{-1}) and the aragonite saturation horizon ($\Omega_{arag} < 1$) higher in the water column than is tolerable for native organisms.

Interannual variability in the north-south source of water over the slope and shelf may also translate into changes in chemistry. Scales of variation in alongcoast lateral advection and its subsequent effects on salinity, oxygen, and DIC concentrations, are estimated in Table 2.3. Because the variation in slope salinity is contained within the scatter of the shelf salinity, we

---

[10] Gradient in slope water across affected latitudes (45˚N – 48˚N).

estimate ΔS_y on the shelf as the standard deviation of slope salinity ($\Delta S_y = 0.01$ psu; compare Figs. 6a, 6b). By analogy with the ΔO_z calculation above,

$$\Delta O_y = \frac{\partial O}{\partial y}\left(-\frac{\partial f_{PEW}}{\partial y}\right)^{-1} \Delta f_{PEW_y} \tag{2.4}$$

where $\partial O/\partial y$ and $\partial f_{PEW}/\partial y$ are the gradients in oxygen and f_{PEW} with latitude and Δf_{PEW} is the scale of variation in f_{PEW} observed in the model. Using mean oxygen fields along the $\sigma_t = 26.5$ kg m^{-3} isopycnal from the World Ocean Atlas (Garcia et al., 2013), we find that $\Delta O_y \approx -6$ µmol kg^{-1}, with southern water carrying less dissolved oxygen than northern water (Table 2.3). This value represents the expected variation in oxygen concentrations in upwelling source water associated with the alongcoast advection anomalies observed in the model analysis.

Accordingly, on average over the time series, the expected variation in oxygen due to along-isopycnal advection (ΔO_y) is small compared to that due to upwelling variability (ΔO_z), but this is not necessarily the case for individual events. The northern intrusion event in 2004, evident in negative f_{PEW} anomalies from 45˚N to 48˚N (Figure 2.7), corresponded to an increase in dissolved oxygen of about 16 ± 6 µmol kg^{-1}, as well as decrease in salinity by about 0.03 psu (Table 2.3). This change in oxygen is similar to the interannual variations in source water oxygen concentration (12 µmol kg^{-1}) observed at Newport, Oregon by Peterson et al. (2013), and is comparable to the effect (ΔO_z) of weaker upwelling, such as shoaling of apparent source depth of upwelled water or deepening of the CUC by 50 m. Note that the effect of the 2004 intrusion event on salinity is still quite small compared to the typical ΔS_z (Table 2.3).

Similarly, the scale of anomalies in DIC associated with alongcoast lateral advection can be estimated as

$$\Delta DIC_y = \frac{\partial DIC}{\partial y}\left(-\frac{\partial f_{PEW}}{\partial y}\right)^{-1} \Delta f_{PEW_y} \tag{2.5}$$

Using mean DIC fields along the $\sigma_t = 26.5$ kg m^{-3} isopycnal from Feely and Sabine (2011), we find that $\Delta DIC_y \approx 9$ µmol kg^{-1}, with southern water carrying more DIC than northern water (Table 2.3). Like ΔO_y, on average ΔDIC_y is smaller than ΔDIC_z, but individual events can yield ΔDIC_y of similar scale as ΔDIC_z. In the case of the 2004 intrusion of northern water, the negative f_{PEW} anomalies from 45°N to 48°N (Figure 2.7) corresponded to a decrease in DIC by about 25 ± 9 µmol kg^{-1} (Table 2.3).

Thus, while on average, ΔO_z and ΔDIC_z are greater than ΔO_y and ΔDIC_y, large-scale intrusion events, such as the northern intrusion event in 2004, can yield ΔO_y and ΔDIC_y of similar scale as mean ΔO_z and ΔDIC_z. Furthermore, the scale of ΔO_y of these intrusion events is of similar size as interannual variation in source water oxygen concentrations described in Peterson et al. (2013). The interannual anomalies in oxygen in Peterson et al. (2013) were statistically linked to changes in NPGO, with positive oxygen anomalies in years with positive NPGO values. The NPGO is driven by changes in the North Pacific Current, with more northern water transported into the region in positive NPGO years. This mechanism is consistent with the idea that there is more oxygen present in the NCCS when there is more northern water advected into the region (Table 2.3). Overall, the model supports the statistical relationship found by Peterson et al. (2013) and provides a model-based map of what changes in advection by the NPGO might look like.

While the length of the time series from the model prohibits systematic comparison with indices of climate-ocean decadal variability, the mechanisms described in this analysis, particularly changes in the depth of the CUC and alongshore advection, are likely important mechanistic links between climate-ocean decadal modes and the shelf. With the positive phase of the Pacific Decadal Oscillation (PDO; Chhak and Di Lorenzo (2007)), North Pacific Gyre Oscillation (NPGO; Di Lorenzo et al. (2008)), and El Nino-Southern Oscillation (ENSO; Jacox et al. (2015); Schwing et al. (2002)), the depth of source water to the shelf is shallower, and thus (we might expect in general) poorer in nutrients and oxygen. With the negative phase of each of these indices, the opposite is true. With PDO (Keister et al., 2011) and ENSO (Kosro, 2002), the positive phase of each would lead to more southern source water in the region, with El Nino leading to enhanced poleward flow over the slope and shelf, as observed in Huyer and Smith (1985). However, with NPGO, the positive phase leads to more northern source water in the region, as well as more oxygen (Peterson et al., 2013). Therefore, with respect to nutrients and oxygen, the vertical and alongshore effects of the NPGO reinforce each other, while with both PDO and ENSO the effects on source water depth and advection are likely to counteract each other. The reinforcement of these effects by the NPGO is likely the reason for the statistical link between oxygen concentrations and NPGO, but not oxygen and PDO, described by Peterson et al. (2013). Longer model or observational time series are required to test this conceptual picture.

2.5 CONCLUSIONS

Using a ROMS hindcast model spanning 2003-2009, as well as intensive particle tracking, we studied the interannual variability of shelf water properties with the goal of understanding how the composition and depth of the California Undercurrent, alongcoast advection, as well as local and remote wind stress, influence this variability. The main conclusions for this analysis are:

1. *Alongcoast interannual variability in both mid-shelf bottom water and upper slope water properties vary little across 800 km of latitude.*

   Over the whole study domain, there is very little variance between latitudes in temperature and salinity of shelf water, with standard deviation across latitudes in temperature of 0.70 ± 0.04˚C, and in salinity of 0.23 ± 0.02 psu (Fig 5), with more variance in winter than in summer. This result is consistent with the results of Hickey et al. (2016) based on data from sensors moored mid-shelf across a similar range of latitudes. Similarly, temperature, salinity, fraction of PEW, and depth of the 26.5 kg m^{-3} isopycnal on the slope also experienced very little variance in their interannual anomalies between latitudes, with average standard deviation across latitudes in temperature of 0.08 ± 0.02˚C, in salinity of 0.01 ± 0.003 psu, in fraction of PEW of 0.01 ± 0.002, and in depth of the 26.5 kg m^{-3} isopycnal of 24 ± 3 m (Figure 2.7). There is an exception to this pattern on slope in 2004. Lagrangian analysis on the slope suggests that the poleward gradient of cold, fresh water on the slope was due to an intrusion of northern water (Figs. 4, 11f-j).

2. *Together, interannual variability in local and remote wind stress and in depth of the CUC explain more than half of the interannual variability in mid-shelf bottom water salinity.*

Interannual anomalies in local wind stress and in remote wind stress are significantly correlated with interannual anomalies in shelf salinity, with stronger wind stress leading to saltier shelf water ($\tau'_y{}^{local}$ and S'_{shelf}, $R^2 = 0.44 \pm 0.10$; Figure 2.8a; $\tau'_y{}^{remote}$ and S'_{shelf}, $R^2 = 0.34 \pm 0.09$; Figure 2.8b). Interannual anomalies shelf salinity were also correlated with interannual anomalies in the depth of the 26.5 kg m^{-3} isopycnal ($z'_{26.5}$ and S'_{shelf}, $R^2 = 0.18 \pm 0.05$ for 44˚N, 45˚N, and 48˚N; Figure 2.8c). To account for cross-correlation among the local and remote wind stress, and in depth of the 26.5 kg m^{-3} isopycnal, a generalized linear model (GLM) was constructed using the interannual anomalies in these three variables to reproduce interannual anomalies in shelf salinity. The resulting GLM suggests that together, interannual anomalies in local and remote wind stress and in depth of the 26.5 kg m^{-3} isopycnal account for more than half the variability in shelf salinity (Generalized Linear Model mean over all latitudes: $R^2 = 0.58 \pm 0.08$). The best fit for this GLM was at 48˚N (Figure 2.9).

3. *The mid-shelf bottom and upper slope have incompatible relationships between temperature and salinity anomalies.*

Interannual anomalies in salinity and temperature on the shelf are significantly correlated with an inverse relationship (S'_{shelf} and θ'_{shelf}, $R^2 = 0.72 \pm 0.05$; Figure 2.6a), while on the slope, salinity and temperature interannual anomalies are significantly correlated with a direct relationship (S'_{slope} and θ'_{slope}, $R^2 = 0.30 \pm 0.07$ for 44˚N, 46˚N, and 47˚N; Figure 2.6b). Furthermore, the magnitude of variation in slope water properties is about one tenth that of shelf water properties, with the scale of slope variation (Figure 2.6b) fitting into the scatter around the primary axis of variation on the shelf (Figure 2.6a). The relationship on the shelf suggests cross-isopycnal variation associated with upwelling dynamics, while the relationship on the slope suggests along-isopycnal variation in water origin.

4. *The vertical position of the CUC might affect shelf water properties more than variations in its composition on the interannual timescale.*

As discussed above, the patterns of temperature and salinity on the shelf and slope have opposite relationships. Furthermore, changes in CUC properties appear to have a minor effect on shelf water properties (f'_{PEW}, S'_{slope} and S'_{shelf}, $R^2 = 0.03 \pm 0.03$), as compared with the vertical position of the CUC ($z'_{26.5}$ and S'_{shelf}, $R^2 = 0.18 \pm 0.05$ for 44°N, 45°N, and 48°N; Figure 2.8c).

5. *The origins of both mid-shelf bottom water and upper slope water are affected by large-scale alongcoast advection.*

Lagrangian analysis of origin of shelf and slope water show that both are affected by large-scale alongcoast advection of water from the north and south (f'^{slope}_{S} and f'^{shelf}_{S}, $R^2 = 0.43 \pm 0.10$, excluding 44°N; Figure 2.12). Intrusions of northern water are evident on both the shelf and slope, and the frequency of these intrusions varies interannually. These changes in water origin can be indicative of the characteristics of that water, with warm, salty water carried from the south and cold, fresh water carried from the north. In particular, the poleward gradient in cold, fresh water over the slope in 2004 found in the Eulerian analysis (Figure 2.7) coincides with an intrusion of northern water in the Lagrangian analysis (Figure 2.4, Figure 2.11f-j).

6. *Particularly large northern or southern intrusion events can cause changes in shelf water chemistry of the same magnitude as those caused by typical upwelling variability.*

   On average, changes in oxygen concentration (-28 µmol kg^{-1}) and in dissolved inorganic carbon concentration (29 µmol kg^{-1}) through upwelling variability (i.e., variability in strength, vertical structure, and apparent source depth of upwelling) are larger than changes in oxygen concentration (-6 µmol kg^{-1}) and in dissolved inorganic carbon concentration (9 µmol kg^{-1}) through along-isopycnal advection (i.e., north-south lateral alongcoast advection). However, unlike the effect these processes have on salinity, large-scale intrusion events, like the intrusion of northern water during 2004, can have an effect on oxygen concentrations and on dissolved inorganic carbon concentrations similar to that of upwelling variability. During the intrusion event in 2004, oxygen concentrations increased, on average by 16 ± 6 µmol kg^{-1}, which is similar scale to the change in oxygen concentration associated with typical upwelling variability, while dissolved inorganic carbon concentrations decreased by about 25 ± 9 µmol kg^{-1}. Furthermore, the magnitude of this intrusion event is similar to the interannual variation in oxygen concentrations (12 µmol kg^{-1}) of source water that are linked to NPGO variability, as measured by Peterson et al. (2013).

Thus, it is through event-scale alongcoast advection and typical upwelling variability, including strength, vertical structure, and apparent source depth of upwelling, rather than the composition of the slope water itself, that upper slope water properties and mid-shelf bottom water properties are primarily connected on longer-than-seasonal scales. While on average, upwelling variability is expected to have a greater impact on oxygen and dissolved inorganic carbon concentrations than does alongcoast advection, large-scale alongcoast intrusion events can have an effect comparable to that of typical upwelling variability. This suggests that event-scale alongcoast advection and upwelling variability can have comparable effects on shelf and slope water chemistry. The precision of this conclusion is limited by a relatively short record. Future investigation into longer-term variability and trends in the northern CCS must carefully consider both the vertical structure and large-scale alongcoast transport of waters over the linked shelf-slope system.

2.6 ACKNOWLEDGEMENTS

Special thanks to Barbara Hickey for guidance and extensive help with analysis and editing, to Samantha Siedlecki, Sarah Giddings, and Ryan McCabe for useful discussions, to LuAnne Thompson and Simone Alin for guidance, and to David Darr for computer cluster administration and support. This chapter is co-authored by Neil S. Banas and Parker MacCready. Access to model run setup files and derived output used in this chapter are available upon request as described here: iodlabs.ucsd.edu/sgiddings/PNWTOX/contact.html. These model setup files and output data are curated by MacCready on MacCready's server at UW and will remain curated for at least 5 years. H. Stone was supported by an Integrative Graduate Education and Research Traineeship (IGERT) grant as part of the University of Washington’s IGERT Program on Ocean Change, and by a National Science Foundation (NSF) Graduate Research Fellowship. P. MacCready and N. Banas were supported by the Coastal Ocean Program of the National Oceanic and Atmospheric

Administration (NA09NOS4780180) and the National Science Foundation (OCE0942675) as part of the Pacific Northwest Toxins (PNWTOX) project. In addition, N. Banas was supported by the National Aeronautics and Space Administration (NNX13AL28G). This is contribution 902 and 15 of the ECOHAB and PNWTOX programs. The findings and conclusions are those of the authors and do not necessarily reflect those of NSF, NOAA, NASA, or the Department of Commerce.

Chapter 3. LINKING CHLOROPHYLL CONCENTRATION AND WIND PATTERNS USING SATELLITE DATA IN THE CENTRAL AND NORTHERN CALIFORNIA CURRENT SYSTEM

3.1 INTRODUCTION

Eastern Boundary Upwelling Systems like the California Current System (CCS) are highly productive regions due to the abundant nutrients largely supplied to the euphotic zone through coastal upwelling. In the CCS, this upwelling is driven by equatorward, alongshore winds that induce Ekman transport offshore, pulling nutrient-rich water from depth, while downwelling is driven by poleward alongshore winds that drive Ekman transport onshore. Throughout much of the CCS, the upwelling regime persists throughout the entire year, with downwelling occurring only during wind relaxation events and predominantly in the Northern CCS. Upwelling typically occurs during the summer into the fall and downwelling occurs in winter in the Northern CCS; still, event-scale (several days) upwelling and downwelling can occur within each season (Hickey, 1989). Despite the weak upwelling-favorable winds characteristic of the Northern CCS, it is an especially productive region. This unusually high productivity has been speculatively attributed to a combination of wind patterns, geography, and freshwater inputs, all of which ultimately lead to abundant nutrients in the region (Hickey & Banas, 2008). Geographically, there are numerous shelf-break canyons in the region that enhance upwelling, allowing more nutrients to reach the euphotic zone (Allen & Hickey, 2010; Connolly & Hickey, 2014). In addition, the wide continental shelves of Washington and Oregon allow phytoplankton ample time to bloom as they are transported offshore (Strub et al., 1991). Remote wind forcing (defined here as alongshore winds at and south of 42˚N), through coastal-trapped waves, plays a large role in upwelling in the

Northern CCS (Battisti & Hickey, 1984; Chapman, 1987; Connolly et al., 2014; Hickey et al., 2006; Hickey et al., 2016; Stone et al., 2018 [Chapter 2]). Lastly, freshwater supply, particularly outflow from the Salish Sea and, on a smaller scale, the Columbia River, brings additional nutrients to the region (Davis et al., 2014). These additional, non-upwelling-derived nutrient sources are essential for higher production with weaker wind speeds observed in this region but may complicate the relationship between phytoplankton biomass and wind.

Due to the nutrient supply the shelf and euphotic zone receives via upwelling-favorable winds, one might expect that stronger winds facilitate larger phytoplankton blooms. However, previous studies suggest that productivity is limited when there are extremely high winds (e.g., Cury and Roy (1989); Ware (1992)). Using an idealized mixed-layer conveyor (MLC) model, Botsford et al. (2003) found that if upwelling winds are too strong, phytoplankton are swept off the shelf before they can utilize all of the upwelled nutrients, though why productivity is not sustained past the shelf break is unclear, as discussed in Section 3.4. Thus, the relationship between wind speed and productivity is described as "dome-shaped" (Botsford et al., 2003), peaking at some optimal wind speed and then falling off at higher wind speeds. This optimal wind speed reflects the amount of time that the parcel takes to cross the shelf and thus is related to shelf width. More specifically, the Botsford et al. (2003) relationship represents the response of shelf chlorophyll concentration to the two independent influences of wind stress on shelf chlorophyll. First, upwelling-favorable wind stress supplies shelf with nutrients; therefore, stronger upwelling-favorable wind results in more nutrients supplied to the shelf and higher shelf chlorophyll concentrations (red dashed arrow; Figure 3.1). Second, upwelling-favorable wind stress also induces Ekman transport offshore, and this cross-shelf export includes transport of phytoplankton from the shelf to the offshore region. Therefore, stronger upwelling-favorable winds result in more cross-shelf export and lower shelf chlorophyll concentrations (blue dashed arrow; Figure 3.1). The Botsford et al. (2003) relationship represents the balance of these two mechanisms, with the resulting dome-shaped relationship between wind stress and shelf chlorophyll concentration depicted by the black curve in Figure 3.1.

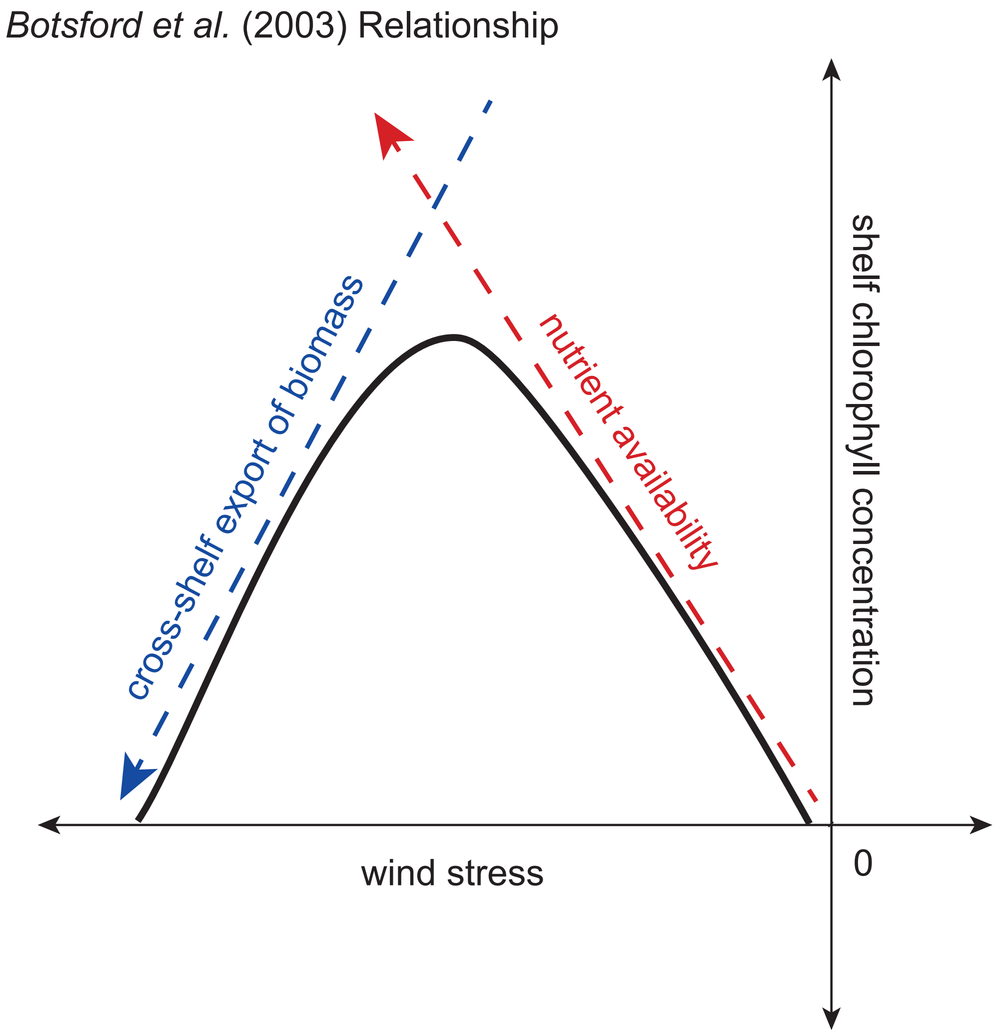

Figure 3.1. A conceptual diagram representing the Botsford et al. (2003) relationship. The relationship between shelf chlorophyll concentration and upwelling-favorable wind stress (black curve) results from the balance between the chlorophyll response to nutrient availability (red dashed arrow) and the chlorophyll response to cross-shelf export of biomass (blue dashed arrow).

In a later MLC model study, Botsford et al. (2006) found that variable winds (i.e. relaxation events) prolong time of phytoplankton on the shelf, allowing for more production and an increase in the optimal wind speed. Using a similar MLC model based on conditions observed in the CCS, Yokomizo et al. (2010) found that the optimal wind pattern for maximum productivity is wind that varies over a period equal to the shelf width divided by the cross-shelf velocity that results from the peak wind speed in the Botsford et al. (2003) relationship, and with the same mean cross-shelf velocity over the period. This finding implies that the optimal wind speed for maximum productivity varies with latitude and shelf width. More recently, in a more complex simulation built upon a traditional ECOPATH food web model that incorporates upwelling dynamics, Ruzicka et al. (2016) found that the dome-shaped relationship with upwelling strength exists across trophic levels. Specifically, their study found that phytoplankton, zooplankton, and secondary consumer fish all exhibited this pattern.

Furthermore, observational studies of the CCS have tended to corroborate the general suggestion in these model studies that increased upwelling does not lead to increased productivity in a simple, linear way. In an important paper, Ware and Thomson (2005) used satellite data spanning the whole CCS to characterize the mean distribution of productivity in CCS. They found that while Ekman transport offshore due to upwelling decreased with increasing latitude, productivity increased, with the most productivity found off of WA and BC where upwelling winds were the weakest. In a 2015 paper, Evans et al. attribute the failed bloom in July 2008 in Oregon on intense upwelling-favorable winds that pushed phytoplankton offshore before they could respond to upwelled nutrients. Based on observations within the CCS as part of the "Wind Events and Shelf Transport" program (WEST), Largier et al. (2006) found that increased upwelling-favorable wind strength leads to increased nutrient supply but excessive upwelling-favorable winds have a negative effect on productivity and lead to increased turbidity, increased offshore phytoplankton transport, deep mixing, and increased ammonium, which decreases nitrate uptake. However, when the duration of upwelling or relaxation events are on the order of phytoplankton blooms (several days), diatom blooms dominate the shelf region; when these events are longer, the shelves accumulate detritus and the phytoplankton move offshore. These findings suggest that the ideal conditions for productivity would be strong upwelling-favorable winds to bring nutrients to the euphotic zone, followed by a period of wind relaxation, with timescales on the order of phytoplankton blooms. This wind relaxation helps retain phytoplankton on the shelf, thus allowing the phytoplankton ample time to utilize the nutrients. Along the same lines, Hickey and Banas (2008) hypothesized that the intermittency of the winds in the Northern CCS was itself one of the drivers behind that region's very high phytoplankton standing stock, with the intermittent winds interacting with freshwater plumes to boost retention and accumulation.

In a recent paper, Jacox et al. (2016) investigated bottom-up controls on productivity in the CCS using chlorophyll concentration observations from satellite combined with a realistic model. Like the previously described studies, their study used wind stress over the "nearshore" region (within 75 km of shore); however, they also included subsurface nitrate concentrations and the offshore region (75 – 300 km from shore) in their analysis. Their results suggest that in the nearshore region, maximum phytoplankton biomass results from moderate wind stress and high subsurface nitrate concentration, while in the offshore region, phytoplankton biomass is highly correlated with subsurface nitrate concentration. Offshore biomass is likely the result of advection of phytoplankton and nutrients from the nearshore region, although it is not significantly correlated with wind stress. Because of the non-linear interactions between wind strength and nutrient concentration, the relationship between productivity and one of these variables is dependent on the other and Jacox et al. (2016) found that one could not explain phytoplankton biomass by either one alone, nor with a combined metric such as vertical nitrate flux. The amount of nitrate available to upwell limits the maximum biomass attainable at a given wind stress, though this relationship varies across the ranges of wind stress and subsurface nitrate concentrations. These findings suggest a view in which in the nearshore region, phytoplankton biomass is dependent on both upwelling strength and characteristics of the upwelling water, while offshore phytoplankton biomass is only dependent on the characteristics of the upwelled water.

In past studies, productivity, including primary and higher trophic levels like fish, was often found to be correlated with indices representing upwelling variability, particularly the Upwelling Index (UI) (Bakun, 1973; Schwing et al., 1996) and Cumulative Upwelling Index (CUI) (Pierce et al., 2006) (e.g., Botsford and Wickham (1975); Ware and Thomson (2005)). Overall, these indices are able to capture wind patterns in order to characterize the strength and variability of upwelling, but do not incorporate any measure of how characteristics of upwelling sourcewater, particularly its nutrient concentration, may have changed. However, as suggested by Jacox et al. (2016), both wind stress and subsurface nitrate concentrations are needed to characterize bottom-up controls on productivity. Recently, Jacox et al. (2018) created indices that include both the physical and nutrient dynamics: CUTI and BEUTI. CUTI (Coastal Upwelling Transport Index) represents the rate of vertical volume flux, while BEUTI (Biologically Effective Upwelling Transport Index) represents the vertical flux of nitrate into the mixed layer.

While there have been numerous investigations into the relationship between phytoplankton productivity and biomass and wind on the shelf, few have extended their analysis into the Northern part of the California Current System. Fewer still have studied the influence of retention on this relationship. Using chlorophyll concentration and wind stress derived from satellite observations, we analyze the relationship between chlorophyll concentration and wind patterns in the Central and Northern CCS to see if the dome-shaped Botsford et al. (2003) relationship applies to the CCS as a whole and whether the Northern CCS is comparable or exhibits different behavior. In addition, we investigate how retention affects the relationship between chlorophyll concentration and wind stress in the Northern CCS using results from particle tracking experiments conducted in a model of the Northern CCS.

3.2 METHODS

3.2.1 *Satellite chlorophyll concentration and wind stress*

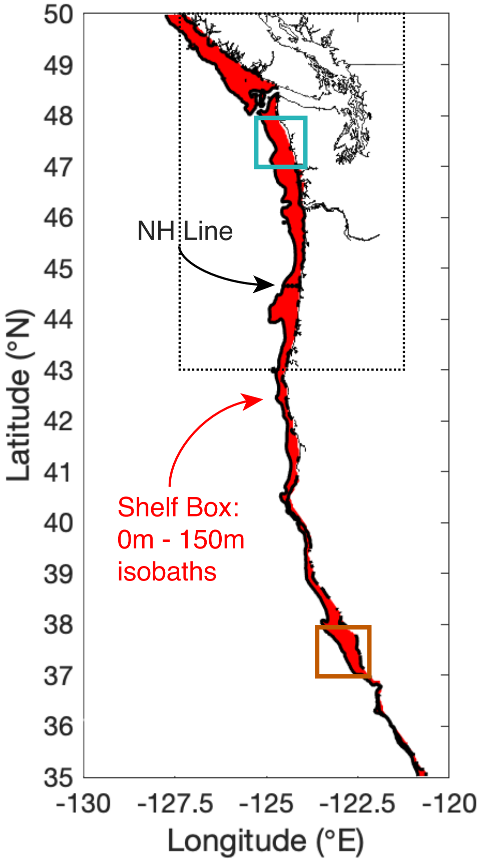

Figure 3.2. Study domain for the chlorophyll concentration and wind stress satellite data. The shelf (0 – 150 m isobaths) is shown in red. The *Cascadia* model domain used during the particle tracking experiments is outlined by the dashed line. Examples of latitude shelf boxes are shown in orange and cyan for 37.5˚N (37˚N – 38˚N) and 47.5˚N (47˚N – 48˚N), respectively. Black dots mark locations along the Newport Hydrographic Line used for satellite chlorophyll validation in Figure 3.4.

For this study, we used chlorophyll concentration from a merged satellite product from the European Node for Global Ocean Colour (GlobColour Project), which combines chlorophyll concentration observations from SeaWiFS (NASA), MODIS (NASA), MERIS (ESA), OLCI-A

(ESA), and VIIRS (NOAA/NASA). The chlorophyll concentration data were 8-day composites spanning 1998 – Present at a 4-km spatial resolution. While only near-surface chlorophyll concentration is estimated by satellite, Frolov et al. (2012) found that depth-integrated chlorophyll is highly correlated with near-surface chlorophyll off of California ($r^2 = 0.9$), and so we will be using chlorophyll concentration as a proxy for phytoplankton biomass in this paper. This analysis focuses on the shelf region (from the coast to the 150 m isobath, shown in red in Figure 3.2). To address spatial variability, the shelf region was split into 1˚ latitudinal bands, over which we took the exponential of the mean of ln(chlorophyll concentration) to obtain a mean that is not as affected by large outliers, resulting in one time series for each degree over our entire domain, 35˚N – 50˚N. This technique is useful, and commonly used, for datasets that are lognormally distributed like chlorophyll concentration (Campbell, 1995). Then 8-day chlorophyll concentration values were compared to 8-day mean wind stress (Figure 3.3). This timescale is appropriate for this analysis as it corresponds to timescales of both an upwelling event (3-10 days) (Beardsley et al., 1987; Hickey, 1979) and phytoplankton response time to upwelled nutrients (3-7 days) (Wilkerson et al., 2006). The 8-day mean wind stress values were derived from QuikSCAT and ASCAT satellite wind velocities from 1˚ longitude offshore following Smith (1988) (NOAA CoastWatch Program and Remote Sensing Systems, Inc.). Data span August 1999 – November 2009 (QuikSCAT) and October 2009 – Present (ASCAT) at a resolution of 0.25˚. These data were then rotated parallel to the coastline throughout the study domain. To correspond with the chlorophyll concentration data, the mean of the wind stress data was taken over the same 1˚ latitudinal bands, with four data points within each band. For this study, we focused on the 2000 – 2019 time period, transitioning from QuikSCAT to ASCAT at November 1, 2009, over much of the Central and Northern California Current System (35˚N – 50˚N). These data were not calibrated to account for the different methods through which QuikSCAT and ASCAT make these measurements. Data from each sensors is differentiated in Figure 3.3 where mean 8-day composite chlorophyll concentrations are plotted against the corresponding mean 8-day wind stresses for each latitude. Bentamy et al. (2012) estimate the difference between wind speed measurements from QuikSCAT and ASCAT to be around 1 m/s, which corresponds to a wind stress of about 0.002 Pa. Given the resolution at which wind stresses are binned in further analysis (0.015 Pa bins; discussed below), we do not expect the difference between measurements from QuikSCAT and ASCAT to significantly affect our results and thus, measurements from QuikSCAT and ASCAT are no longer differentiated in later figures depicting wind stress.

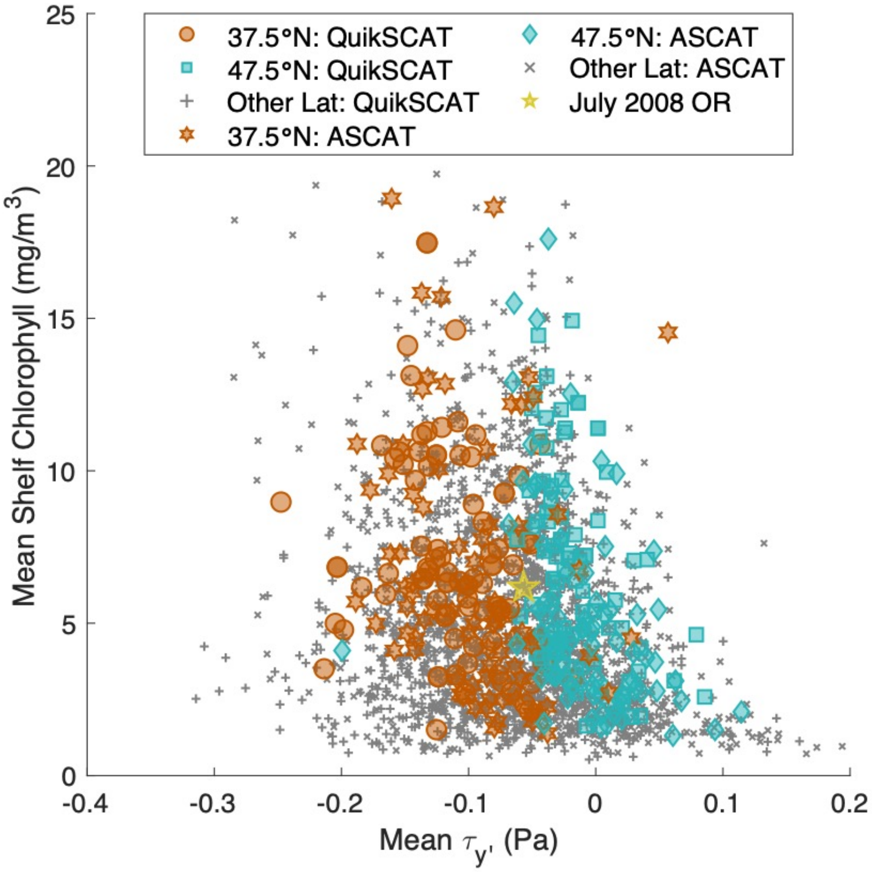

Figure 3.3. Mean 8-day composite shelf chlorophyll concentration plotted against its corresponding wind stress for each latitude from 35.5˚N to 49.5˚N, with a distinction made between wind stresses derived from QuikSCAT measurements (January 2000-October 2009) and ASCAT measurements (November 2009 – December 2019). Data from 37.5˚N (between 37˚N and 38˚N) is shown in orange circles (QuikSCAT) and orange hexagons (ASCAT), and data from 47.5˚N (between 47˚N and 48˚N) is shown in blue squares (QuikSCAT) and blue diamonds (ASCAT). The failed bloom in OR (44.5˚N) in July 2008 (Evans et al., 2015) is depicted by the yellow star. All other latitudes are shown in grey crosses (QuikSCAT) and in grey Xs (ASCAT wind).

The GlobColour satellite product matches well with in-situ observations within the study area. Surface bucket samples from the NOAA Newport Hydrographic (NH) Line (~44.6° N) for the dates of January 2013 to February 2018 were compared to satellite color fields. NH Stations 1, 3, 5, 10, 15, and 20 (black dots in Figure 3.2) were used, which cover the width of the shelf and were sampled bi-weekly most of the year with monthly sampling in winter. Total samples for this time period varied by station from 54-92, with those stations closest to shore being sampled most often. Satellite chlorophyll concentrations were limited to a 1° latitude band centered on 44.6° N. Satellite and NH concentrations show a similar distribution, with a high proportion of log values near zero, a steep decline in the lower tail, and a similar extent of the upper tail (Figure 3.4a). A comparison of the mean of NH station values for each sampling date with the mean of satellite values over the Newport region for the corresponding 8-day period shows good agreement ($r^2 = 0.48$, $p < 0.01$; Figure 3.4b). For satellite wind validation, a recent study by Ribal and Young (2020) found that 10-m wind speed and direction measurements from both QuikSCAT and ASCAT match well with in situ 10-m wind speed and direction measurements from buoys from the National Data Buoy Center ($\rho = 0.9593$ and 0.9404, respectively), though QuikSCAT had a tendency to overestimate high wind speeds (> 15 m/s). This study also compared wind speed measurements from four other satellite scatterometers and found generally good agreement among instruments, so we would expect similar results with these other satellite wind products.

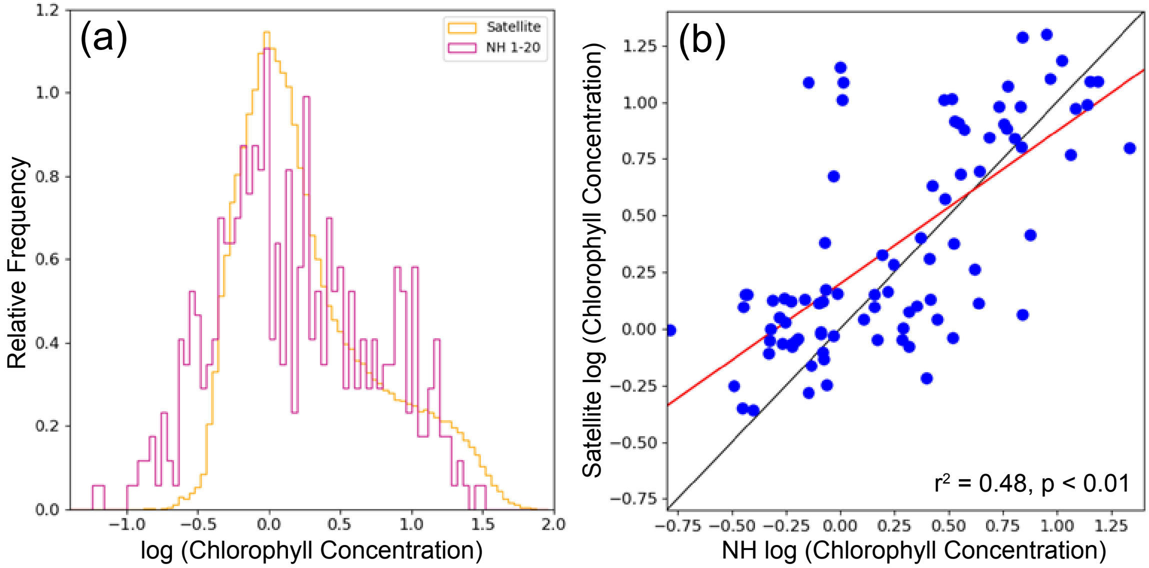

Figure 3.4. Comparison of GlobColour merged satellite product with in-situ measurements taken along the Newport Hydrographic Line (NH) January 2013 through February 2018. Relative frequency histogram, where satellite values are 8-day composites over a 1° latitude band centered on 44.6°N while NH values are individual measurements for each station on each sample date (a). Scatter plot comparing the mean of NH stations sampled on each date with the mean of the satellite field for the Newport region for the corresponding 8-day composite (b), where the red line represents the trendline for the data, with an $r^2 = 0.48$, $p < 0.01$, while the diagonal grey line is 1:1.

Chlorophyll concentrations in each latitude band were binned by wind stress during the upwelling season (March – October). We took the natural log of chlorophyll concentration to calculate the 95% confidence intervals for each 0.015 Pa wind stress bin using the Student's t-test (Emery & Thomson, 2004). Then, we plotted mean chlorophyll concentration vs. wind stress, as shown in the example plot in Figure 3.5, with the mean shelf chlorophyll concentration shown with the solid green line and the high and low 95% confidence intervals shown with the dashed green lines. Wind stress bins whose difference between the high and low 95% confidence intervals was greater than the global mean chlorophyll concentration (4.34 mg/m^3; dashed black line in

Figure 3.5) are colored in red, with the solid red line representing the mean and dashed red lines representing the high and low 95% confidence intervals. These red bins were ignored in the remainder of the analysis. By eliminating bins using these criteria, about 13% of observations are ignored as being too noisy and undersampled to analyze. Each latitude band was processed in this manner. This analysis was also conducted with NCEP Reanalysis winds (Kalnay et al., 1996) in place of QuikSCAT/ASCAT, as well as with various upwelling season lengths with similar results (not shown). In particular, the analysis with NCEP Reanalysis winds showed a similar pattern when plotted against chlorophyll concentrations, though NCEP wind stresses were often lower magnitude than QuikSCAT and ASCAT wind stresses, especially at high wind stresses, a pattern that was also reported in Fewings et al. (2016).

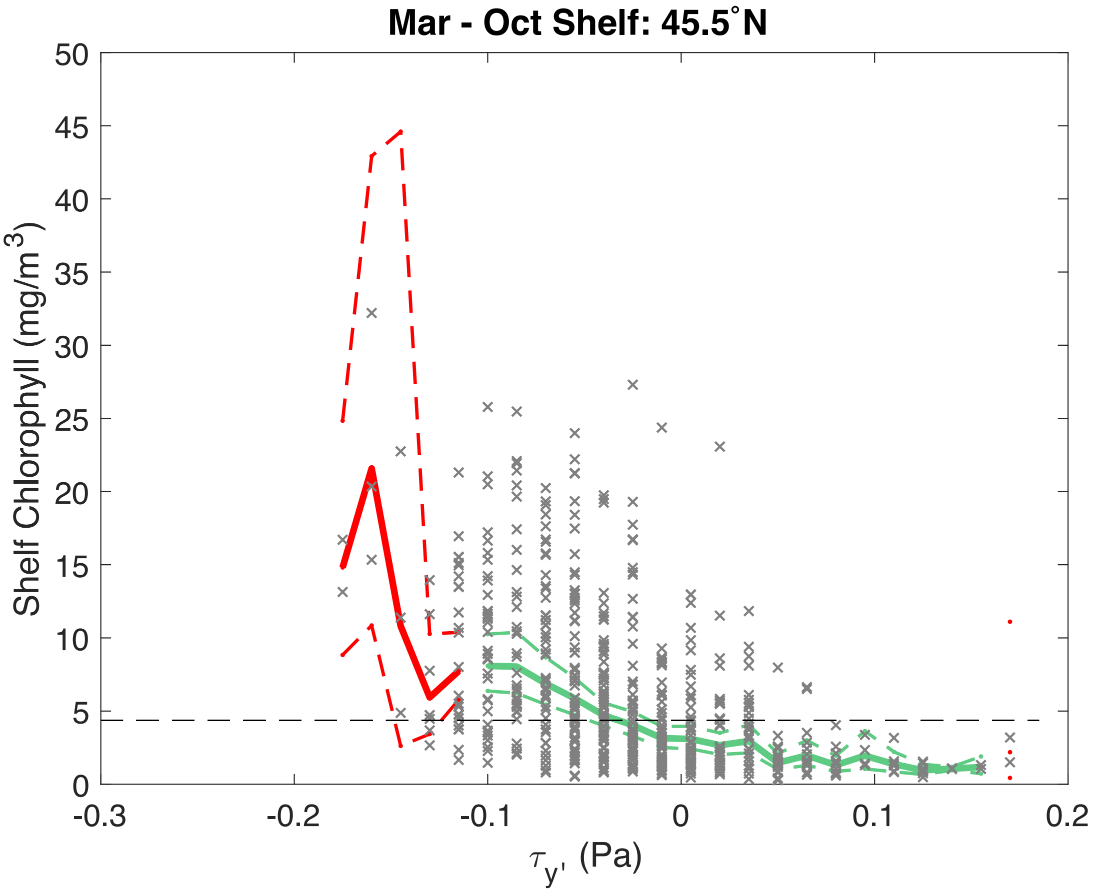

Figure 3.5. Example of chlorophyll vs. wind stress bins for the shelf at 45.5˚N. The mean shelf chlorophyll concentration for each bin is plotted in the solid green line. The dashed green lines represent the 95% confidence intervals for each bin that is used in further analysis. The 8-day chlorophyll concentration data corresponding to each wind stress bin for this latitude band are plotted in grey. The dashed black line is the global mean shelf chlorophyll concentration (4.34 mg/m^3). If the difference between the high confidence interval and low confidence interval for each bin was greater than the global mean (4.34 mg/m^3), then that bin was ignored in further analysis; these bins are represented by the solid and dashed red lines, representing the mean and 95% confidence intervals for those bins.

3.2.2 *Retention: particle tracking experiments*

To address the role of retention on the shelf, we conducted a particle release experiment in the *Cascadia* model developed by the Washington Coastal Modeling Group (Giddings et al., 2014;

Sutherland et al., 2011) using the Regional Oceanic Modeling System (ROMS; Shchepetkin and McWilliams (2005)). The model domain includes the Salish Sea and coastal ocean of Washington, northern Oregon, and southern British Columbia (Figure 3.6). The horizontal resolution of the model over the slope and shelf is 1.5 km and expands out to a maximum of 4.5 km offshore. The model has 40 *S*-coordinate vertical layers, with stretching parameters set to better resolve the near-bottom and the upper water column. Ocean initial state and forcing on the southern and western boundaries are from the global Navy Coastal Ocean Model (NCOM: Barron et al. (2007, 2006)). Rivers were forced by daily discharge data from the Columbia River, Fraser River, and 14 Puget Sound rivers using data from the USGS and Environment Canada (Giddings et al., 2014). Tides were provided by the quarter-degree TPXO7.2 inverse global tidal model (Egbert & Erofeeva, 2002). All atmospheric forcing was derived from the fifth-generation Mesoscale Model (MM5) from Pennsylvania State University - National Center for Atmospheric Research regional atmospheric forecast model (transitioning to the Weather Research and Forecasting model (WRF) in April 2008) (Mass et al., 2003). A hindcast of physical parameters, including temperature, salinity, and velocity, spanning 2002-2009 was produced using this model setup, with each individual year 2002-2009 run in ROMS initialized from NCOM. Then each year 2003-2009 was re-run initialized from the previous year's ROMS run, thus the year 2002 was discarded as spin-up. Overall, the model's temperature, salinity, and sea surface elevation had high Willmott Skill Scores ($WS \geq 0.92$; Willmott (1982)), based on comparison with data from 2264 CTD casts in 2005 (Giddings et al., 2014). More information about the *Cascadia* model can be found in Davis et al. (2014), Giddings et al. (2014), and Siedlecki et al. (2015), and more information about the particle tracking experiments can be found in Banas et al. (2009a) and Stone et al. (2018) [Chapter 2].

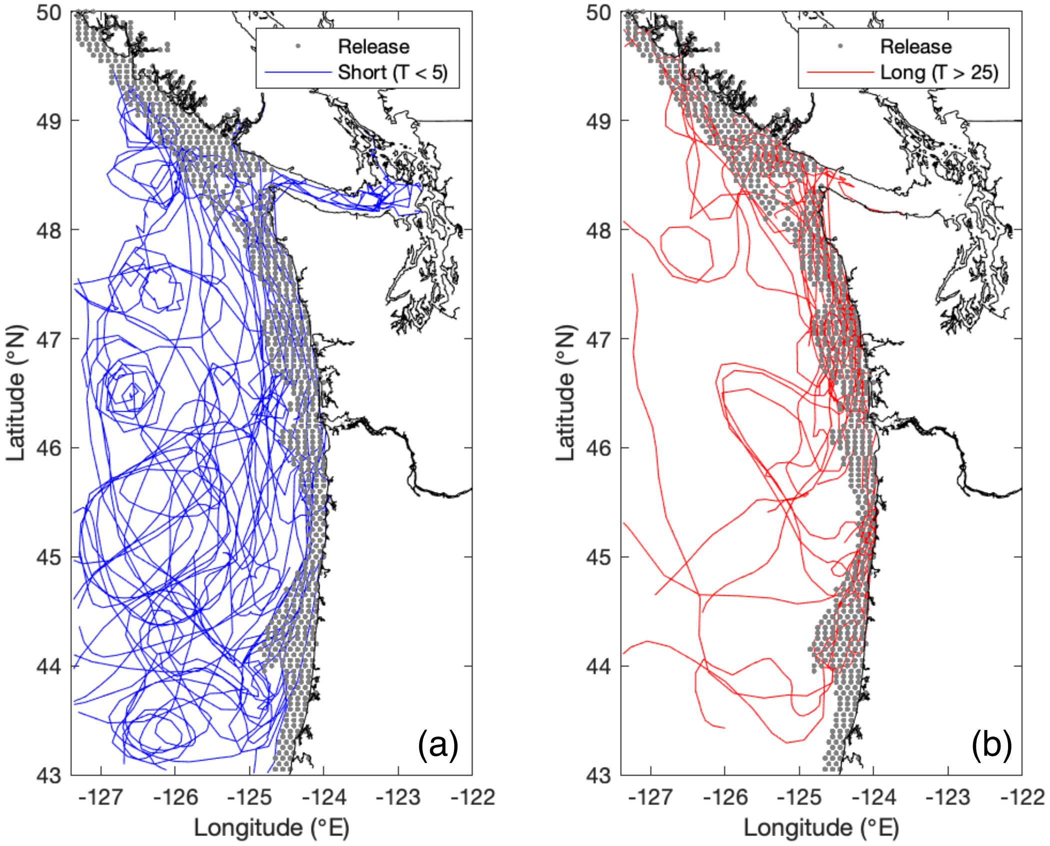

Figure 3.6. Model study domain for the particle tracking experiments. Particle release points are shown in grey. A subsample of particle tracks is also plotted, with short shelf retention times (T < 5 days) plotted in blue (a), and long shelf retention times (T > 25 days) plotted in red (b).

Particles were released in on the shelf (i.e., in water shallower than 150 m, the depth of the shelf break) every 0.05˚ on the model domain, (43˚N – 50˚N) with release points plotted in black in Figure 3.6. They were released every 10 days over 2003 – 2009, resulting in 58,536 particles per year. Once released the surface-trapped particles were tracked with hourly time steps and daily output for up to 350 days, or until they moved outside the model boundaries or ‘‘beached’’ on land, defined as being close enough to land that a bilinear interpolation of the ROMS land mask (1 for ocean, 0 for land) at its location was less than 0.5 (Banas et al., 2015; Stone et al., 2018

[Chapter 2]). Tidally-averaged model output was used for this particle release experiment. Retention times (T) were calculated for each particle based on how long it stayed on the shelf (shallower than 150 m). Examples of short retention times are plotted in blue and long retention times are plotted in red in Figure 3.6. Finally, median retention times were calculated for each latitude band from 44˚N to 49˚N. For a given month and latitude, the monthly mean wind stress and monthly mean chlorophyll concentration, calculated from the same satellite-derived 8-day means used previously, were compared with the median retention time of particles that left the shelf during that month. This analysis was also conducted with particles in a depth-averaged surface layer ranging from 5 to 100 m to the surface, with similar results (not shown).

3.3 RESULTS

3.3.1 *Satellite chlorophyll concentration and wind stress*

As expected in an Eastern Boundary Upwelling System, shelf chlorophyll concentrations were generally highest during negative (upwelling-favorable) meridional wind stress (Figure 3.3). In Figure 3.3, data from the Central CCS, including from 37.5˚N (plotted in orange), makes up the left side of the figure, while data from the Northern CCS, including from 47.5˚N (plotted in blue), makes up the right side of the figure. This pattern shows the strong upwelling-favorable winds that are typical in the Central CCS, as well as the weaker upwelling-favorable winds that are typical in the Northern CCS. However, the same chlorophyll concentration can result from different wind stresses in the Central and Northern CCS, suggesting a varied relationship between chlorophyll concentration and wind stress throughout the CCS. For example, there are numerous observations of chlorophyll concentrations between 15 and 20 mg/m^3 at wind stresses ranging from -0.3 to 0 Pa (Figure 3.3). While these observations are some of the highest chlorophyll concentrations observed over the record, they were measured during a wide range of wind stresses, including some of the strongest and weakest upwelling-favorable winds from the record.

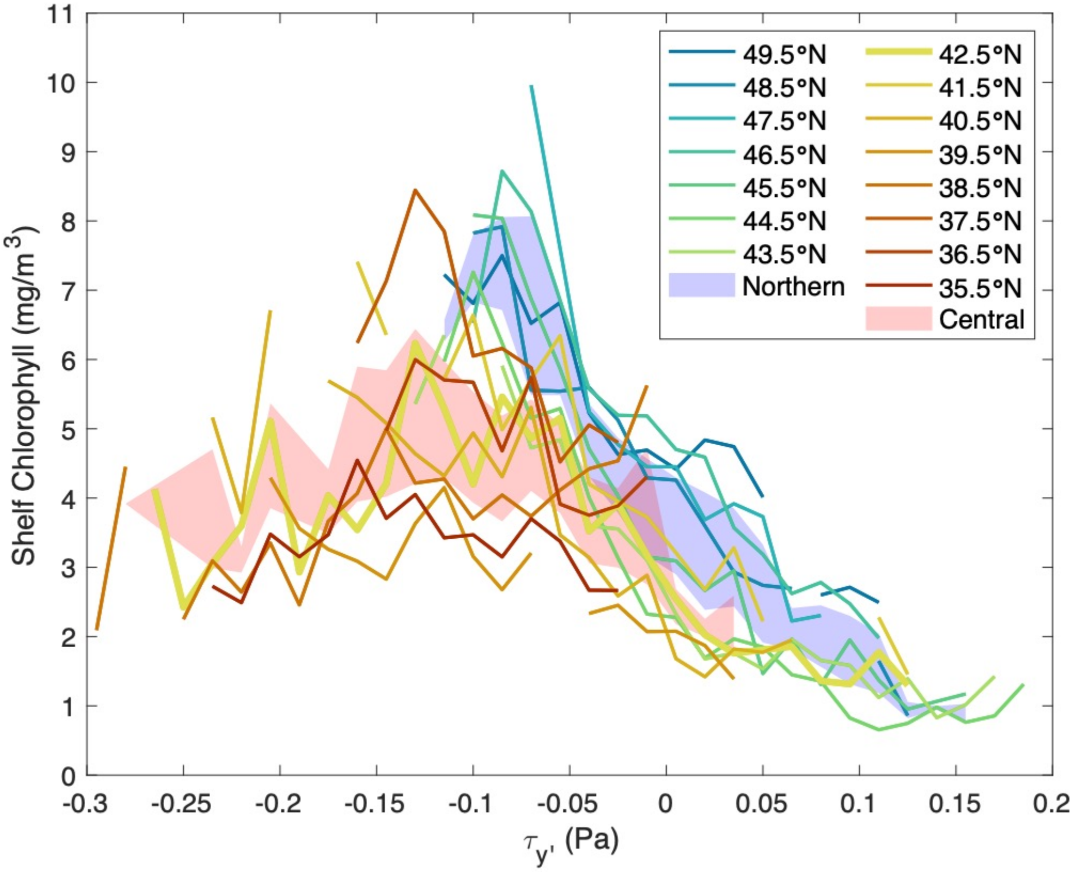

Figure 3.7. Shelf chlorophyll concentration vs. wind stress bins for the entire domain (35.5˚N – 49.5˚N) from 2000 – 2016, colored by latitude. Only bins whose difference between high and low 95% confidence intervals is less than the global shelf chlorophyll mean are included. Northern latitudes (43.5 – 49.5˚N) are shown in cool colors, while Central latitudes (35.5 – 41.5˚N) are shown in warm colors, with the dividing latitude (42.5˚N) is shown in the thick yellow line. Mean chlorophyll concentration vs. wind stresses curves are plotted for the Central region (35.5˚N – 42.5˚N; shaded red) and Northern region (43.5˚N – 49.5˚N; shaded blue). These mean curves were calculated via the bootstrapping method in MATLAB and are plotted to depict the 95% confidence intervals for each region.

Calculating the mean chlorophyll concentration that occurs under a particular wind stress by latitude further suggests that while wind stress is important to chlorophyll concentration throughout the domain, other mechanisms alter how this relationship manifests, particularly in the Northern CCS. For example, in the south, this relationship is roughly flat, particularly at 35.5˚N and 39.5˚N, (dark red and orange, respectively; Figure 3.7). However, as latitude increases, this relationship progresses towards a monotonic relationship, with highest chlorophyll concentrations at the most upwelling-favorable winds, for example 46.5˚N and 47.5˚N (teal and blue, respectively; Figure 3.7). For each latitude, chlorophyll concentration increases with increasing upwelling-favorable wind, while for a given wind stress, chlorophyll concentration increases with latitude, as evidenced at about -0.05 Pa (Figure 3.7).

Individually, results at any single latitude do not support the Botsford et al. (2003) relationship, except perhaps at 42.5˚N (bold yellow line; Figure 3.7) where there is a hint of a dome-shaped relationship between wind stress and chlorophyll concentration. However, over the whole CCS, the relationship between chlorophyll concentration and wind stress has a dome-shaped envelope, consistent with the Botsford et al. (2003) relationship, with individual latitudes contributing different parts of the dome. In the Central CCS (warm colors), the chlorophyll concentrations appear to peak at a wind stress of about -0.125 Pa (Figure 3.7), while in the Northern CCS (cool colors), the chlorophyll concentrations appear to peak at a wind stress of about -0.05 Pa (Figure 3.7). Furthermore, the Central and Northern regions have significantly different relationships between mean chlorophyll concentration and wind stresses. This difference is evident in the separation between the mean curves for the Central and Northern regions, which were calculated via the bootstrapping method in MATLAB and are plotted to depict the 95% confidence intervals for the Central (red shaded curve) and Northern (blue shaded curve) regions (Figure 3.7). While these curves do overlap at a few points near 0 Pa, the rest of points are significantly different.

The difference in chlorophyll concentration-wind stress curves for the Central and Northern regions suggests two dynamically distinct systems north and south of 42.5˚N, which experiences almost the full range of wind stresses. The location of this split is consistent with previous work that found that Cape Blanco (41.9˚N) divided the upwelling system into two regimes: one that is influenced by the Columbia River plume on the shelf north of Cape Blanco and one that is more influenced by strong upwelling-favorable winds south of Cape Blanco (Huyer et al., 2005). The Central CCS appears to be governed by traditional coastal upwelling dynamics characterized by the Botsford et al. (2003) relationship, while in the Northern CCS, the Botsford et al. (2003) relationship manifests differently, with high chlorophyll concentrations observed even during weak upwelling-favorable winds. Furthermore, unlike the Central CCS, the Northern CCS has high chlorophyll concentrations during positive (downwelling-favorable) wind stresses (Figures 3.3, 3.7). Often, particularly for 46.5˚N – 48.5˚N, the mean chlorophyll concentration at positive wind stresses are almost as large as the greatest mean chlorophyll concentrations observed in the Central CCS. However, while phytoplankton in the Northern CCS are productive during downwelling-favorable wind events, this behavior is only observed during the upwelling season. Previous studies have found that phytoplankton will exhibit a large negative productivity anomaly in the event of an anomalously late spring transition like in 2005 (Hickey et al., 2006; Kudela et al., 2006). Still, the overall pattern in the Northern CCS goes against the traditional upwelling-driven phytoplankton productivity that is characteristic of the CCS and suggests another mechanism supporting phytoplankton productivity in the Northern CCS during the upwelling season.

As noted in the Introduction, Hickey and Banas (2008) present two hypotheses for why the Northern CCS is productive at weaker wind stresses: (1) shelf retention related to wind intermittency, freshwater plume dynamics, and shelf geometry, and (2) non-upwelling-derived nutrient sources. Increased retention on the shelf at a given mean wind stress would allow phytoplankton more time to use upwelled nutrients, potentially resulting in higher chlorophyll concentrations at lower wind stresses, particularly on the falling (highly negative wind stress) side of the dome-shaped curve. If this mechanism explained the difference between the Northern and Central CCS in our results, it would manifest itself as either higher retention times at a given moderate wind stress or a more complicated, scattered relationship between retention time and wind stress in the Northern region. Furthermore, to support this hypothesis, this effect of wind intermittency on retention would outweigh the linear relationship between downwelling-favorable winds (positive wind stress) and retention time that represents retention due to Ekman transport onshore driven by downwelling-favorable winds. By conducting particle tracking experiments in a ROMS model, we were able to test this hypothesis.

3.3.2 *Influence of shelf retention*

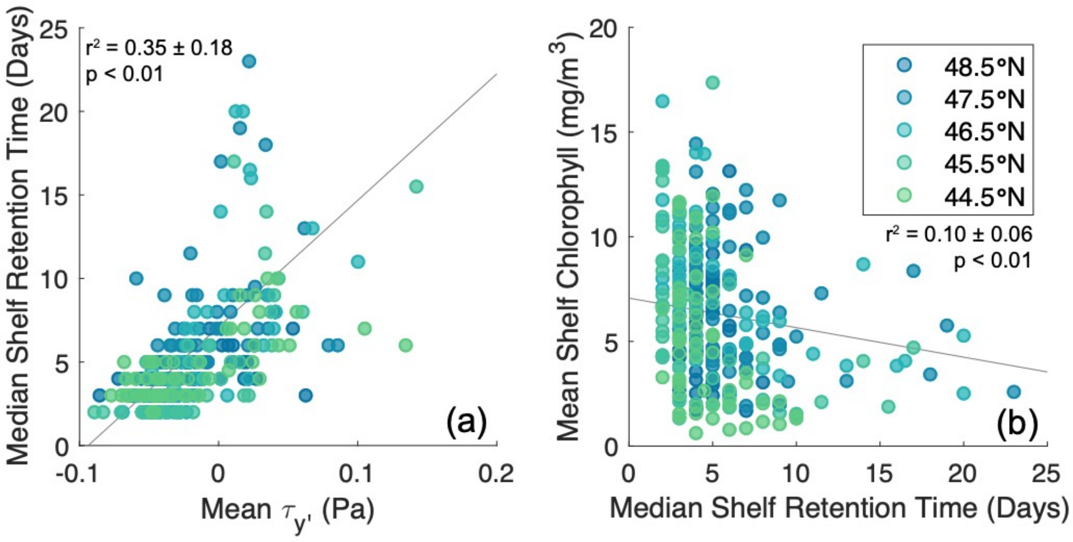

Figure 3.8. Monthly median shelf retention time plotted against mean wind stress (a) and monthly mean shelf chlorophyll concentration plotted against median shelf retention time (b) for 2003 – 2009. Results from 44.5˚N through 48.5˚N are colored by latitude, with more northern latitudes in blues and more southern latitudes in greens. Trendlines for each relationship are plotted in grey ($r^2 = 0.35 \pm 0.11$, $p < 0.01$ (a); $r^2 = 0.10 \pm 0.06$, $p < 0.01$ (b)). There are five instances of retention times > 25 days that are left off this figure in the interest of resolution of the low retention values. In this figure, retention times (T) are calculated from model output while wind stress and chlorophyll concentrations are calculated from the same satellite data used previously.

After calculating retention times from each particle track, monthly median retention times were plotted against monthly mean meridional wind stress. In general, rather than exhibiting either a peak in retention time at moderate wind stress or a scattered relationship between retention time and wind stress that would represent the relationship between high retention time and wind intermittency, in the Northern CCS, retention times increase with positive, downwelling-favorable, wind stress, and there appears to be very little variance in this relationship with latitude ($r^2 = 0.35 \pm 0.11$, $p < 0.01$; Figure 3.8a). Plotting monthly mean chlorophyll concentrations against retention times shows that the highest chlorophyll concentrations are at the lowest retention times ($r^2 = 0.10 \pm 0.06$, $p < 0.01$; Figure 3.8b). The linear relationship between wind stress and retention time suggests that on this scale (1° latitude bins), the effect of wind intermittency on retention time is minimal. Overall, it seems likely that on a large scale, retention is largely driven by the simple mechanism of downwelling-favorable winds inducing Ekman transport onshore, rather than the more nuanced causes of retention such wind intermittency, geography, and mesoscale features as put forth in Hickey and Banas (2008). However, this analysis cannot reject the hypothesis that mesoscale features in the Northern CCS interact with wind intermittency (Banas, MacCready, et al., 2009; Hickey & Banas, 2008) in ways that affect the region's mean productivity (Figure 3.7) more strongly than they affect mean retention time (Figure 3.8). If this were the case, it would not be discernible in retention calculations on this 1° latitude-wide scale.

3.3.3 *Comparison with CUTI and BEUTI*

We also compared the satellite chlorophyll concentration data with the new upwelling indices CUTI and BEUTI from Jacox et al. (2018), both of which are based on estimates from a data-assimilative ROMS reanalysis model of the CCS spanning 1988 to present from 31˚N – 47˚N. CUTI (Coastal Upwelling Transport Index) quantifies the rate of vertical volume transport and includes both Ekman transport and cross-shelf geostrophic flow. BEUTI (Biologically Effective

Upwelling Transport Index) quantifies the *vertical* nitrate flux into the mixed layer, based on CUTI and concentration of nitrate below the mixed layer. Thus, as defined, BEUTI does not include lateral nutrient fluxes into the mixed layer. If the higher productivity of the Northern CCS is due to higher nutrient concentrations below the mixed layer such that a weaker wind stress would still result in a high concentration of nutrients upwelled, then we would expect a plot of chlorophyll concentration against BEUTI to collapse the two peaks into one peak. More information about these indices can be found in Jacox et al. (2018) and at http://mjacox.com/upwelling-indices/.

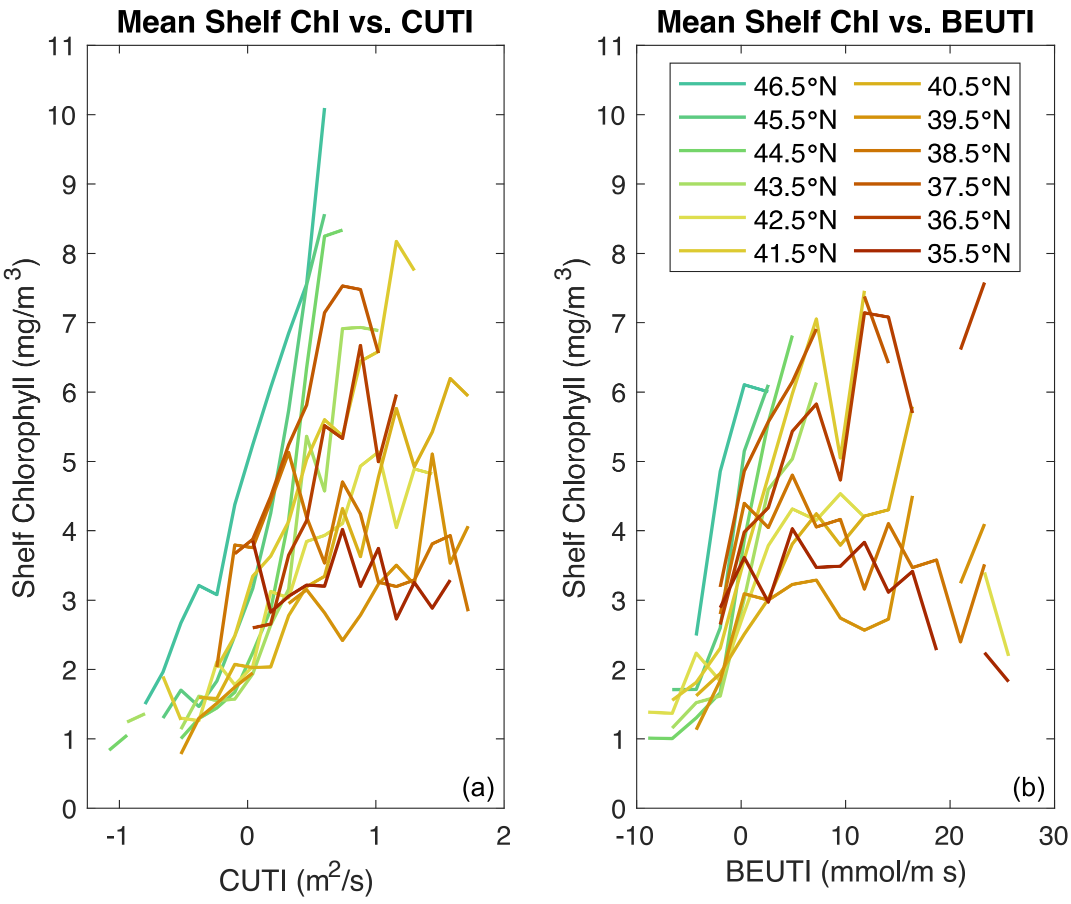

Figure 3.9. Mean shelf chlorophyll concentration plotted against CUTI (a) and BEUTI (b), colored by latitude. Similar to the shelf chlorophyll concentration vs. wind stress plots, in these plots, shelf chlorophyll was binned by its corresponding CUTI and BEUTI values, and the mean value and 95% confidence intervals for each bin is calculated. For CUTI, each bin represents 0.14 m^2/s and for BEUTI, each bin represents 2.3 mmol/s. Bins with a difference between their high and low confidence intervals greater than the CCS-wide mean were ignored.

As expected, shelf chlorophyll concentration increases with increasing CUTI, with the Central CCS experiencing the highest values for CUTI and the Northern CCS experiencing the lowest values (Figure 3.9a). Similar to the patterns in Figure 3.7, the relationship between shelf chlorophyll concentration and CUTI suggests variation with latitude, as in the Northern CCS, some of the highest chlorophyll concentrations correspond to the lowest CUTI values over the whole

CCS. Overall, the use of CUTI does not help explain the difference between the Central and Northern CCS by collapsing the two peaks in chlorophyll concentration for the different regions into one peak, likely because CUTI represents wind-driven vertical transport into the mixed layer.

Similarly, the Central CCS experiences the highest BEUTI values, while the Northern CCS experiences the lowest values, once again crossing into negative BEUTI values (Figure 3.9b). There appears to be some separation between the Northern CCS and Central CCS in the shelf chlorophyll plotted against BEUTI. This separation suggests that it is not a higher subsurface nutrient concentration that accounts for the higher chlorophyll concentrations in the Northern CCS. These results suggest that is more likely that the BEUTI index does not capture the different nutrient dynamics in the Northern CCS, such as the lateral nutrient flux via outflow from the Salish Sea (Davis et al., 2014), in the sense that if BEUTI captured those mechanisms, the Northern and Central relationships would collapse together.

3.4 DISCUSSION

While the overall relationship between shelf chlorophyll concentration and wind stress is dome-shaped for the entire Central and Northern CCS, as suggested by Botsford et al. (2003) and supported by Yokomizo et al. (2010), Jacox et al. (2016), and Ruzicka et al. (2016), this is not the case for individual latitudes within the CCS, likely because each individual latitude band does not experience enough wind variation, or because strong winds occur so rarely during the satellite era that we cannot resolve them statistically (Figure 3.5). In particular, in the Northern CCS, the relationship between shelf chlorophyll concentration and wind stress is most simply described as monotonic, with the highest chlorophyll observations occurring with the most upwelling-favorable (negative) wind stress values. However, the Northern CCS does not typically experience the most extreme upwelling-favorable wind stress observed in the CCS. If stronger upwelling-favorable winds became common and statistically resolvable in the Northern region, would chlorophyll concentrations decrease, as suggested by Botsford et al. (2003), or would they continue to increase? This uncertainty presented by lack of forcing variability extends into the Central CCS as well, where there are few observations of the most extreme winds. Of those observations, the phytoplankton response varied widely, evident in Figure 3.3a where wind stresses beyond -0.25 Pa elicited chlorophyll concentrations ranging from about 2 to 22 mg/m^3. However, due to the statistical limits accompanying few observations, we cannot say anything meaningful about these extreme winds. The results presented in Figure 3.7 represent about 87% of all observations for the Central and Northern CCS and these results support the application of Botsford et al. (2003)'s dome-shaped relationship for the CCS as a whole.

While the simple dome-shaped relationship does appear to apply to the CCS as a whole, there are some limits to this interpretation of the wind-productivity relationship. Botsford et al. (2003) only considers a simple, two-dimensional upwelling system, but does not consider regional differences, such as the role of filaments in the Central CCS and the role of freshwater input and non-upwelling-derived nutrients sources in the Northern CCS. This two-dimensional upwelling system includes cross-shelf transport but does not include any downstream transport, which is particularly relevant in the presence of filaments. The semi-permanent filaments of the Central CCS form at capes and other promontories and act as a rapid conduit of phytoplankton to the open ocean, particularly at Pt. Arena (38.9˚N) and Cape Mendocino (40.4˚N) (Strub et al., 1991). The rapid transport of chlorophyll offshore by these filaments could explain the flatness of the 38.5˚N and 40.5˚N lines in Figure 3.7 that depict their relationship between wind stress and chlorophyll concentration. Inclusion of both cross-shelf and downstream transport in the Botsford et al. (2003)

model might better capture the relationship between chlorophyll concentration and wind stress in this upwelling system, and is an important direction for future work.

If chlorophyll concentration decreases on the shelf under extreme wind conditions because of cross-shelf advection, one might expect significant chlorophyll concentrations observed in the offshore region under strong upwelling. Previous studies suggest that beyond the shelf break, phytoplankton are less productive due to both limited light and nutrient availability. Huntsman and Barber (1977) found that phytoplankton become light-limited during periods of deep mixing, reducing the overall productivity of the region during a mixing event lasting just days. Additionally, subduction and advection of nutrients and phytoplankton from the coast to the open ocean via mesoscale eddy activity (Gruber et al., 2011; Rossi et al., 2008, 2009) and by the California Current jet (Barth et al., 2002) reduces productivity near the coast. However, a model study by Lathuilière et al. (2010) found that while overall productivity of the shelf region decreases due to transport of nutrients and phytoplankton offshore, mesoscale eddy activity widens the coastal productivity band from about 80 km to 200 km, suggesting that phytoplankton can still be productive in the offshore region. Additionally, Jacox et al. (2016) found that the offshore region was still productive, though less so than the shelf region because chlorophyll concentration in the offshore region is about 12-25% of that of the shelf region, but this productivity was not significantly correlated with wind stress. Our initial analysis examined chlorophyll concentration in the offshore region (between the 150 m and 2500 m isobaths) using a similar procedure as we used for the shelf region. Similar to Jacox et al. (2016), based on plots from all latitudes spanning 35-50˚N, the chlorophyll concentrations in the offshore region were about 25% of those of the shelf region and remain roughly constant with varying wind stress (not shown).

However, it may not be the case that phytoplankton productivity in this offshore region is a minor contribution, as these studies suggest. Other studies have found that in the offshore region, a subsurface chlorophyll maximum may develop due to subduction of phytoplankton offshore (Barth et al., 2002; Bograd & Mantyla, 2005; Huyer et al., 2005; Kadko et al., 1991), and this feature likely is not captured by satellite in the offshore region. Furthermore, there is also evidence that in the offshore region, phytoplankton shift to a smaller cell size due to iron limitation and these smaller phytoplankton are more tightly coupled with grazers (Rykaczewski & Checkley, 2008). If future work is able to incorporate more observations of phytoplankton under extreme upwelling-favorable wind conditions, it would be useful to examine the offshore region as well to see if there is a transfer to phytoplankton offshore from the shelf, or if once phytoplankton leave the shelf, they are largely lost to the depths.

Lastly, results from the particle release experiment found that on a large, 1° latitude-wide scale, the effect of wind intermittency on retention is minimal because the relationship between retention time and wind stress is linear. However, this result does not disqualify the influence of more complex controls on retention like wind intermittency on smaller spatial scales. The interactions between intermittent winds, mesoscale bathymetry (e.g., Heceta Bank), and freshwater dynamics (e.g., the Columbia River plume) could easily lead to a situation in which mesoscale, transient retention features had a greater effect on large-scale mean chlorophyll concentrations than on large-scale mean shelf retention times. Pursuing these possibilities likely requires a Lagrangian analysis of nutrient and biomass budgets, presumably in models, rather than an Eulerian, observational analysis.

The same small-scale features might well have equally nonlinear effects on large-scale mean nutrient supply. The Columbia River plume entrains ocean-derived nutrients though mixing between ocean water and river water at the river plume lift-off region and then moves these nutrients seaward at the surface (Banas et al., 2009b; Hickey & Banas, 2008; MacCready et al., 2009). Similarly, nutrient-rich water that is upwelled into the Strait of Juan de Fuca is entrained into the surface outflow, spreading nutrients along the shelf locally (Davis et al., 2014; Hickey & Banas, 2008; MacFadyen et al., 2008). Additionally, irreversible turbulent mixing throughout the region transports nitrate from near-bottom water to surface water at a rate of about 25% of nutrient transport by upwelling (Hales et al., 2005). Therefore, in addition to retaining phytoplankton in surface shelf water, the mechanisms within these "retentive regions" may be providing more nutrients to the shelf via entrainment of ocean-derived nutrients into the surface layer.

3.5 CONCLUSIONS

Using chlorophyll concentration and wind stress derived from satellite observations, we studied the relationship between chlorophyll concentration and wind stress in the California Current System, spanning 35˚N to 50˚N, and 2000 – 2016. Additionally, to address the influence of shelf retention on this relationship, we conducted particle tracking experiments in a ROMS model of the Northern CCS (43˚N – 50˚N) for 2003 – 2009. The main conclusions for this analysis are:

1. *The relationship between chlorophyll concentration and wind stress in the California Current System is dome-shaped.*

   Does the Botsford et al. (2003) relationship apply to the Central and Northern California Current System? Yes, but only as a whole. At individual latitudes, only pieces of the dome-shaped relationship between chlorophyll concentration and wind stress are visible (Figure 3.7). In general, at a given latitude, chlorophyll concentration increases with upwelling-favorable wind stress, with a downturn in chlorophyll concentration at high upwelling-favorable wind stresses in the Central CCS. At a given wind stress, chlorophyll concentration increases with latitude with the Northern CCS having the highest chlorophyll concentrations. Additionally, in the Northern CCS, chlorophyll concentrations were still relatively high during downwelling-favorable winds.

2. *High chlorophyll concentration is observed in the Northern CCS during weak upwelling-favorable and downwelling-favorable winds.*

   Despite the weaker upwelling-favorable winds, as well as downwelling-favorable winds experienced during the upwelling season, high chlorophyll concentrations are observed in the Northern CCS (Figure 3.7). In fact, over the entire CCS, some of the highest chlorophyll concentrations are observed in the Northern CCS, despite the weaker winds, as Ware and Thomson (2005) originally noted, using a much shorter satellite record.

3. *There are two separate curves that describe the relationship between chlorophyll concentration and wind stress in the CCS.*

   The Central CCS and Northern CCS have significantly different relationships between mean chlorophyll concentration and wind stresses, which is evident in the separation between the mean curves for the Central (red shaded curve) and Northern (blue shaded curve) regions (Figure 3.7). These results suggest that the Central CCS is governed by traditional upwelling dynamics, while the high chlorophyll concentrations during weak upwelling-favorable and downwelling-favorable winds in Northern CCS suggests another mechanism supporting phytoplankton productivity during the upwelling season. Hickey and Banas (2008) present two hypotheses for the Northern CCS's high biomass: complex retention on the shelf and additional non-upwelling-derived nutrient sources. Their second hypothesis is further supported by Davis et al. (2014), who found in a model study that the nutrient-rich outflow from the Strait of Juan de Fuca fueled productivity in this region. While results from the particle tracking experiment compared with chlorophyll concentrations and wind stress in the Northern CCS found that the effect of wind intermittency on retention is minimal on a 1˚latitude-wide scale (Figure 3.8), they do not disqualify the influence of more complex controls on retention like wind intermittency on smaller spatial scales.

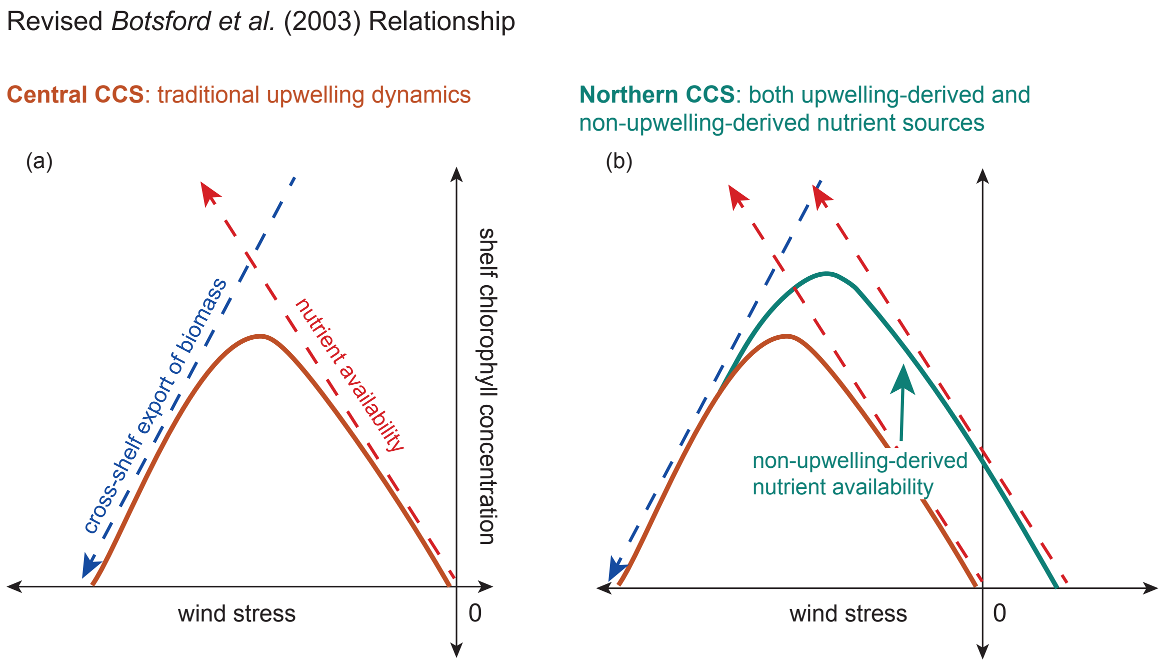

Figure 3.10. A revised Botsford et al. (2003) relationship for the Central and Northern CCS. The relationship between shelf chlorophyll concentration and wind stress in the Central CCS (orange curve, a) and in the Northern CCS (teal curve, b). The chlorophyll response to nutrient availability supplied by upwelling-favorable wind stress is depicted by the red dashed arrow, while the chlorophyll response to cross-shelf export of biomass is depicted by the blue dashed arrow. Non-upwelling-derived nutrient availability (teal arrow in b) in the Northern CCS accounts for the increase in overall nutrient availability and shift of the shelf chlorophyll response to wind stress (teal curve) into downwelling-favorable wind stresses (b).

Based on these results, we propose a revised Botsford et al. (2003) relationship for the CCS (Figure 3.10). The Central CCS is governed by traditional upwelling dynamics and its relationship between shelf chlorophyll concentration and wind stress (orange curve; Figure 3.10a) represents the balance between nutrient availability (red dashed arrow; Figure 3.10a) and cross-shelf export of biomass (blue dashed arrow; Figure 3.10a). The Northern CCS still follows the overall pattern of traditional upwelling dynamics, with its relationship between shelf chlorophyll concentration and wind stress (teal curve; Figure 3.10b) still representing this balance, but its nutrient availability is increased by non-upwelling-derived nutrients (teal arrow; Figure 3.10b). Non-upwelling-derived nutrient sources include lateral nutrient fluxes through mechanisms like outflow from the Salish Sea which Hickey and Banas (2008) estimated as 0.6 x 10^9 kg of nitrate per upwelling season and which Davis et al. (2014) suggests account for 20% of primary productivity in the Northern CCS, with contributions varying with distance from the Strait of Juan de Fuca. Outflow from the Columbia River also contributes to non-upwelling-derived nutrients (0.04 x 10^9 kg of nitrate per upwelling season: Hickey and Banas (2008)), though its effects are much more localized and are on a smaller scale (Davis et al., 2014). This increase in nutrient availability in the Northern CCS effectively shifts the chlorophyll-wind relationship towards downwelling-favorable wind stresses, resulting in the high productivity at weak upwelling-favorable and downwelling-favorable winds that is characteristic of the Northern CCS. While the data from the Northern CCS do show that chlorophyll concentration is higher on the falling side of the curve in downwelling-favorable wind stresses, the shape of the curve on the high chlorophyll side in upwelling-favorable wind stresses is unclear (Figure 3.7). Therefore, the data are consistent with this revised Botsford et al. (2003) relationship for the CCS, but they are not sufficient to fully test this new hypothesis.

Future work should focus on understanding the role of mesoscale retention driven by geographic features and wind intermittency, as well as the role of lateral nutrient fluxes in the Northern CCS, such as outflow from the Strait of Juan de Fuca and river discharge. Incorporation of these non-upwelling-derived nutrient sources into indices like CUTI and BEUTI could help collapse the observations into Botsford et al. (2003)'s hypothesized dome-shaped relationship as expected. Furthermore, a better understanding of the nutrient-chlorophyll dynamics in the Northern CCS may allow us to better predict how productive this region may be under different future conditions.

3.6 ACKNOWLEDGEMENTS

Special thanks to the MacCready and Banas lab groups for useful conversations, to Melanie Fewings for help with satellite wind products, to Mike Jacox for use of the CUTI and BEUTI indices, to Kym Jacobson and Jennifer Fisher at NOAA Northwest Fisheries Science Center for providing the Newport Hydrographic Line data, to Evelyn Lessard for guidance, and to David Darr for computer cluster administration and support. This chapter is co-authored by Neil S. Banas, Parker MacCready, Raphael M. Kudela, and Bridget Ovall. Publicly available datasets were analyzed in this study. Satellite chlorophyll concentration data is available through the GlobColour Project (http://hermes.acri.fr/); wind stress derived from QuikSCAT and ASCAT wind speeds is available through NOAA CoastWatch Program and Remote Sensing Systems, Inc. (https://coastwatch.noaa.gov/cw/index.html); and CUTI and BEUTI from Jacox et al. (2018) are found at http://mjacox.com/upwelling-indices/. Access to model run setup files and derived output used for the particle tracking experiments in this paper are available upon request, without undue reservation, as described here: iodlabs.ucsd.edu/sgiddings/PNWTOX/contact.html. These model setup files and output data are curated by MacCready on MacCready's server at UW and will remain curated for at least 5 years. H. Stone was supported by a National Science Foundation (NSF) Graduate Research Fellowship. P. MacCready, N. Banas, and H. Stone were supported by MERHAB grant number NA16NOS4780189 from the Coastal Ocean Program of the National Oceanic and Atmospheric Administration (NOAA). R. Kudela was supported by the RISE funds from NSF, grant number OCE 0238347. B. Ovall was supported by NOAA grant number NA16NOS0120019. This is a contribution of the MERHAB program. The findings and conclusions are those of the authors and do not necessarily reflect those of NSF, NOAA, or the Department of Commerce.

Chapter 4. MODELING TRANSPORT OF HARMFUL ALGAL BLOOMS TO PACIFIC NORTHWEST COASTAL BEACHES

4.1 INTRODUCTION

Globally, the impacts of harmful algal blooms (HABs) on public health, fisheries, aquaculture, and ecosystem have increased over the past few decades (D. M. Anderson et al., 2012). In the Pacific Northwest, a prominent type of HAB found are species in the genus *Pseudo-nitzschia* (*PN*). *PN,* a type of diatom, produce domoic acid (DA), a neurotoxin that causes amnesic shellfish poisoning. DA is easily transferred up the food chain and can have severe or fatal effects on seabirds, marine mammals, and humans (Lefebvre et al., 2002). Given the dangerous health impacts, once DA is found on beaches where either commercial or recreational fishing occurs, these beaches are closed to activities such as shellfish harvest or fishing. However, these closures can significantly and negatively affect people whose livelihoods rely on these fisheries, including people within the commercial fishing industry itself and people within the tourism industry (Ritzman et al., 2018). Historical data of *PN* and DA on beaches suggests that there are bands of years with numerous beaching events, and bands of years with very few (e.g., McCabe et al. (2016); McKibben et al. (2017)). Ocean-atmosphere climate variability could explain the gaps in HAB events, with warm anomalies associated with the Pacific Decadal Oscillation (PDO) and El Niño-Southern Oscillation (ENSO) triggering *PN* events (McCabe et al., 2016; McKibben et al., 2017).

In the Pacific Northwest, the sources of *PN* cells to the coastal region are the Juan de Fuca eddy in the summer and early fall (MacFadyen et al., 2005; Trainer et al., 2002, 2009) and Heceta Bank in the winter and early spring (Hickey et al., 2013), both of which are retentive regions with appropriate supply of nutrients during some or all of the year. For *PN* cells to reach the coast from either of these retentive regions, enough *PN* cells must first accumulate for a bloom to form. Then, this bloom must escape its “hot spot” and travel to the coast, all of which require particular wind conditions. In the Juan de Fuca eddy, *PN* cells must first accumulate in the eddy under downwelling-favorable winds. Next, *PN* cells escape the eddy under upwelling-favorable winds. Finally, downwelling-favorable winds transport *PN* cells to the coast. These dynamics can be further complicated by the Columbia River plume, which can act as both a conduit and as a barrier for *PN* cells to the coasts (Giddings et al., 2014; Hickey et al., 2013). During wind reversals in the summer or fall, the northern branch of the Columbia River plume is pushed against the coast, acting as a barrier for *PN* cells for part of the WA coast. However, during strong storms in the winter, the Columbia River plume helps transport *PN* cells up even farther north along the coast.

While many HAB events follow this pattern, there are some important nuances that add a layer of complexity to forecasting. Within the eddy itself, *PN* cells do not typically dominate the bloom. They are often found in blooms of other types of diatoms, as well as with euglenoids and dinoflagellates, usually making up no more than 17% of biomass within the eddy (Trainer et al., 2009). Therefore, not every cell, or even most of the cells, that are transported to coastal beaches are *PN* cells. Additionally, the concentration of *PN* cells does not correlate with concentration of DA, and presence of *PN* cells does not indicate presence of DA (Trainer et al., 2009). Lastly, *PN* cells do not always originate in a known “hot spot” like the Juan de Fuca eddy. In six cruises that sampled the Juan de Fuca eddy and nearshore region spanning 2003 – 2006, *PN* cells were observed both in the nearshore region and within the eddy, with some difference in *PN* species between regions, suggesting that these populations were unrelated (Trainer et al., 2009). Similarly, recent sampling of the eddy from cruises spanning 2017 – 2019 found that among ten cruises, there was one cruise that did not observe any *PN* cells within the eddy, despite observations of *PN* cells at several nearby beaches. Additionally, analysis of the coast-wide HAB event in 2015 suggested these *PN* cells came from a diffuse offshore source rather than one of the usual “hot spots” like the Juan de Fuca eddy or Heceta Bank (McCabe et al., 2016).

Given the huge losses that can result from fishery closures in the region, understanding when and where a HAB event will occur can help minimize the collateral economic damage that accompanies last-minute changes of plans due to an unexpected HAB event, such as suddenly having to close a beach right before a big razor clamming weekend, as well potentially avoid unnecessary closures. The Pacific Northwest’s HAB Bulletin program, a partnership between academic, government, and tribal stakeholders, uses a combination of monitoring programs and modeling to better understand the formation, evolution, and transport of HABs in this region. In addition, this program produces periodic bulletins to inform local stakeholders of current and forecasted conditions. These bulletins make HAB risk recommendations based on expert synthesis of observations including in situ sampling, wind and surface current patterns, satellite chlorophyll concentrations, and river discharge, as well as relevant Pacific Ocean indices, marine weather forecasts, and modeled particle transport forecasts. Currently, the PNW HAB Bulletin also uses 72-hour model forecasts of *PN* transport from the Juan de Fuca Eddy and Heceta Bank in its preparation. One goal of this study is to analyze particle tracks combined with a variety of beaching criteria to improve the forecasting capabilities of the model. With improved forecasting, it is possible that in the future we could be able to forecast HAB events with enough notice for earlier harvests, which could be extremely beneficial to both the economy and to those whose livelihoods rely on the commercial or recreational fishing industries.

In this study, we use in situ beaching data and wind stress observations combined with particle tracking experiments to test whether the model reproduces the observed patterns of *PN* cell beaching that originate in the Juan de Fuca eddy. As part of this analysis, we also test various beaching criteria to identify which criterion best matches observations and therefore is most appropriate to use in the forecasting model. Lastly, we compare results from an older medium-resolution version of the model with the newer high-resolution version of the model, which is currently used for forecasting for the PNW HAB Bulletin.

4.2 METHODS

4.2.1 *Beach observations and wind stress*

In this study, we used beach observations of *PN* cell counts from 46 beaches (shown as blue stars in Figure 4.1) in Washington and Oregon spanning 2000 – 2018. Samples were collected at each beach in water depths of 1-, 5-, and 10-m, and the total number of *PN* cells were counted in these whole water samples (Trainer et al., 2009). In Washington, beach observations are conducted by the Olympic Region Harmful Algal Bloom (ORHAB) partnership (http://depts.washington.edu/orhab/), while in Oregon, past beach observations were conducted as part of the Monitoring Oregon Coastal Harmful Algae (MOCHA) project and continue today supported by the Monitoring and Event Response for Harmful Algal Blooms (MERHAB) program. The MERHAB program also includes partners in the Washington Department of Fish and Wildlife, Washington State Department of Health, and Oregon Department of Fish and Wildlife. In this paper, we will focus on observations north of the Columbia River mouth, where beach sampling was most consistent, and the summer-autumn upwelling period. To identify events in observations that match the proposed mechanism of *PN* cells escaping the Juan de Fuca eddy and then being transported to the beach, we used wind stress derived from satellite wind speeds. The daily mean wind stress values were derived from QuikSCAT and ASCAT satellite wind velocities from 1° longitude offshore following Smith (1988) (NOAA CoastWatch Program and Remote Sensing Systems, Inc.). Data span August 1999 – November 2009 (QuikSCAT) and October 2009 – Present (ASCAT) at a resolution of 25 km. The mean of the wind stress data was taken over 1° latitudinal bands and then plotted against the beach observations data to identify events. For this study, we focused on the 2000 – 2018 time period, transitioning from QuikSCAT to ASCAT at November 1, 2009.

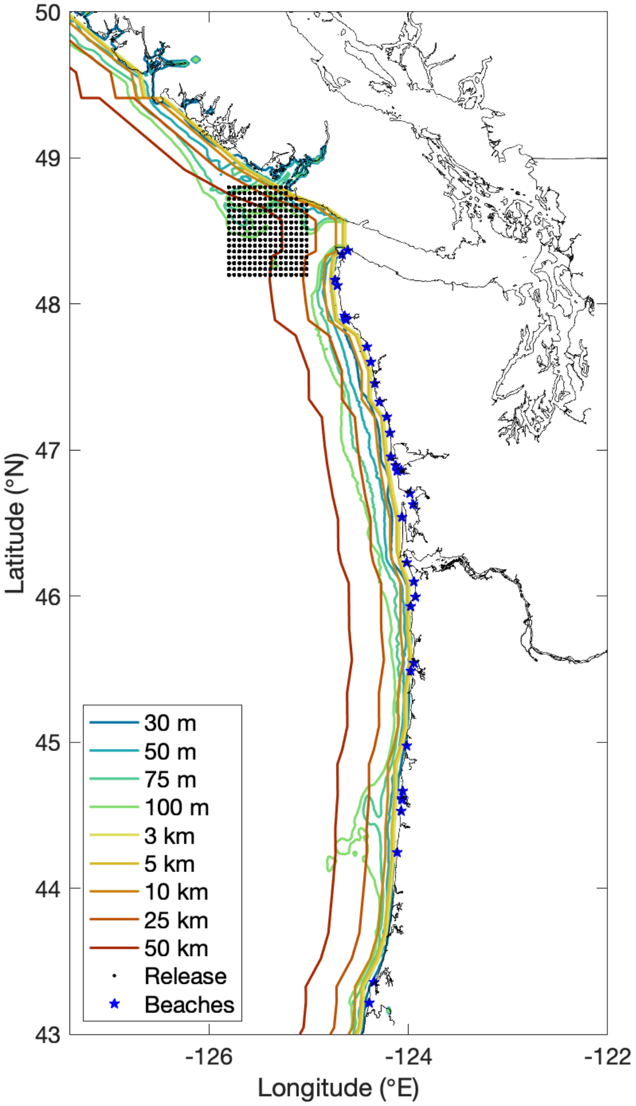

Figure 4.1. Map of study location. Beach locations for sampling are plotted in blue stars, release points for particle tracking experiments are plotted in black dots, and beaching criteria are plotted in colored lines. Beaching criteria based on isobath are plotted in cooler colors and beaching criteria based on distance offshore are plotted in warmer colors.

4.2.2 *Particle tracking experiments*

To test whether the model captures the proposed mechanism of transport from the Juan de Fuca eddy, as well as asses the skill of the PNW Bulletin forecasting system, we conducted a particle release experiment in three different versions of the model, two of which use the medium-resolution grid of the *Cascadia* model, with output spanning 2003 – 2009 (PNWTOX series) and 2013 – 2018 (LiveOcean series). The third version, part of the LiveOcean series, uses a higher resolution grid and is described in the following paragraph. These model versions were developed by the University of Washington Coastal Modeling Group (Giddings et al., 2014; Sutherland et al., 2011) using the Regional Oceanic Modeling System (ROMS; Shchepetkin and McWilliams (2005)). The model domain includes the Salish Sea and coastal ocean of Washington, Oregon, and southern British Columbia, spanning 43˚N – 50˚N, -127.4˚E – 122˚E (Figure 4.1). The horizontal resolution of the model over the slope and shelf is 1.5 km and expands out to a maximum of 4.5 km offshore. The model has 40 *S*-coordinate vertical layers, with stretching parameters set to better resolve the near-bottom and the upper water column. Ocean initial state and forcing on the southern and western boundaries are from the global Navy Coastal Ocean Model (NCOM: Barron et al. (2007, 2006)). Rivers were forced by daily discharge data from the Columbia River, Fraser River, and 14 Puget Sound rivers using data from the USGS and Environment Canada (Giddings et al., 2014). Tides were provided by the quarter-degree TPXO7.2 inverse global tidal model (Egbert & Erofeeva, 2002). All atmospheric forcing was derived from a regional implementation of the fifth-generation Mesoscale Model (MM5) from Pennsylvania State University - National Center for Atmospheric Research regional atmospheric forecast model (transitioning to the Weather Research and Forecasting model (WRF) in April 2008) (Mass et al., 2003). A hindcast of physical parameters, including temperature, salinity, and velocity, spanning 2002 – 2009 was produced using this model setup, with each individual year 2002 – 2009 run in ROMS initialized from NCOM. Then each year 2003 – 2009 was re-run initialized from the previous year's ROMS run, thus the year 2002 was discarded as spin-up. More information about the *Cascadia* model, including model performance, can be found in Davis et al. (2014), Giddings et al. (2014), and Siedlecki et al. (2015), and more information about the particle tracking experiments can be found in Banas et al. (2009) and Stone et al. (2018) [Chapter 2]. For the period 2013 – 2018 a similar version of the model was run as part of the LiveOcean series. It used the same "medium-resolution" grid as the 2003 – 2009 run, and only differed in using the Navy HYCOM model (Metzger et al., 2014) for its open ocean boundary conditions.

In addition to using the medium-resolution version of the LiveOcean model, we also ran experiments in the newer, high-resolution version of the LiveOcean model, spanning 2017 – Present. The purpose of this experiment was to compare performance of the medium-resolution version against the high-resolution version because the latter is currently used for forecasting in the PNW HAB Bulletin. Similar to the medium-resolution version, the high-resolution version includes the Salish Sea and the coastal waters of Washington, Oregon, and Vancouver Island, B.C., spanning 42˚N – 52˚N, -130˚E – 122˚E, though its resolution is much higher, with 500 m resolution within the Salish Sea and Washington coastal estuaries, stretching to 3 km resolution offshore. Additionally, there are 30 *S*-coordinate vertical layers, with stretching parameters set to better resolve the near-bottom and the upper water column. Other differences in the medium-resolution version and high-resolution version include the addition of more coastal rivers, with output from 45 rivers total, and use of higher resolution open-ocean boundary model forcing from HYCOM, a global, data-assimilative ocean model with a resolution of 4.5 km in this region (Metzger et al., 2014). In addition, the high-resolution version of the model uses a WRF model with finer resolution (1.4 km instead of 12.5 km) for its atmospheric forcing. Further details about the high-resolution version of the LiveOcean model can be found in MacCready et al. (In Prep).

Particles were released at the surface within the typical extent of the Juan de Fuca eddy (48.2 – 48.8˚N; -125.8˚ – -125˚E) with release points every 0.052˚ in longitude and 0.04˚ in latitude, plotted in black in Figure 4.1. They were released every 2 days from the Spring transition to the Fall transition over 2004 – 2007 and 2013 – 2017, resulting in approximately 22,277 particles per year, though the number depends on the dates of the Spring and Fall transitions, based on the Pierce and Barth method (Barth et al., 2007; Pierce et al., 2006). We chose to release particles from the Juan de Fuca eddy only between the spring and fall transition dates because the Juan de Fuca eddy is a seasonal feature that is typically present during the upwelling season (Denman & Freeland, 1985; Freeland & Denman, 1982; Freeland & McIntosh, 1989; MacFadyen et al., 2005; MacFadyen & Hickey, 2010). Once released the surface-trapped particles were tracked with hourly time steps and daily output for up to 30 days, or until they moved outside the model boundaries or ‘‘grounded’’ on land, defined as being close enough to land that a bilinear interpolation of the ROMS land mask (1 for ocean, 0 for land) at its location was less than 0.5 (Banas et al., 2015; Stone et al., 2018 [Chapter 2]). Tidally-averaged model output was used for this particle release experiment.

4.2.3 *Skill assessment*

With the particle tracks, we tested a variety of beaching criteria within the model to see which criteria best captures the observed beaching of *PN* cells that originate in the Juan de Fuca eddy. The dynamics of the inner shelf, including cross-shelf transport, are not well-resolved in the model, so we assume that any time a particle gets within a certain distance or passes a certain isobath, that it is also likely to be present on the beach in reality, even if the paths of these particles suggest that they just move along the coast. In addition, we also tested whether a particle should be removed from tracking after its first beaching (first beaching) or if a particle should be allowed to beach multiple times along its path (any beaching), based on the beaching criteria. The beaching criteria tested were based on whether a particle crosses a particular isobath and whether a particle is within a certain distance of the coast. For isobath-based beaching, the criteria tested were 30 m isobath, 50 m isobath, 75 m isobath, and 100 m isobath, and for beaching based on distance offshore, the criteria tested were 3 km offshore, 5 km offshore, 10 km offshore, 25 km offshore, and 50 km offshore. All of these criteria were tested following the first beaching and any beaching of each particle, totaling 18 tested criteria. These beaching criteria are plotted in Figure 4.1, with those based on isobath plotted in cooler colors and those based on distance offshore plotted in warmer colors. In this paper, output from June 1 through the Fall transition for 2004 – 2007 and 2013 – 2017 and beaches above the Columbia River mouth (46˚N – 48˚N) were used to test these criteria, as most of the observations of *PN* cells from the Juan de Fuca eddy occur during the late summer in this region (Giddings et al., 2014; MacFadyen et al., 2005; Trainer et al., 2002, 2009).

To address the performance of each of these criteria, locations and timings of beached particles were compared with observed *PN* cell counts at Washington beaches. Again, as discussed in the Introduction, it is important to note that in this study, particles are only originating in the Juan de Fuca eddy and therefore are unlikely to capture the transport pathways of *PN* cells from regions outside the eddy. Similarly, even when they are present, *PN* cells do not dominate the biomass within the eddy so in reality, not all phytoplankton cells that beach are *PN* cells (Trainer et al., 2009). From there, daily particles results for each 0.125˚ of coastline were compared with cell counts (measured within one day before or after the particle results), and were then categorized as “true positive” (at least one particle beached and at least 10,000 *PN* cells/L were measured), “true negative” (no particles beached and less than 10,000 *PN* cells/L were measured), “false positive” (at least one particle beached but less than 10,000 *PN* cells/L were measured), and “false negative” (no particles beached but at least 10,000 *PN* cells/L were measured). We chose 10,000 *PN* cells/L as our threshold because this is the threshold used in the California Harmful Algal Risk Mapping (C-HARM) system to establish whether there is a *PN* bloom (C. R. Anderson et al., 2016). In these cases, daily results were only categorized if there was an observation at the beach, so days where no measurements were taken are considered inconclusive and are not taken into account for further analysis. From here, a variety of performance metrics were calculated for each of the beaching criteria, based on performance metrics outlined in (C. R. Anderson et al., 2010) and used in (C. R. Anderson et al., 2016). These metrics are accuracy, probability of detection, false alarm ratio, probability of false detection, and bias score, and their calculations are outlined in Table 4.1. These metrics provide a thorough evaluation of the different strengths and weaknesses of a particular beaching criteria, though ultimately, the importance of each of these metrics is dependent on the needs of the stakeholder. For example, in analysis of various observed *PN* bloom thresholds used in the C-HARM system, minimizing the false alarm ratio (FAR) compared to probability of detection (POD) was important to stakeholders, which resulted in an overall accuracy of 43%, though its best performing threshold had an overall accuracy of 67% (C. R. Anderson et al., 2016).

Table 4.1. Performance metrics and their calculations, as described in Anderson et al. (2010). Table adapted from Anderson et al. (2016).

Performance Metric	**Calculation**	**Range**
Accuracy	$\frac{true\ positives\ +\ true\ negatives}{total}$	0 – 1 (1 is best)
Probability of Detection (POD)	$\frac{true\ positives}{true\ positives + false\ negatives}$	0 – 1 (1 is best)
False Alarm Ratio (FAR)	$\frac{false\ positives}{true\ positives + false\ positives}$	0 – 1 (0 is best)
Probability of False Detection (POFD)	$\frac{false\ positives}{true\ negatives + false\ positives}$	0 – 1 (0 is best)
Bias Score	$\frac{true\ positives + false\ positives}{true\ positives + false\ negatives}$	0 – ∞ (1 is best)

4.3 RESULTS

4.3.1 *HAB and wind observations*

The purpose of this study was to ascertain whether the model simulates the observed patterns of *PN* cell beaching that originate in the Juan de Fuca eddy. Transport from the Juan de Fuca eddy starts with *PN* cells accumulating in the Juan de Fuca eddy under downwelling-favorable winds, escaping the eddy under upwelling-favorable winds, and then downwelling-favorable winds transporting *PN* cells to the coast (Hickey et al., 2013; MacFadyen et al., 2005; MacFadyen & Hickey, 2010). Therefore, analysis began by identifying events in the observational record that follow this pattern. First, we collected all available beach sampling data, resulting in a time series of *PN* cell counts from 2000 – 2018, with observations from 46 beaches in Washington and Oregon (Figure 4.2). In this figure, the cell counts are colored by level of severity, with the highest counts (>525,000 cells/L) plotted in red, medium counts (175,000 – 525,000 cells/L) plotted in yellow, low cell counts (1 – 175,000 cells/L) plotted in green, and measurements of no cells present plotted in grey. In this record, it is evident that typically, large events with high cell counts affect large swaths of the coast, typically occurring no more than a couple of times a year. Also, while the observational record is long, sampling at individual beaches was sporadic, leaving large gaps in the record, particularly in Oregon. The inconsistency in measurements may make it difficult to derive any meaningful patterns in terms of which beaches are more prone to HABs and which beaches are not. However, the record is a powerful tool for testing the forecasting capabilities of the model. The purpose of this paper is to investigate whether the model reproduces the observed patterns of *PN* cell beaching that originate in the Juan de Fuca eddy, so we will focus on summer events that affect beaches above the Columbia River mouth (46˚N – 48˚N).

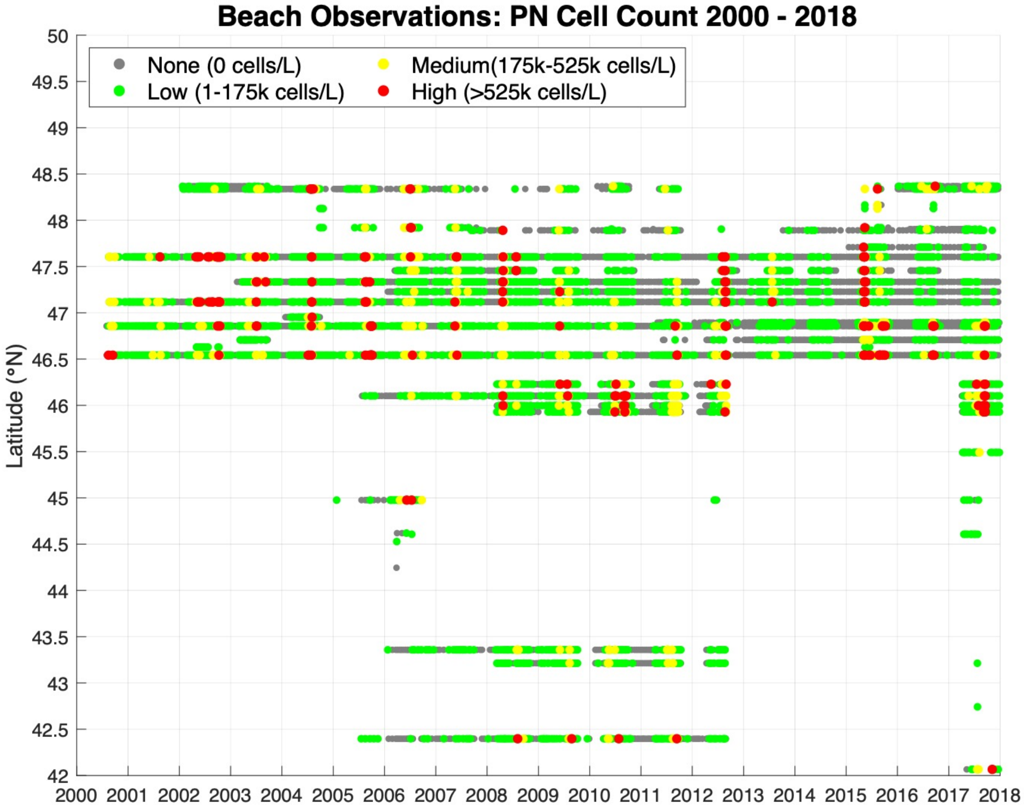

Figure 4.2. Beach observations of *PN* cell counts over 2000 – 2018 and 42˚N – 50˚N, colored by cell counts. Measurements of 0 cells/L are plotted in grey (none), measurements of low cell counts (1 – 175,000 cells/L) are plotted in green, measurements of medium cell counts (175,000 – 525,000 cells/L) are plotted in yellow, and measurements of high cell counts (>525,000 cells/L) are plotted in red.

In comparing the observational HAB record with meridional wind stress derived from satellite winds in each summer for each year corresponding to overlapping model output, we were able to identify beaching events that appear to follow the proposed mechanism. An example of one of these HAB events from 2004 is plotted in Figure 4.3. The dashed box outlines the identified event, with intermittent winds shifting from downwelling-favorable (accumulation in the eddy; red shading) to upwelling-favorable winds (escape from the eddy; blue shading), then followed by a wind relaxation (transport to beach; red or lighter blue shading) and *PN* cells observed at the beach. With this particular event, *PN* cells first beach at northern latitudes closest to the Juan de Fuca eddy, while at more southern latitudes, *PN* cells take a little longer to be transported from the Juan de Fuca eddy down the coast and then beach. Events were identified in several of the years analyzed. These events were then investigated using the particle tracking experiments in the model, as seen in Figure 4.4, though summers were also investigated as a whole for each of the years from 2004 – 2007 and 2013 – 2017.

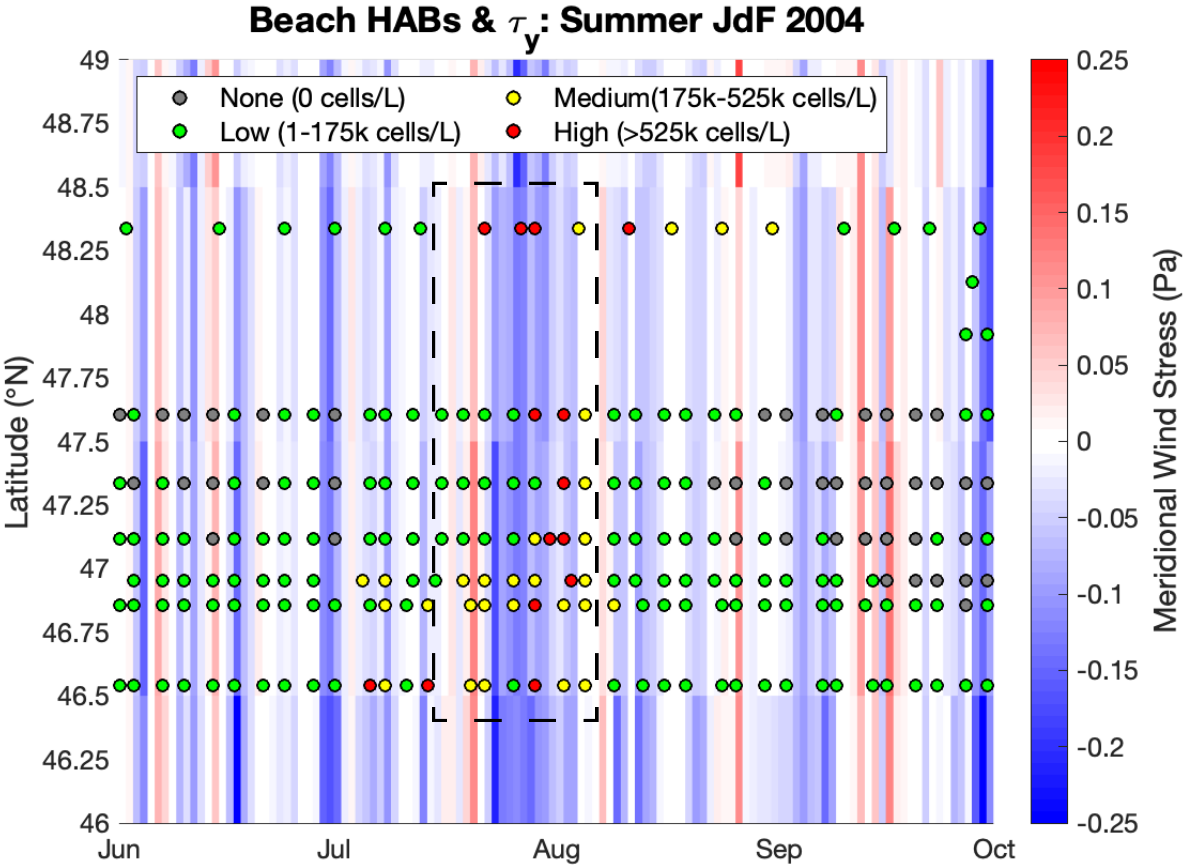

Figure 4.3. An example figure used to identify events in observations that match the proposed mechanism of accumulation, escape, and transport to the coast from the Juan de Fuca eddy. In this figure, depicting summer 2004 from 46˚N – 49˚N, beach HAB observations (colored circles, colored as in Figure 4.2) are plotted on top of meridional wind stress (red and blue shading). The black dashed box represents an identified event, where there is accumulation of *PN* cells in the Juan de Fuca eddy under downwelling-favorable conditions (red shading), then *PN* cells escape from the eddy (blue shading), and finally *PN* cells transport onshore (red or lighter blue shading and *PN* cells observed on the beach). For this last step, *PN* cells beach following a wind relaxation, where upwelling-favorable winds (darker blue shading) shift to downwelling-favorable winds (red shading) or weaker upwelling-favorable winds (lighter blue shading).

4.3.2 *Particle tracking experiments*

Using plots like the one shown in Figure 4.3, events that match the proposed transport mechanism from the Juan de Fuca eddy were identified for 2004, 2005, 2006, 2013, 2015, and 2017. Using the particle tracking experiments, we recreated these events in the model (Figure 4.4). In each of these plots, particle tracks are mapped from 10 days before the identified event to 10 days after, with particles that beach plotted in green and particles that do not beach plotted in grey. In all of the maps shown in Figure 4.4, "beached" particles are any particles that cross the 30 m isobath at any point along their track. The maximum observed cell counts at beaches in the region are also plotted on the maps.

In all of these figures, there are many particles that are transported equatorward along the shelf and slope, though the alongcoast extent of their transport varies between events. It is also evident that most particles pass very close to the coast in the immediate vicinity of their release near the mouth of the Strait of Juan de Fuca, and then move down the coast at a distance offshore that would not be considered "beached" by our definition farther south. This pattern is especially evident in the 2005 and 2013 events between 46˚N – 47˚N (Figure 4.4b, e).

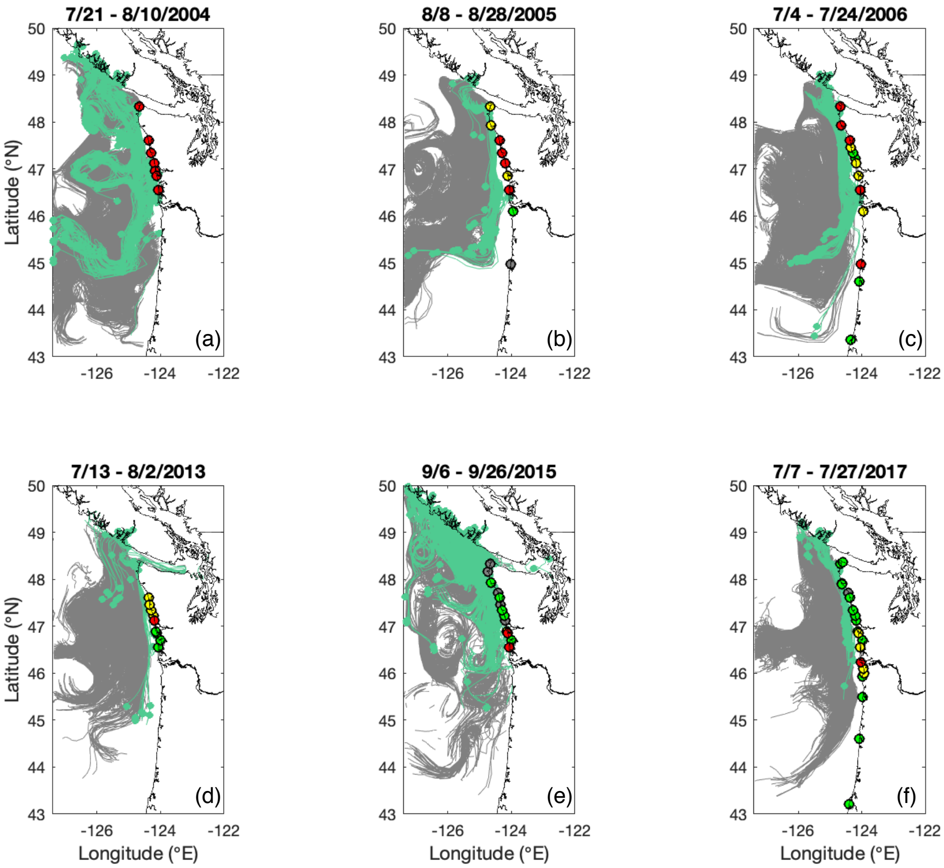

Figure 4.4. Maps of particle tracks for events identified in observations from 2004, 2005, 2006, 2013, 2015, and 2017, as demonstrated in Figure 4.3. In each figure, particles that beach within ±10 days of each identified event (defined as passing the 30 m isobath, in this case) are plotted in green, while particles that do not beach during this time period are plotted in grey. Observed cell concentrations are plotted at sampled beaches (grey, green, yellow, and red circles), indicating the maximum measured cell concentration over the 20-day period, using the same scale as used in Figure 4.2.

In addition to creating maps of particle tracks for these events, we also constructed heat maps depicting particles beaching in order to test the various beaching criteria outlined in Section 4.2.3. For each of these criteria, we analyzed the results from using the first beaching of each particle and using any beaching of each particle. Example heat maps for each of these beaching criteria –

by isobath (top) and by distance offshore (bottom) are plotted in Figure 4.5for the first beaching of each particle and in Figure 4.6 for any beaching of each particle for summer 2004. At first glance, it is evident that using the first beaching of each particle does not capture the reality of the observations because most particles are counted at the northern-most beach, with few particles transported south in late summer (Figure 4.5). This pattern persists even when latitudes above 47.5˚N are not counted, as is shown in Figure 4.5. The beaching criteria that comes the closest to capturing the patterns in the observations is the largest bin, 50 km offshore (Figure 4.5i), which accounts for much of the shelf.

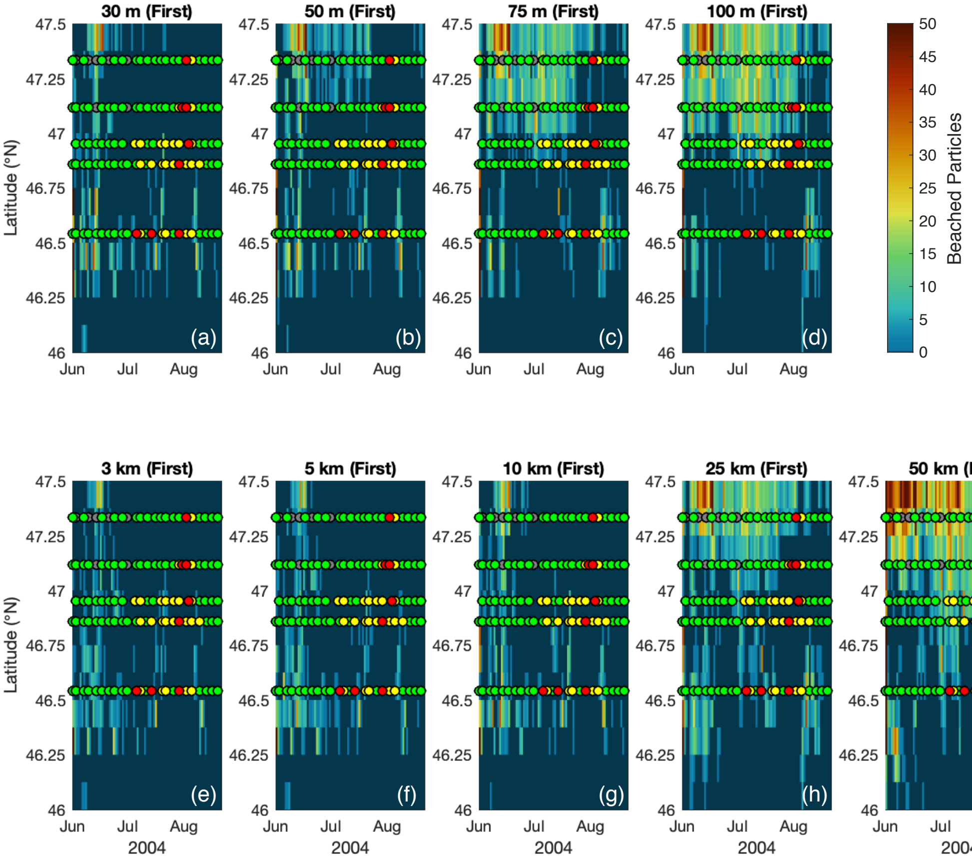

Figure 4.5. Example maps of number of particles beaching (shaded color) for each beaching criteria for summer 2004 based on the first beaching of each particle. Beaching criteria based on isobath are plotted on top (a-d) and beaching criteria based on distance offshore are plotted on bottom (e-i), both increasing to the right. The colored scale representing number of particles beached, ranging from 0 beached particles in dark blue to 50 beached particles in dark red, is the same scale used in Figure 4.6. Observed cell concentrations are plotted at sampled beaches (grey, green, yellow, and red circles), with the same scale as used in Figure 4.2.

With the beaching criteria that uses any beaching of each particle, particles are able to move southward and appear to better replicate the observations (Figure 4.6). Still, most particles beach in early summer when observed cell counts are lower, while many fewer particles beach later in the summer when the highest cell counts are observed. Furthermore, while particles with any beaching are able to move farther southward than they are using their first beaching, after the first big transport southward in the early summer, there is still a dearth of beached particles between 46˚N – 47˚N, contrary to observations. As with the beaching criteria using the first beaching of each particle (Figure 4.5), the criterion using any beaching of each particle that comes the closest to capturing the patterns in the observations is still the largest bin, 50 km offshore (Figure 4.6i), though the results from the 100 isobath criterion do well, too (Figure 4.6d), as further quantified in Section 4.3.3.

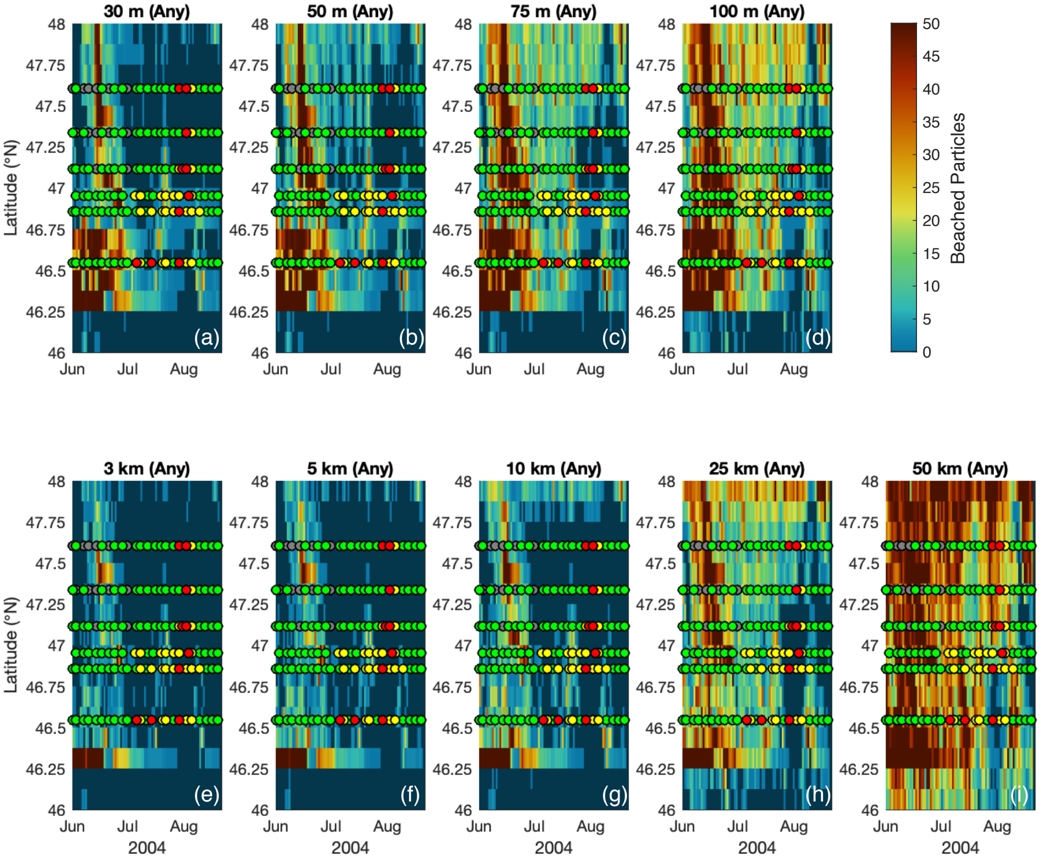

Figure 4.6. Example maps of number of particles beaching (shaded color) for each beaching criteria for summer 2004 based on any beaching of each particle. Beaching criteria based on isobath are plotted on top (a-d) and beaching criteria based on distance offshore are plotted on bottom (e-i), both increasing to the right. The colored scale representing number of particles beached, ranging from 0 beached particles in dark blue to 50 beached particles in dark red, is the same scale used in Figure 4.5. Observed cell concentrations are plotted at sampled beaches (grey, green, yellow, and red circles), with the same scale as used in Figure 4.2.

4.3.3 *Model performance*

To further address the performance of each of these beaching criteria, the fraction of true positives, true negatives, false positives, and false negatives were counted for each 0.125° latitude bin across all analyzed summers (from June 1 through the Fall transition for 2004 – 2007; 2013 – 2017). For this calculation, the daily beached particle count was compared with observed beach cell counts from the proceeding, corresponding, and following day, i.e. ±1 day. This analysis utilizes particle tracking results from all medium-resolution version of the model runs spanning 2004 – 2007 and 2013 – 2017 and does not distinguish between the concentration of *PN* cells observed at each beach, i.e. any measurement of at least 10,000 *PN* cell/L at a beach, including all green, yellow, and red events (shown in Figures 4.2, 4.5, 4.6), counts as a positive observation and any measurement of less than 10,000 *PN* cells/L at a beach counts as a negative observation. The results of this analysis show the performance of each beaching criterion spatially from 46˚N – 48˚N.

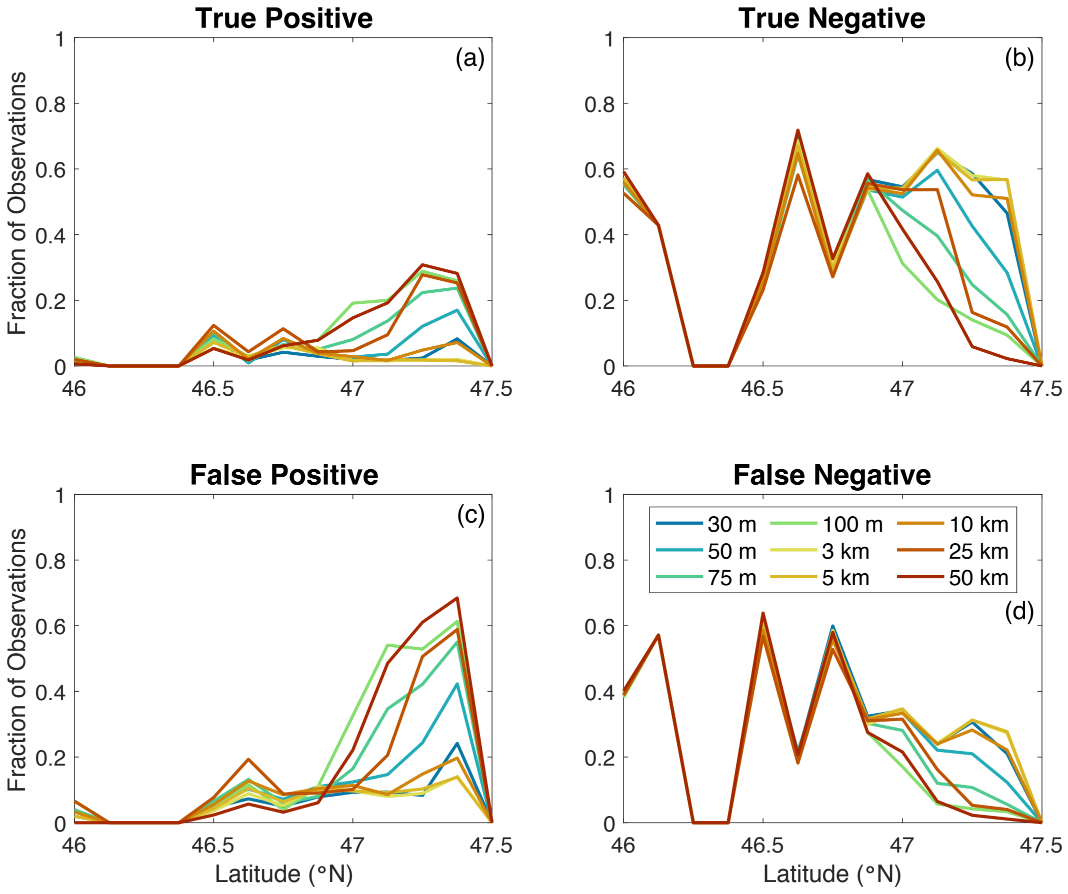

Figure 4.7. Fraction of true positives (a), true negatives (b), false positives (c), and false negatives (d) by latitude for each beaching criterion in summers 2004 – 2007 and 2013 – 2017 in the medium-resolution version of the model, based on the first beaching of each particle. Cooler colors represent criteria based on isobath while warmer colors represent criteria based on distance offshore (see legend).

As expected, using only the first beaching of each particle results in very few true positives and high levels of false negatives below 47˚N (Figure 4.7). This pattern persists for all beaching criteria, likely because most particles are beaching at the northern-most point in the model. With the narrowest beaching criteria (e.g., 3 km and 5 km offshore, 30 m isobath), there are very few true positives, though low levels of false positives, likely because very few particles beach under these strict criteria. On the positive side, since very few particles are beaching south of the northern-most sites, there are very few false positives.

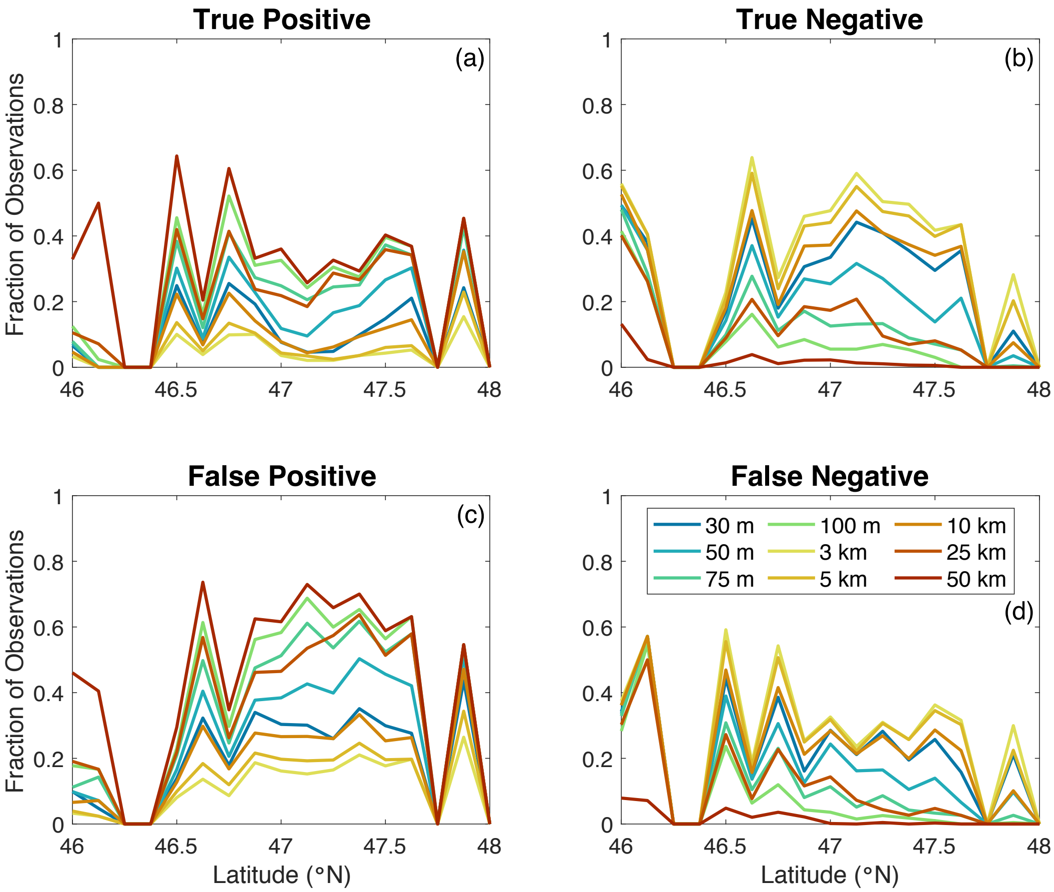

Figure 4.8. Fraction of true positives (a), true negatives (b), false positives (c), and false negatives (d) by latitude for each beaching criterion in summers 2004 – 2007 and 2013 – 2017 in the medium-resolution version of the model, based on any beaching of each particle. Cooler colors represent criteria based on isobath while warmer colors represent criteria based on distance offshore (see legend).

In comparison to the performance of the beaching criteria using the first beaching of each particle, the beaching criteria using any beaching of each particle performs much better, with higher counts of true positives throughout the study region (Figure 4.8). Still, there are numerous false negatives, particularly in the 46.5˚N – 47˚N, that are largely from later in the summer, as is evident in the heat maps like the ones shown in Figure 4.5. As suggested by the heat maps, the best performing beaching criteria are again the most generous as results from the 100 m isobath and from 50 km offshore have the most true positives and fewest false negatives, though these criteria also have some of the highest amounts of false positives.

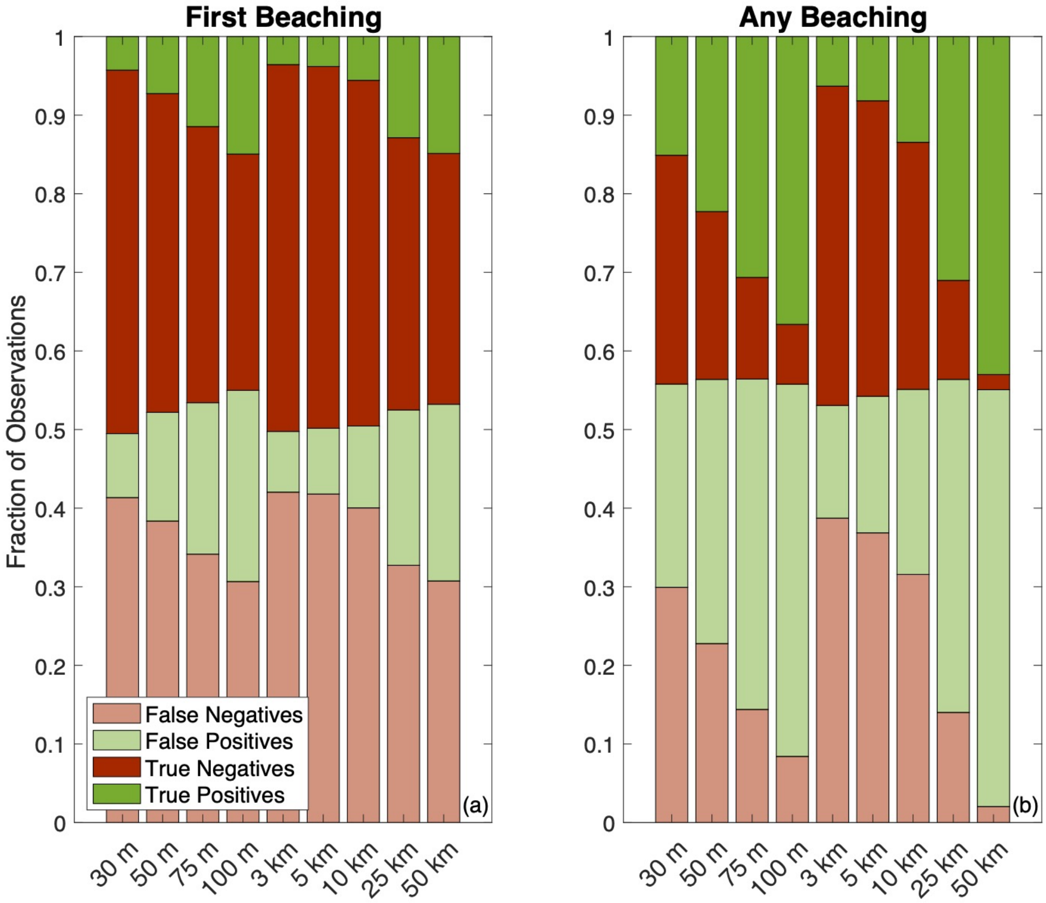

Figure 4.9. Mean fraction of true positives, true negatives, false positives, and false negatives for each beaching criterion in summers 2004 – 2007 and 2013 – 2017 in the medium-resolution version of the model, based on the first beaching of each particle (a) and on any beaching of each particle (b). Darker colors represent true positives (green) and negatives (red), while lighter colors represent false positives and negatives (see legend).

Unlike comparison of the fractions of true positives, true negatives, false positives, and false negatives between beaching criteria based on the first beaching of each particle and any beaching of each particle by latitude, comparison of mean fractions for each method suggests similar success at simulating reality. While using the first beaching of each particle results in slightly more success overall, this success is based on its capture of true negatives (red, Figure 4.9a). In doing so, it also results in a higher fraction of false negatives (light red, Figure 4.9a) compared to that of beaching criteria based on any beaching of each particle (light red, Figure 4.9b). Conversely, using any beaching of each particle results in more positives and fewer negatives overall and so its success is based on its capture of true positives (green, Figure 4.9b). Similarly, it also results in a higher fraction of false positives (light green, Figure 4.9b) compared to that beaching criteria based on the first beaching of each particle (light green, Figure 4.9a). Overall, while these methods perform similarly in terms of success, using any beaching of each particle is preferable because it results in more false positives than false negatives, which are inherently more dangerous because they indicate a failure to predict a potentially toxic HAB event.

Table 4.2. Model performance for beaching criteria, based on the first beaching of each particle, shaded by whether its value is “good” or bad”. For accuracy, values greater than or equal to 0.43 are green, while values less than 0.43 are red. For POD, values greater than 0.5 are green, while values less than or equal to 0.5 are red. For FAR and POFD, values less than 0.5 are green, while values greater than or equal to 0.5 are red. For bias score, values between 0.75 – 1.25 are green, while values outside that range are red. The threshold for whether an accuracy score is good or bad is based on results of the optimized threshold of the C-HARM system (C. R. Anderson et al., 2016), and the other thresholds for whether a score is “good” or “bad” are chosen based on what score is best according to their definitions (POD and Bias Score: 1 is best; FAR and POFD: 0 is best).

	30 m	**50 m**	**75 m**	**100 m**	**3 km**	**5 km**	**10 km**	**25 km**	**50 km**
Accuracy	0.51	0.48	0.47	0.45	0.50	0.50	0.50	0.48	0.47
POD	0.09	0.16	0.25	0.33	0.08	0.08	0.12	0.28	0.33
FAR	0.66	0.66	0.63	0.62	0.68	0.69	0.65	0.61	0.60
POFD	0.15	0.25	0.35	0.45	0.14	0.15	0.19	0.36	0.41
Bias Score	0.27	0.46	0.67	0.86	0.25	0.27	0.35	0.72	0.82

Using the mean spatial fractions of each of these categories, we calculated the metrics described in Section 4.2.3: accuracy, probability of detection (POD), false alarm ratio (FAR), probability of false detection (POFD), and bias score. At first glance, the accuracy of each of these metrics looks promising, with accuracy ranging from 45% – 50% (Table 4.2). For reference, the best overall accuracy score of the C-HARM system was 67%, though their threshold that performed best considering their goal to optimize FAR compared to POD had an accuracy of 43% (C. R. Anderson et al., 2016). Furthermore, these criteria all have relatively low POFDs, though this trend is most likely because very few particles are beaching throughout the study region. However, the POD scores and bias scores for all criteria are quite low. These results are likely because while this method does a good job of capturing true negatives with few false positives, it does a poor job of capturing true positives, as is evident in Figure 4.9a. Similarly, this method produces a lot of false negatives as well, which is also responsible for the low bias scores. Lastly, the high FAR scores indicate that false positives outnumber true positives with this method. Overall, these results illustrate the importance of considering a suite of metrics rather than relying on accuracy alone.

Table 4.3. Model performance for beaching criteria, based on any beaching of each particle shaded by whether its value is “good” or bad”, based on the scheme outlined in the caption of Table 4.2.

	30 m	**50 m**	**75 m**	**100 m**	**3 km**	**5 km**	**10 km**	**25 km**	**50 km**
Accuracy	0.44	0.44	0.44	0.44	0.47	0.46	0.45	0.44	0.45
POD	0.34	0.49	0.68	0.81	0.14	0.18	0.30	0.69	0.95
FAR	0.63	0.60	0.58	0.56	0.69	0.68	0.64	0.58	0.55
POFD	0.47	0.61	0.76	0.86	0.26	0.32	0.43	0.77	0.96
Bias Score	0.91	1.24	1.61	1.87	0.46	0.57	0.82	1.63	2.13

Calculation of the same metrics as above shows that using any beaching of each particle results in similar performance of the model using all beaching criteria in terms of accuracy as compared to the first beaching of each particle; however, all beaching criteria using any beaching of each particle have higher POD scores (Table 4.3). The best performing criteria in terms of accuracy and POD are the loosest, most generous beach definitions, the 100 m isobath and 50 km offshore. However, if bias score and low POFD is important to the stakeholder, then the narrower criteria in each category do best: beaching based on the 30 m isobath and 10 km offshore. The reason that no particular criterion stands out as a clear winner compared to the first beaching of each particle is that with this method, there are more positives, both true and false, than negatives, which dominate in the first beaching method (Figure 4.9). The abundance of false positives compared to false negatives is responsible for the high bias scores for most of these criteria. However, while use of any beaching results in more false positives, it also results in fewer false negatives, which are inherently more dangerous to a stakeholder. Overall, these performances again demonstrate the importance of considering more than one metric as well as stakeholder needs in model evaluation.

4.3.4 *Comparison of the medium-resolution and high-resolution versions of the model*

Lastly, the existence of a newer model version that overlaps with the old model version provides us with a unique opportunity to compare their performances in 2017. The high-resolution version of the model is a higher resolution model that includes more coastal rivers in its forcing than the medium-resolution version of the model, and the high-resolution version is currently used in forecasting for the PNW HAB Bulletin project. Similar analysis was conducted in the high-resolution version of the model and then compared with the results from the medium-resolution version. The most notable differences in these two versions are evident in the maps of particle tracks surrounding the identified event in 2017, shown in Figure 4.10. As plotted in Figure 4.4, these maps show beached particle tracks in green and tracks of particles that do not beach in grey, with the maximum observed cell counts plotted at the beaches following the same scale used in Figure 4.2. Again, “beached” particles are those that pass the 30 m isobath at any point along their track.

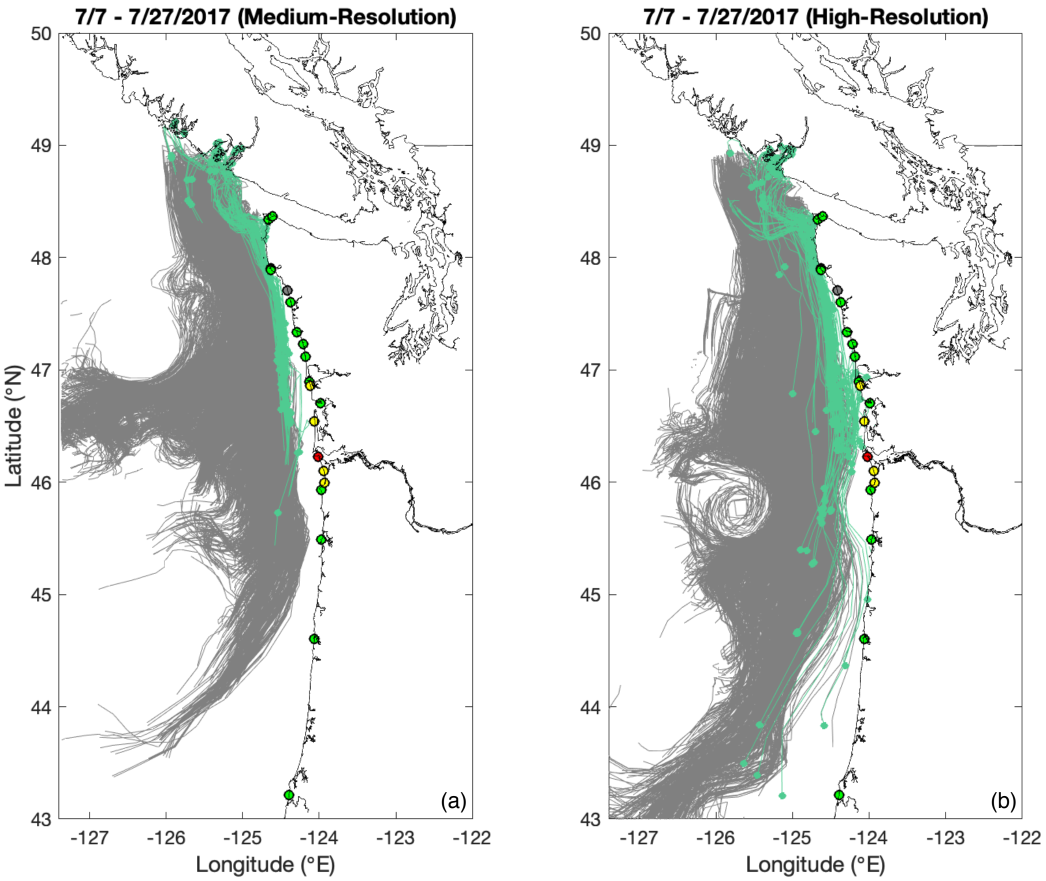

Figure 4.10. Maps of particle tracks for the 2017 event as demonstrated in Figure 4.3, using the medium-resolution version of the model (a) and the high-resolution version of the model (b). In each figure, particles that beach within ±10 days of each identified event (defined as passing the 30 m isobath, in this case) are plotted in green, while particles that do not beach during this time period are plotted in grey. Observed cell concentrations are plotted at sampled beaches (grey, green, yellow, and red circles), indicating the maximum measured cell concentration over the 20-day period, using the same scale as used in Figure 4.2.

With the medium-resolution version of the model, particles are closest to the coast near their release point and then stream down along the coast at distances that would not be considered "beached" by most of our beaching criteria farther south (Figure 4.10a). However, the high-resolution version exhibits stronger cross-shelf dispersion, particularly within the 46˚N – 47˚N band, as is evident in the particle tracks that flow closer to the coast as they move southward, with cross-shelf movement evident in their particle tracks (Figure 4.10b). Another notable difference is that there are many more particles that beach in the high-resolution version than those that beach in the medium-resolution version.

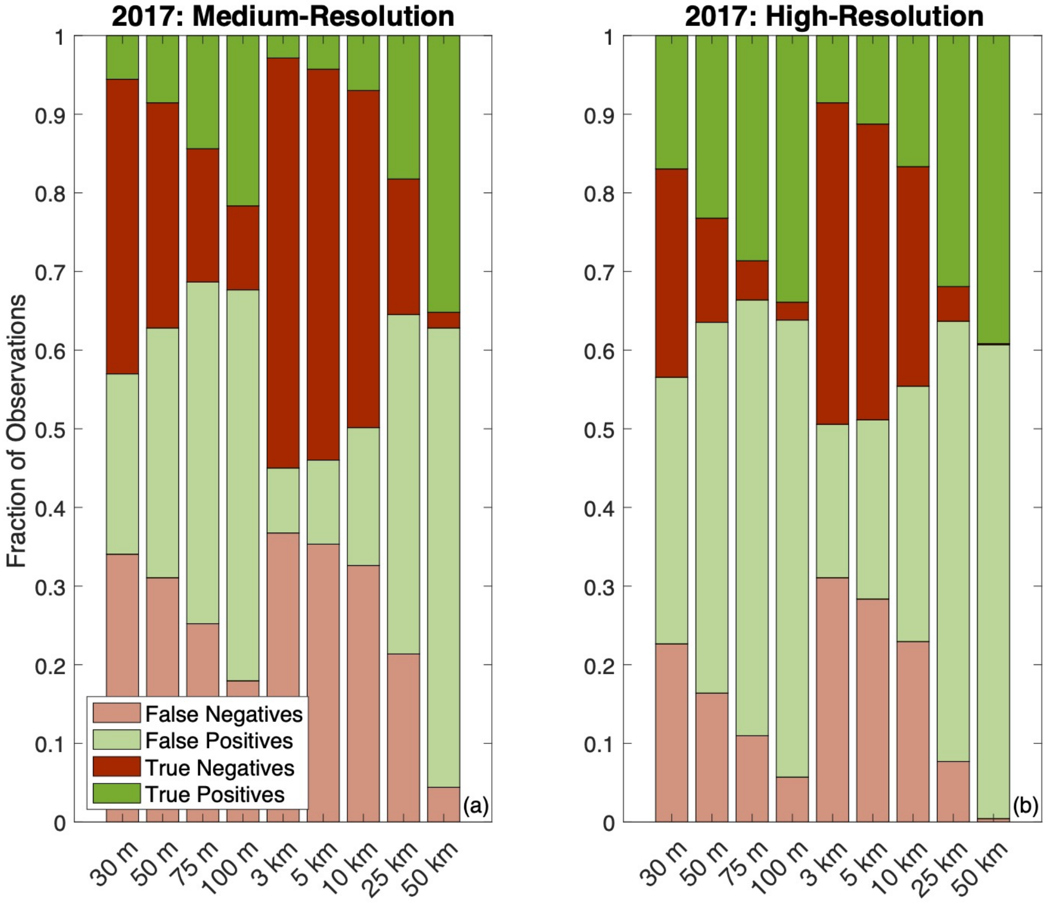

Figure 4.11. Mean fraction of true positives, true negatives, false positives, and false negatives for each beaching criterion in summer 2017 in the medium-resolution version of the model (a) and in the high-resolution version of the model (b), based on any beaching of each particle. Darker colors represent true positives (green) and negatives (red), while lighter colors represent false positives and negatives (see legend).

Similar to the comparison between beaching criteria based on the first beaching of each particle and those based on any beaching of each particle, the mean fraction of true positives, true negatives, false positives, and false negatives for each beaching criteria in the medium-resolution version of the model and in the high-resolution version of the model demonstrate similar success of both versions in simulating reality. However, closer inspection of the fractions of positives and negatives again suggests a winner. The high-resolution version of the model results in more positives, both true and false (greens, Figure 4.11b), than does the medium-resolution version of the model (greens, Figure 4.11a). Most importantly, the high-resolution version also results in fewer false negatives (light red, Figure 4.11b) compared with the medium-resolution version. Lastly, both versions have the largest fractions of true results at narrower beaching criteria (Figure 4.11), with the 30 m isobath in the high-resolution version of the model having an especially high fraction of true positives (Figure 4.11b). However, this pattern is not as pronounced in the results of the medium-resolution version of the model for all analyzed years (Figure 4.9b). Further analysis of more years in the high-resolution version of the model are necessary to determine if this pattern holds true for the high-resolution version.

Table 4.4. Model performance for beaching criteria in 2017 using any beaching of each particle for the medium-resolution version of the model, shaded by whether its value is "good" or bad", based on the scheme outlined in the caption of Table 4.2.

	30 m	**50 m**	**75 m**	**100 m**	**3 km**	**5 km**	**10 km**	**25 km**	**50 km**
Accuracy	0.43	0.37	0.31	0.32	0.55	0.54	0.50	0.35	0.37
POD	0.14	0.22	0.36	0.55	0.07	0.11	0.18	0.46	0.89
FAR	0.81	0.79	0.75	0.70	0.74	0.71	0.72	0.70	0.62
POFD	0.38	0.53	0.72	0.82	0.14	0.18	0.29	0.71	0.97
Bias Score	0.72	1.02	1.46	1.80	0.28	0.38	0.62	1.55	2.36

Table 4.5. Model performance for beaching criteria in 2017 using any beaching of each particle for the high-resolution version of the model, shaded by whether its value is "good" or bad", based on the scheme outlined in the caption of Table 4.2.

	30 m	**50 m**	**75 m**	**100 m**	**3 km**	**5 km**	**10 km**	**25 km**	**50 km**
Accuracy	0.43	0.36	0.34	0.36	0.49	0.49	0.45	0.36	0.39
POD	0.43	0.59	0.72	0.86	0.22	0.28	0.42	0.81	0.99
FAR	0.67	0.67	0.66	0.63	0.70	0.67	0.66	0.64	0.61
POFD	0.56	0.78	0.92	0.96	0.32	0.38	0.54	0.93	1.00
Bias Score	1.28	1.78	2.12	2.32	0.71	0.86	1.24	2.22	2.51

As done previously, performance metrics were calculated for both of these model versions based on their fractions of true positives, true negatives, false positives, and false negatives. The high-resolution version of the model performs similarly (Table 4.5) to the medium-resolution version of the model (Table 4.4). However, the most notable difference between these two performances are the consistently higher bias scores of the high-resolution version of the model. A higher bias score reflects a higher ratio of false positives to false negatives, which may be more preferable for stakeholders as false negatives can be more dangerous. Based on these metrics, in the high-resolution version of the model, the narrower beaching criteria, 30 m isobath and 3 – 10 km offshore, do well in terms of accuracy and bias score, with results from the 30 m isobath showing a promising POD score and the results from 3km – 10 km offshore showing promising POFD scores (Table 4.5). Aside from accuracy, the same metrics for the same criteria in the medium-resolution version of the model all perform worse (Table 4.4) compared with those from the high-resolution version.

4.4 DISCUSSION

Overall, the analysis of the high-resolution version of the model alleviates many of the concerns with the results using the medium-resolution version, particularly with regards to the cross-shelf dispersion, evident in particle tracks as they were transported southward along the coast, that was largely absent in the medium-resolution version of the model (Figure 4.10). This crucial difference is most likely the reason why the more realistic 30 m isobath beaching definition (the 30 m isobath approximates the beginning of the inner shelf where the surface and bottom layers interact (Lentz & Fewings, 2012)) performs better in the high-resolution version of the model than it does in the medium-resolution version. With the cross-shelf dispersion in the high-resolution version, instead of only moving meridionally along the coast, particles are also moving zonally and crossing the 30 m isobath more frequently as they are transported along the coast (Figure 4.10).

This observation begs the question: why is the cross-shelf dispersion so much weaker in the medium-resolution version of the model? The most notable differences between these two model versions are that the newer version is higher resolution, is forced by a higher resolution model at its open ocean boundaries as well as by higher resolution winds, and includes more coastal rivers in its forcing. Given the distance from the shelf to the open-ocean boundaries, it is unlikely that the higher resolution model forcing is responsible for the improved cross-shelf dispersion in the high-resolution version. However, previous studies suggest that coastal rivers may improve cross-shelf dispersion. In a modeling study by Banas, MacCready, et al. (2009), they found that the Columbia River plume increases cross-shelf dispersion, resulting in 25% more export across the shelf when the Columbia River and coastal estuaries were present in the model than when they were not. Their results also show the eddies and instabilities that arise within the shelf region due to the interactions of the buoyant plume, the denser oceanic water, and variable winds. On smaller scales, with rivers that are much less prominent than the Columbia River, these plume interactions with both oceanic water and the wind might promote cross-shelf dispersion. The high-resolution version of the model includes 18 more coastal rivers than the medium-resolution version of the model, which only includes the Columbia River (Giddings et al., 2014; MacCready et al., In Prep). The influence of these small, but numerous, coastal rivers could be responsible for the increase in cross-shelf dispersion within the high-resolution version of the model. It is also possible that this increase is due to the higher resolution of the high-resolution version, which may better resolve the influence of submesoscale processes and internal tides in promoting cross-shelf dispersion (e.g., Brink (2016); Davies and Xing (2001); Lévy et al. (2012); Noble et al. (2009)). Further analysis, including comparison of salinity and cross-shelf velocity over the shelf, could help untangle these influences and better understand the discrepancy in strength of cross-shelf dispersion between these two models.

Despite the role that rivers may play in facilitating more cross-shelf flow within the high-resolution version of the model, the Columbia River plume largely acts as a barrier to the coast, particularly during downwelling-favorable winds. These effects are particularly evident in the region immediately north of the Columbia River mouth (~46.25˚N) where we found a lot of false negatives, i.e. where there were no particles beaching in the model but there were *PN* cells observed in that region, a pattern also observed in other modeling studies that investigated the influence of the Columbia River plume (Banas, MacCready, et al., 2009; Giddings et al., 2014). However, the existence of false negatives in this region suggests that while particles may not be getting to the beach in this region because of the Columbia River plume in the model, *PN* cells are getting to these beaches under similar conditions. Previous studies suggest that it is often a race between the Columbia River plume and the upwelling front to get to the beach first during these wind reversals from upwelling to downwelling (Austin & Lentz, 2002; Giddings et al., 2014). Perhaps *PN* cells are able to beat the plume to the coast by some mechanism that is not well-captured by the model. This mismatch between the model and observations warrants further investigation using particle tracking experiments with non-surface-trapped particles or analysis of the model's phytoplankton within the extent of the Columbia River plume.

The success of particle tracking experiments can be difficult to assess because false positives are inevitable in this type of work. Even under ideal conditions, with wind patterns that mirror the proposed mechanism for *PN* cells to accumulate and escape from the Juan de Fuca eddy, and then be transported to the beach, in reality, there are not always *PN* cells in the Juan de Fuca eddy waiting to escape. Giddings et al. (2014) found some success with applying a chlorophyll criterion to their particle tracking experiments, though it was not always the case that phytoplankton observed in the eddy were *PN*. While there has been progress in understanding what factors are important for *PN* growth, such as high nutrient supply and retentive features (Pitcher et al., 2010; Trainer et al., 2000), there is still a lot unknown. Additional understanding of the drivers of growth of *PN* is imperative to furthering the success of such forecasting systems.

In addition, this paper operates under the assumption that the proposed mechanism of HAB transport from the Juan de Fuca eddy is true (MacFadyen et al., 2005; MacFadyen & Hickey, 2010); however, as evidenced by Figure 4.3, which shows meridional wind stressed overlaid by *PN* cell counts at beaches, the reality is messier than the idealized hypothesis. Looking at summer records, it is apparent that while there are events like the one highlighted in Figure 4.3 from 2004 that appear to fit the proposed mechanism, there are also many beaching events observed that are more complex and do not usually match the proposed mechanism. However, this analysis only considers summer beaching events from one source, the Juan de Fuca eddy. *PN* cell beaching events in spring and early summer typically originate at Heceta Bank and follow different dynamics in their transport to the beach (Hickey et al., 2013). Furthermore, as discussed in the Introduction, a recent study of the unusual HAB event in 2015, unprecedented in its spatial extent and in its severity, raised the possibility of a diffuse offshore source of *PN* cells rather than the identified “hot spots” for *PN* cell accumulation and growth (McCabe et al., 2016). This event was linked to anomalously warm ocean conditions, suggesting that these types of events could become more prevalent in the future under climate change. Capturing similar events that do not originate in a known “hot spots” like the Juan de Fuca eddy or at Heceta Bank may be more difficult and requires further investigation.

Additionally, given the sparseness of the sampling record, there could be times that the observed winds match the proposed mechanism, but there were not any measurements at the beach. This sparseness in sampling resulted in many particles beaching in the model that were ultimately inconclusive as there were not measurements with which to compare. It is unclear if these beached particles would result in positive or negative outcomes. Continuing sampling efforts and expanding their extent both spatially and temporally is important for furthering this work.

As C. R. Anderson et al. discussed in their 2010 and 2016 papers, the importance of metrics used to assess the performance of HAB models is largely dependent on the components of the model, as well as the goals of the stakeholder. As mentioned previously, this method of particle tracking results in numerous false positives, particularly with the high-resolution version of the model, which is largely due to the fact that our method relies only on the physics of the region. In this case, it would be unwise to focus on metrics that weigh heavily on the false positives, like particularly the false alarm ratio (FAR) and probability of false detection (POFD). With our model, false negatives are more problematic because they highlight flaws in the transport of particles onshore, as well as flaws in our assumption of the source of *PN* cells that beach, like if *PN* cells come from offshore rather than from the Juan de Fuca eddy. As discussed previously, results from the medium-resolution version of the model, particularly those from the narrowest beaching criterion and those that used the first beaching of each particle, were particularly prone to false negatives. If a stakeholder is using our model forecast to determine whether to open or close a beach for shellfish harvest, a false negative is far more dangerous to them than a false positive as a false negative could result in sickness or death of people, while a false positive may only result in a perhaps unnecessary beach closure. However, stakeholders will lose confidence in a model with a high rate of false positives if their decisions to close a beach to shellfish harvest that are based on the model continually prove to be for naught. In that regard, a bias score that is close to or slightly greater than 1 is ideal, as it would suggest a model with slightly more false positives than false negatives. Nonetheless, since both the bias score and the probability of detection (POD) are largely dependent on the prevalence of false negatives, which could be due to an incorrect assumption of the source of *PN* cells, their value might be much less interpretable those of the probability of false detection (POFD) and false alarm ratio (FAR), especially if the model were to incorporate biology into its forecasting, like Giddings et al. (2014). Still, the importance of each of these metrics is ultimately dependent on the needs of each individual stakeholder.

Finally, there are other caveats that bear mentioning with regards to our particle tracking scheme. While it is true that the cell concentration is not necessarily indicative of toxicity (Trainer et al., 2009) and thus the overall beached particle count may not as important, defining a beaching event based on a threshold of 1 particle beaching within 0.125˚ of latitude per day is perhaps too lenient. As part of their efforts to reduce false positives, Giddings et al. (2014) applied a threshold of 10 particles in 20 days within their 0.4˚ latitude band before it would be considered a beaching event. Similarly, our analysis considers any concentration of at least 10,000 *PN* cells/L as a positive observation in its comparison with the model results, rather than considering the various thresholds of *PN* cell concentration used in analysis of the observational data (e.g., Figure 4.2). Like the analysis of the C-HARM system (C. R. Anderson et al., 2016), similar analysis using a threshold of 1 *PN* cell/L resulted in vastly different performances of the beaching criteria between results based on the first beaching of each particle and those based on any beaching of each particle, as well as differences between the performance of the medium-resolution version of the model compared with that of the high-resolution version of the model (not shown). Future work should include testing of various particle count and *PN* cell concentration thresholds, as well as length of beaching window, to determine one that is both more realistic and more accurate. Similarly, we initially tested the beaching criteria using the first beaching of each particle, though this decision proved unsuccessful. We chose to use the first beaching because in reality, *PN* cells are finite, so if a *PN* cell is beached at a northern beach, it will not continue to move down the coast to beach at another, more southern beach. Once we started using any beaching of each particle, we found much more success, particularly in whether the model captures HAB events (true positives) rather than non-events (true negatives). This method reflects the idea that if a mass of water that could be carrying *PN* cells approaches the coast, some fraction of that water, and thus some fraction of the *PN* cells, are likely to reach the beach.

4.5 CONCLUSIONS

4.5.1 *Summary*

The goal of this study was to improve how the forecasting model is used in the PNW HAB Bulletin project by testing whether the model reproduces the observed patterns of *PN* cell beaching that originate in the Juan de Fuca eddy, based on particle tracking experiments in the model combined with observations of beach *PN* cell counts and meridional wind stress. We identified events in the observations that match the proposed mechanism of *PN* cell transport from the Juan de Fuca eddy to the coast, and then used particle tracks in the model to recreate these events. We also tested a variety of beaching criteria, defined by isobath and by distance offshore, as well as tested the model performance using the first beaching of each particle compared with any beaching of each particle. The success of these criteria was assessed by determining the fractions of true positives, true negatives, false positives, and false negatives within the model in comparison with observations, as well as calculating a variety of model performance metrics (Table 4.1). Lastly, we compared the summer 2017 performance of the medium-resolution version of the *Cascadia* model with that of the high-resolution version of the *Cascadia* model, which is currently used in forecasting for the PNW HAB Bulletin project.

1. *Using any beaching of each particle was more successful at simulating HAB events in the model than using the first beaching of each particle.*

   As is evident in Figure 4.5, if only the first beaching of each particle is used, most particles beach at the northern-most latitudes because most particles are transported closely past the mouth of the Strait of Juan de Fuca after their escape from the Juan de Fuca eddy (Figure 4.4). This pattern is observed with every beaching criterion, and there is fair performance for most of the calculated metrics (Table 4.2), this is largely due to the ability of this method to simulate non-events in the model (true negatives; Figure 4.9a). However, using any beaching of each particle results in more particles beaching throughout the study region (Figure 4.6), which more closely aligns with observations. Additionally, while these beaching criteria have similar overall metrics as those based on the first beaching each particle (Table 4.3), this method does a better job of simulating HAB events in the model (true positives, Figure 4.9b).

2. *The loosest beaching criteria successfully simulated the most HAB events in the medium-resolution version of the model.*

The loosest beaching criteria, by both isobath (100 m) and distance offshore (50 km), do an especially good job of capturing beaching events, particularly within the 47 – 48˚N band (Figures 4.6, 4.8). These criteria also exhibit the highest counts of true positives and lowest false negatives (Figure 4.9b) and have good metrics, with about 45% accuracy (Table 4.3). However, all beaching criteria in the medium-resolution version of the model performed similarly in terms of accuracy (44% – 47%, Table 4.3), with narrower criteria simulating more non-events than HAB events and looser criteria simulating more HAB events than non-events (Figure 4.9b).

3. *Based on comparisons from particle tracking experiments for summer 2017, the high-resolution version of the model performs better than the medium-resolution version utilizing a narrower beaching criterion, which is promising for future forecasting.*

Maps of particle tracks comparing the medium-resolution version of the model with the high-resolution version of the model show more particles beaching under the 30 m isobath beach definition as well as more cross-shelf dispersion within the 46˚N – 47˚N band in the high-resolution version (Figure 4.10). Furthermore, the high-resolution version of the model performs better according to all metrics, aside from accuracy, (Table 4.5) than does the medium-resolution version of the model (Table 4.4). Its best performing beaching criterion, using any beaching of each particle, is the 30 m isobath beaching definition, which best simulates reality, with the most HAB events compared to non-events (Figure 4.11b).

4.5.2 *Future Work*

As usual, the results of this study provide many avenues for future work in understanding transport pathways of HABs to the coast. As noted above, future work should incorporate the application of different thresholds for beaching and different comparison windows. This analysis uses one beached particle and ±1 day when comparing with observations to categorize each event. One beached particle in a 0.125˚ latitude range is an exceedingly small threshold, especially when compared with the sheer number of particles released each year. Similarly, this analysis does not consider the various thresholds of *PN* cell concentration used in analysis of the observational data in its comparison with the model results, instead considering any concentration of at least 10,000 *PN* cells/L as a positive observation. Future work should experiment with a variety of thresholds and comparison windows, as well as test the performance using a probabilistic approach to establish the most accurate parameters and methodology for future forecasting.

Additionally, this paper only focuses on the HABs sourced from the Juan de Fuca eddy. As noted in the Introduction, the retentive region at Heceta Bank is thought to be an important source of HABs, particularly in the spring. Additionally, *PN* cells that originate from offshore rather than from a known "hot spot" have recently been found to be important as well. Applying beaching criteria from the results of this study to see if particles released from Heceta Bank and from offshore in the model follow similar beaching patterns is an important next step. Similarly, expanding the analysis area beyond 46˚N – 48˚N in the summer months should also be a priority in future work.

Lastly, and perhaps most importantly, further experimentation with the high-resolution version of the model is imperative for optimizing the performance of the forecasting system as part of the PNW HAB Bulletin. As is apparent in the simple comparison of the results between the medium-resolution version and high-resolution version in 2017, the high-resolution version of the model performs markedly better than the medium-resolution version of the model. In addition to its more realistic cross-shelf flow, which warrants its own investigation in the future, the high-resolution version has the best performing beaching criteria matching more closely with reality (30 m isobath) rather than the extremely generous 50 km offshore beaching criteria that performs best in the medium-resolution version, likely due to the medium-resolution version's weaker cross-shelf dispersion. Given these advantages and the fact the high-resolution version is currently used for forecasting for the PNW HAB Bulletin, future work to optimize the forecasting system should focus on analysis and experimentation within the high-resolution version. This skill assessment of model-based hindcasts compared with historic beach sampling data within the high-resolution version of the model will serve as a guide for the future role of the forecast model in expert synthesis for the bulletin. Overall, this work will provide more region-specific forecasts that will better prepare PNW communities for HAB impacts.

4.6 ACKNOWLEDGMENTS

Special thanks to the MacCready and Banas lab groups for useful conversations; to collaborators in the PNW HAB Bulletin, particularly Ryan M. McCabe, Vera L. Trainer, Barbara M. Hickey, Dan L. Ayres, and Matthew Hunter; to Evelyn Lessard for guidance; and to David Darr for computer cluster administration and support. This chapter is co-authored by Neil S. Banas and Parker MacCready. H. Stone was supported by a National Science Foundation (NSF) Graduate Research Fellowship. P. MacCready, N. Banas, and H. Stone were supported by MERHAB grant number NA16NOS4780189 from the Coastal Ocean Program of the National Oceanic and Atmospheric Administration (NOAA). PM was also supported by the IOOS regional association NANOOS, and the Washington Ocean Acidification Center. This is a contribution of the MERHAB program. The findings and conclusions are those of the authors and do not necessarily reflect those of NSF, NOAA, or the Department of Commerce. This work is part of a larger collaboration that includes partnership with MERHAB program, ORHAB partnership, Makah Tribe, National Centers for Coastal Ocean Sciences (NCCOS), Northwest Fisheries Science Center (NWFSC), Olympic Coast National Marine Sanctuary (OCNMS), Quileute Tribe, Quinault Indian Nation, Washington Department of Fish and Wildlife (WDFW), Washington State Department of Health (WDOH), Oregon Department of Fish and Wildlife (ODFW), NOAA National Ocean Service, NCCOS Ecology and Oceanography of Harmful Algal Blooms (ECOHAB) program, NOAA Oceans and Human Health Initiative, and Centers for Disease Control.

Chapter 5. CONCLUSION

This dissertation sought to characterize some of the effects of transport on coastal productivity and harmful algal blooms in the Pacific Northwest coastal ocean (also referred to as the Northern California Current System) and greater California Current System (CCS). The three studies described in this manuscript utilize both observations and model output to examine the effects of transport on bottom water (Chapter 2), phytoplankton productivity (Chapter 3), and beaching of harmful algae (Chapter 4). The results of each of these studies are outlined below.

5.1 CHAPTER SUMMARIES

5.1.1 *The effect of alongcoast advection on Pacific Northwest shelf and slope water properties in relation to upwelling variability*

The goal of Chapter 2 was to investigate the effect of upwelling variability and large-scale advection on slope and shelf water properties in the Northern CCS, both of which can significantly affect water chemistry. Salinity and temperature fields from a 7-year ROMS hindcast model of this region (43°N - 50°N), along with extensive particle tracking, were used to study interannual variability in water properties over both the upper slope and the mid-shelf bottom. Variation in slope water properties was an order of magnitude smaller than on the shelf. Furthermore, the primary relationship between temperature and salinity anomalies in mid-shelf bottom water consisted of variation in density (cold/salty vs. warm/fresh), nearly orthogonal to the anomalies along density levels (cold/fresh vs. warm/salty) observed on the upper slope. These mid-shelf anomalies were well-explained ($R^2 = 0.6$) by the combination of interannual variability in local and remote alongshore wind stress, and depth of the California Undercurrent core. Lagrangian analysis of upper slope and mid-shelf bottom water shows that both are affected simultaneously by large-scale alongcoast advection of water through the northern and southern boundaries. The amplitude of anomalies in bottom oxygen and dissolved inorganic carbon on the shelf associated with upwelling variability are larger than those associated with typical variation in alongcoast advection and are comparable to observed anomalies in this region. However, a large northern intrusion event in 2004 illustrates that particular, large-scale alongcoast advection anomalies can be just as effective as upwelling variability in changing shelf water properties on the interannual scale.

5.1.2 *Linking chlorophyll concentration and wind patterns using satellite data in the Central and Northern California Current System*

In Chapter 3, we explored the relationship between phytoplankton productivity, wind patterns, and retention in the Central and Northern CCS, a highly productive region due to wind-driven upwelling, which supplies nutrients to the euphotic zone. Numerous studies of the relationship between phytoplankton productivity and wind patterns suggest that an intermediate wind speed yields the most productivity on the shelf. However, few studies have considered the productivity-wind relationship across the entire CCS, including the Northern CCS (north of 42˚N), an unusually productive region with highly variable upwelling- and downwelling-favorable winds. Using satellite chlorophyll concentration from GlobColour together with QuikSCAT and ASCAT winds, we examined the relationship between shelf (shallower than the 150 m isobath) chlorophyll concentration and wind patterns in the Central and Northern CCS. Results from this analysis suggest that while there is a dome-shaped relationship between mean chlorophyll concentration and wind stress for the whole system, the Central and Northern CCS have significantly different relationships, which is evident in the separation between their mean chlorophyll concentration-wind stress curves. The Northern CCS also supports high chlorophyll concentration during downwelling-favorable winds. To understand this difference in chlorophyll concentration-wind stress relationships, results from particle tracking experiments using a ROMS model of the Northern CCS are used to map shelf retention times with respect to wind patterns. These results suggest that on the 1°-latitude scale, the effect of wind intermittency on retention is minimal in the Northern CCS; however, this result does not disqualify the influence of more complex controls on retention like wind intermittency on smaller spatial scales. Lastly, we presented a revised hypothesis to describe the relationship between chlorophyll concentration and wind stress in the CCS that includes the influence of non-upwelling-derived nutrients in the Northern CCS.

5.1.3 *Modeling transport of harmful algal blooms to Pacific Northwest coastal beaches*

In Chapter 4, we used particle tracking experiments in a ROMS model to test whether the model reproduces the observed beaching patterns of *Pseudo-nitzschia* (*PN*) cells, a diatom that sometimes produces a neurotoxin called domoic acid that causes amnesic shellfish poisoning. This work was part of the Pacific Northwest's HAB Bulletin program, a partnership between academic, government, and tribal stakeholders that uses a combination of monitoring programs and modeling to better understand the formation, evolution, and transport of HABs in this region. This program produces periodic bulletins to inform local stakeholders of current and forecasted conditions. One of the goals of this chapter was to help improve how the forecasting model is used in the bulletin's preparation. Using observations of beach cell counts and meridional wind stress, we identified events in the observations that match the proposed mechanism of transport from the Juan de Fuca eddy to the coast, and then used particle tracks in the model to simulate these events. We also tested a variety of criteria, using both depth and distance offshore, to define when a particle was close enough to the coast that it was likely to correspond to cells appearing in the intertidal zone and in shellfish diets. Allowing for single or multiple coastal proximity events was also considered. The success of these criteria was assessed by determining the fraction of true positives, true negatives, false positives, and false negatives within the model in comparison with observations, as well as calculating a variety of model performance metrics. Lastly, we compared the performance of a medium-resolution (1.5 km) version of the model with that of a high-resolution (0.5 km) version of the model, the latter of which is currently used in forecasting for the PNW HAB Bulletin project. We found that allowing for multiple coastal proximity events as well as using the loosest beaching criteria resulted in the most successfully simulated HAB events in the medium-resolution version of the model, and that the high-resolution version of the model performed better than the medium-resolution version.

5.2 FUTURE WORK

While these studies help explain some of the effects of transport on the biology both at the sea floor and at the sea surface, there is still much more to investigate. As expected, all three of these studies highlight the importance of longer time series and greater spatial extent for studying various phenomena. For example, while results in Chapter 2 suggest that typically the strength, vertical structure, and apparent source depth of upwelling has a larger effect than does large-scale advection on slope and shelf water properties, anomalous large-scale alongcoast intrusion events can have just as large of an effect. However, this type of event was only observed once during the study period. A longer record would likely capture more events like this one and allow for investigation into the long-term variability and trends in both upwelling variability and in large-scale advection in the Northern CCS.

In addition to the benefit of greater temporal and spatial coverage, Chapter 3 and Chapter 4 highlight the importance of increased study of the role of rivers in the coastal ocean. Results in Chapter 3 suggest that the unusually high productivity of the Northern CCS is likely due to lateral nutrient fluxes, such as outflow from the Salish Sea and, to a lesser extent, river discharge. Furthermore, while results from the particle tracking experiment suggest that retention does not affect chlorophyll concentration on the 1° latitude-wide scale, retention on smaller scales may be significant. In addition to retention driven by geographic features and wind intermittency, the Columbia River plume can act as a retentive feature, allowing phytoplankton ample time and nutrients to grow while on the shelf. Similarly, the importance of the Columbia River plume was highlighted in Chapter 4 as it can act as both a barrier and a conduit to the coast for *Pseudo-nitzschia* cells, depending on its orientation. The mismatch between the model results and beaching record where particles were not beaching but *Pseudo-nitzschia* cells were in the vicinity of the plume suggest that there are some dynamics within the plume region that are not well resolved in the model. Lastly, comparison of the results from the medium-resolution version of the model with the results from the high-resolution version of the model suggest that the high-resolution version better resolves cross-shelf dispersion. This improvement is likely due to the inclusion of more coastal rivers in the high-resolution version. Further investigation into all of these various roles of rivers, both large and small, is imperative for understanding all of the dynamics that control phytoplankton productivity and HAB beaching events in the coastal ocean.

Finally, all three of these studies demonstrated the value and limitations of models in investigating a variety of phenomena. A well-validated physical model can provide us with incredible insight into the dynamics of a system, as demonstrated in all three chapters. For example, we were able to estimate the changes in water chemistry based on results of the analysis of the physical model combined with observed oxygen and dissolved inorganic carbon concentrations in Chapter 2. In Chapter 3, we were able to characterize the importance of retention in fueling the unusually high chlorophyll concentrations in the Northern CCS through analysis of the particle tracking experiments conducted in the physical model, while similar experiments described in Chapter 4provided insight into patterns of transport of harmful algal blooms to coastal beaches. Still, a fully coupled biogeochemical model would further our understanding of these dynamics, particularly our understanding of the role of lateral nutrient fluxes within the Northern CCS that fuel its unusually high primary productivity. Similarly, as suggested by the results from the comparison of the medium-resolution version of the model with the high-resolution version of the model, the higher-resolution version performed better in many aspects, particularly in its resolution of cross-shelf dispersion. Since much of the most interesting aspects of coastal productivity occur over the shelf, a model that resolves this region is imperative for future study.

5.3 CLOSING THOUGHTS

In closing, the experience of working on three distinct studies that focused on the same system has shed a lot of light on the role of models in oceanography, the importance of continued observations, and importance of continuing to test and refine hypotheses. While all of these studies explored the dynamics within a coastal upwelling system, they each examined distinctly different aspects. Still, all utilized model output and particle tracking experiments. The particle tracking experiments were particularly powerful for understanding the transport of water masses, regardless of whether that transport represented large-scale movement of cold, fresh Pacific Subarctic Upper Water or if that transport represented the movement of a tiny phytoplankton as it traversed the shelf. Models can be incredibly valuable for really digging into the dynamics of a particular region or phenomenon, even if those models are only resolving the physics. Imagine what you could learn with a fully coupled biogeochemical model!

However, these models would lose much of their value if not for the numerous observations that have been painstakingly gathered over time. These observations are extremely important for grounding our models in reality so that we may trust that our models are, in fact, simulating reality. Furthermore, as we move towards more ambitious forecasting models, such as one that can tell us where and when harmful algae will beach, confidence in that forecast is paramount for any stakeholder who might use that forecast in decision-making. Therefore, it is imperative that all observational programs, including everything from in situ measurements to satellite observations, continue to operate and expand so that we have greater temporal and spatial resolution for further model validation.

Lastly, and perhaps most importantly, these studies have demonstrated the importance of continuing to test and refine hypotheses. Each of these studies was motivated by a hypothesis that was ultimately refined. Chapter 2 was predicated on the idea that water from the California Undercurrent upwells onto the shelf and thus the properties of California Undercurrent water determine the properties of shelf bottom water. However, our study suggested that shelf bottom water properties are controlled by the strength of upwelling and the depth of the California Undercurrent rather than its composition. In Chapter 3, we tested the hypothesis presented in Botsford et al. (2003) that there is a peak at moderate wind stress in the relationship between wind stress and phytoplankton productivity. Our results supported this idea in general within the Central and Northern CCS but suggested that this peak is shifted in the Northern CCS by a non-upwelling-derived nutrient source. Finally, there are two known “hot spots” for *Pseudo-nitzschia* accumulation before they are transported to the beach, one of which is considered by our study in Chapter 4: the Juan de Fuca eddy. However, some recent studies, like McCabe et al. (2016), suggest that *Pseudo-nitzschia* can also come from a diffuse offshore source rather than these known hot spots. While we did not directly test this new hypothesis, the prevalence of false negatives in our study could be due to *Pseudo-nitzschia* cells that are not transported from the Juan de Fuca eddy but rather from this offshore source, a direction that will be included in future work. Overall, this continual testing and refining of hypotheses is integral to the pursuit of science, including understanding the transport effects on coastal productivity and harmful algal blooms.

BIBLIOGRAPHY

Alford, M. H., & MacCready, P. (2014). Flow and mixing in Juan de Fuca Canyon, Washington. *Geophysical Research Letters*, *41*(5), 1608–1615. https://doi.org/10.1002/2013GL058967

Allen, S. E., & Hickey, B. M. (2010). Dynamics of advection-driven upwelling over a shelf break submarine canyon. *Journal of Geophysical Research*, *115*(C8), C08018. https://doi.org/10.1029/2009JC005731

Anderson, C. R., Sapiano, M. R. P., Prasad, M. B. K., Long, W., Tango, P. J., Brown, C. W., & Murtugudde, R. (2010). Predicting potentially toxigenic Pseudo-nitzschia blooms in the Chesapeake Bay. *Journal of Marine Systems*, *83*(3–4), 127–140. https://doi.org/10.1016/j.jmarsys.2010.04.003

Anderson, C. R., Kudela, R. M., Kahru, M., Chao, Y., Rosenfeld, L. K., Bahr, F. L., et al. (2016). Initial skill assessment of the California Harmful Algae Risk Mapping (C-HARM) system. *Harmful Algae*, *59*, 1–18. https://doi.org/10.1016/j.hal.2016.08.006

Anderson, D. M., Cembella, A. D., & Hallegraeff, G. M. (2012). Progress in Understanding Harmful Algal Blooms : Paradigm Shifts and New Technologies for Research, Monitoring, and Management. *Annual Review of Marine Science*, *4*, 143–176. https://doi.org/10.1146/annurev-marine-120308-081121

Austin, J. A., & Lentz, S. J. (2002). The inner shelf response to wind-driven upwelling and downwelling. *Journal of Physical Oceanography*, *32*(7), 2171–2193. https://doi.org/10.1175/1520-0485(2002)032<2171:TISRTW>2.0.CO;2

Bakun, A. (1973). Coastal upwelling indices, west coast of North America. US Department of Commerce. *NOAA Technical Report, NMFS SSRF-671*.

Banas, N. S., McDonald, P. S., & Armstrong, D. A. (2009). Green Crab Larval Retention in Willapa Bay, Washington: An Intensive Lagrangian Modeling Approach. *Estuaries and Coasts*, *32*(5), 893–905. https://doi.org/10.1007/s12237-009-9175-7

Banas, N. S., Lessard, E. J., Kudela, R. M., MacCready, P., Peterson, T. D., Hickey, B. M., & Frame, E. (2009). Planktonic growth and grazing in the Columbia River plume region: A biophysical model study. *Journal of Geophysical Research*, *114*(9), C00B06. https://doi.org/10.1029/2008JC004993

Banas, N. S., MacCready, P., & Hickey, B. M. (2009). The Columbia River plume as cross-shelf exporter and along-coast barrier. *Continental Shelf Research*, *29*(1), 292–301. https://doi.org/10.1016/j.csr.2008.03.011

Banas, N. S., Conway-Cranos, L., Sutherland, D. A., MacCready, P., Kiffney, P. M., & Plummer, M. (2015). Patterns of River Influence and Connectivity Among Subbasins of Puget Sound, with Application to Bacterial and Nutrient Loading. *Estuaries and Coasts*, *38*(3), 735–753. https://doi.org/10.1007/s12237-014-9853-y

Barron, C. N., Kara, A. B., Martin, P. J., Rhodes, R. C., & Smedstad, L. F. (2006). Formulation, implementation and examination of vertical coordinate choices in the Global Navy Coastal Ocean Model (NCOM). *Ocean Modelling*, *11*(3–4), 347–375. https://doi.org/10.1016/j.ocemod.2005.01.004

Barron, C. N., Smedstad, L. F., Dastugue, J. M., & Smedstad, O. M. (2007). Evaluation of ocean models using observed and simulated drifter trajectories: Impact of sea surface height on synthetic profiles for data assimilation. *Journal of Geophysical Research: Oceans*, *112*(7), 1–11. https://doi.org/10.1029/2006JC003982

Barth, J. A., Cowles, T. J., Kosro, P. M., Shearman, R. K., Huyer, A., & Smith, R. L. (2002). Injection of carbon from the shelf to offshore beneath the euphotic zone in the California Current. *Journal of Geophysical Research*, *107*(C6), 3057. https://doi.org/10.1029/2001JC000956

Barth, J. A., Menge, B. A., Lubchenco, J., Chan, F., Bane, J. M., Kirincich, A. R., et al. (2007). Delayed upwelling alters nearshore coastal ocean ecosystems in the northern California current. *Proceedings of the National Academy of Sciences of the United States of America*, *104*(10), 3719–24. https://doi.org/10.1073/pnas.0700462104

Barton, A., Hales, B., Waldbusser, G. G., Langdon, C., & Feely, R. a. (2012). The Pacific oyster, Crassostrea gigas, shows negative correlation to naturally elevated carbon dioxide levels: Implications for near-term ocean acidification effects. *Limnology and Oceanography*, *57*(3), 698–710. https://doi.org/10.4319/lo.2012.57.3.0698

Battisti, D. S., & Hickey, B. M. (1984). Application of Remote Wind-Forced Coastal Trapped Wave Theory to the Oregon and Washington Coasts. *Journal of Physical Oceanography*, *14*(5), 887–903. https://doi.org/10.1175/1520-0485(1984)014<0887:AORWFC>2.0.CO;2

Beardsley, R. C., Dorman, C. E., Friehe, C. A., Rosenfeld, L. K., & Winant, C. D. (1987). Local atmospheric forcing during the Coastal Ocean Dynamics Experiment: 1. A description of the marine boundary layer and atmospheric conditions over a northern California upwelling region. *Journal of Geophysical Research*, *92*(C2), 1467. https://doi.org/10.1029/JC092iC02p01467

Bentamy, A., Grodsky, S. A., Carton, J. A., Croizé-Fillon, D., & Chapron, B. (2012). Matching ASCAT and QuikSCAT winds. *Journal of Geophysical Research: Oceans*, *117*(2), 1–15. https://doi.org/10.1029/2011JC007479

Bograd, S. J., & Mantyla, A. W. (2005). On the subduction of upwelled waters in the California Current. *Journal of Marine Research*, *63*(5), 863–885. https://doi.org/10.1357/002224005774464229

Bograd, S. J., Buil, M. P., Di Lorenzo, E., Castro, C. G., Schroeder, I. D., Goericke, R., et al. (2015). Changes in source waters to the Southern California Bight. *Deep Sea Research Part II: Topical Studies in Oceanography*, *112*, 42–52. https://doi.org/10.1016/j.dsr2.2014.04.009

Botsford, L. W., & Wickham, D. E. (1975). Correlation of upwelling index and Dungeness crab catch. *Fishery Bulletin*, *73*(4), 901–907.

Botsford, L. W., Lawrence, C. A., Dever, E. P., Hastings, A., & Largier, J. (2003). Wind strength and biological productivity in upwelling systems: an idealized study. *Fisheries Oceanography*, *12*(4–5), 245–259. https://doi.org/10.1046/j.1365-2419.2003.00265.x

Botsford, L. W., Lawrence, C. A., Dever, E. P., Hastings, A., & Largier, J. (2006). Effects of variable winds on biological productivity on continental shelves in coastal upwelling systems. *Deep Sea Research Part II: Topical Studies in Oceanography*, *53*(25–26), 3116–3140. https://doi.org/10.1016/j.dsr2.2006.07.011

Brink, K. H. (2016). Cross-Shelf Exchange. *Annual Review of Marine Science*, *8*(1), 59–78. https://doi.org/10.1146/annurev-marine-010814-015717

Campbell, J. W. (1995). The lognormal distribution as a model for bio-optical variability in the sea. *Journal of Geophysical Research*, *100*(C7), 13237. https://doi.org/10.1029/95JC00458

Chapman, D. C. (1987). Application of wind-forced, long, coastal-trapped wave theory along the California coast. *Journal of Geophysical Research*, *92*(C2), 1798. https://doi.org/10.1029/JC092iC02p01798

Chhak, K., & Di Lorenzo, E. (2007). Decadal variations in the California Current upwelling cells. *Geophysical Research Letters*, *34*(14), 1–6. https://doi.org/10.1029/2007GL030203

Connolly, T. P., & Hickey, B. M. (2014). Regional impact of submarine canyons during seasonal upwelling. *Journal of Geophysical Research: Oceans*, *119*(2), 953–975. https://doi.org/10.1002/2013JC009452

Connolly, T. P., Hickey, B. M., Geier, S. L., & Cochlan, W. P. (2010). Processes influencing seasonal hypoxia in the northern California current system. *Journal of Geophysical Research: Oceans*, *115*(3), 1–22. https://doi.org/10.1029/2009JC005283

Connolly, T. P., Hickey, B. M., Shulman, I., & Thomson, R. E. (2014). Coastal Trapped Waves, Alongshore Pressure Gradients, and the California Undercurrent*. *Journal of Physical Oceanography*, *44*(1), 319–342. https://doi.org/10.1175/JPO-D-13-095.1

Cury, P., & Roy, C. (1989). Optimal Environmental Window and Pelagic Fish Recruitment Success in Upwelling Areas. *Canadian Journal of Fisheries and Aquatic Sciences*, *46*(4), 670–680. https://doi.org/10.1139/f89-086

Davies, A. M., & Xing, J. (2001). *Modelling processes influencing shelf edge currents, mixing, across shelf exchange, and sediment movement at the shelf edge. Dynamics of Atmospheres and Oceans* (Vol. 34). https://doi.org/10.1016/S0377-0265(01)00072-0

Davis, K. A., Banas, N. S., Giddings, S. N., Siedlecki, S. A., MacCready, P., Lessard, E. J., et al. (2014). Estuary-enhanced upwelling of marine nutrients fuels coastal productivity in the U.S. Pacific Northwest. *Journal of Geophysical Research: Oceans*, *119*(12), 8778–8799. https://doi.org/10.1002/2014JC010248

Denman, K. L., & Freeland, H. J. (1985). Correlation scales, objective mapping and a statistical test of geostrophy over the continental shelf. *Journal of Marine Research*, *43*(3), 517–539. https://doi.org/10.1357/002224085788440402

Diaz, R. J., & Rosenberg, R. (1995). Marine benthic hypoxia: a review of its ecological effects and the behavioural responses of benthic macrofauna. *Oceanography and Marine Biology: An Annual Review. Vol. 33*, (May 2014), 245–303.

Egbert, G. D., & Erofeeva, S. Y. (2002). Efficient Inverse Modeling of Barotropic Ocean Tides. *Journal of Atmospheric and Oceanic Technology*, *19*(2), 183–204. https://doi.org/10.1175/1520-0426(2002)019<0183:EIMOBO>2.0.CO;2

Emery, W. J., & Thomson, R. E. (2004). *Data Analysis Methods in Physical Oceanography* (2nd ed.). Amsterdam: Elsevier.

Evans, W., Hales, B., Strutton, P. G., Shearman, R. K., & Barth, J. A. (2015). Failure to bloom: Intense upwelling results in negligible phytoplankton response and prolonged CO 2 outgassing over the Oregon shelf. *Journal of Geophysical Research: Oceans*, *120*(3), 1446–1461. https://doi.org/10.1002/2014JC010580

Feely, R. A., & Sabine, C. L. (2011). Carbon dioxide and hydrographic measurements during the 2007 NACP West Coast Cruise. Carbon Dioxide Information Analysis Center, Oak Ridge National Laboratory, US Department of Energy, Oak Ridge, Tennessee. https://doi.org/10.3334/CDIAC/otg.CLIVAR_NACP_West_Coast_Cruise_2007

Feely, R. A., Sabine, C. L., Hernandez-Ayon, J. M., Ianson, D., & Hales, B. (2008). Evidence for upwelling of corrosive "acidified" water onto the continental shelf. *Science (New York, N.Y.)*, *320*(5882), 1490–2. https://doi.org/10.1126/science.1155676

Fewings, M. R., Washburn, L., Dorman, C. E., Gotschalk, C., & Lombardo, K. (2016). Synoptic forcing of wind relaxations at Pt. Conception, California. *Journal of Geophysical Research: Oceans*, *121*(8), 5711–5730. https://doi.org/10.1002/2016JC011699

Freeland, H. J., & Denman, K. L. (1982). TOPOGRAPHICALLY CONTROLLED UPWELLING CENTER OFF SOUTHERN VANCOUVER ISLAND. *Journal of Marine Research*.

Freeland, H. J., & McIntosh, P. (1989). The vorticity balance on the southern British Columbia continental shelf. *Atmosphere - Ocean*, *27*(4), 643–657. https://doi.org/10.1080/07055900.1989.9649359

Freeland, H. J., Gatien, G., Huyer, A., & Smith, R. L. (2003). Cold halocline in the northern California Current: An invasion of subarctic water. *Geophysical Research Letters*, *30*(3), 1141. https://doi.org/10.1029/2002GL016663

Frolov, S., Ryan, J. P., & Chavez, F. P. (2012). Predicting euphotic-depth-integrated chlorophyll-a from discrete-depth and satellite-observable chlorophyll- a off central California. *Journal of Geophysical Research: Oceans*, *117*(C5), n/a-n/a. https://doi.org/10.1029/2011JC007322

Garcia, H. E., Boyer, T. P., Locarnini, R. A., Antonov, J. I., Mishonov, A. V, Baranova, O. K., et al. (2013). World Ocean Atlas 2013. Volume 3: dissolved oxygen, apparent oxygen utilization, and oxygen saturation. *NOAA Atlas NESDIS 75*, *3*(September), 27.

Giddings, S. N., MacCready, P., Hickey, B. M., Banas, N. S., Davis, K. A., Siedlecki, S. A., et al. (2014). Hindcasts of potential harmful algal bloom transport pathways on the Pacific Northwest coast. *Journal of Geophysical Research: Oceans*, *119*(4), 2439–2461. https://doi.org/10.1002/2013JC009622

Grantham, B. A., Chan, F., Nielsen, K. J., Fox, D. S., Barth, J. A., Huyer, A., et al. (2004). Upwelling-driven nearshore hypoxia signals ecosystem and oceanographic changes in the northeast Pacific. *Nature*, *429*(June), 749–754. https://doi.org/10.1038/nature02605

Gruber, N., Lachkar, Z., Frenzel, H., Marchesiello, P., Münnich, M., McWilliams, J. C., et al. (2011). Eddy-induced reduction of biological production in eastern boundary upwelling systems. *Nature Geoscience*, *4*(11), 787–792. https://doi.org/10.1038/ngeo1273

Hales, B., Moum, J. N., Covert, P., & Perlin, A. (2005). Irreversible nitrate fluxes due to turbulent mixing in a coastal upwelling system. *Journal of Geophysical Research*, *110*(C10), C10S11. https://doi.org/10.1029/2004JC002685

Harris, K. E., DeGrandpre, M. D., & Hales, B. (2013). Aragonite saturation state dynamics in a coastal upwelling zone. *Geophysical Research Letters*, *40*(11), 2720–2725. https://doi.org/10.1002/grl.50460

Hickey, B. M. (1979). The California current system-hypotheses and facts. *Progress in Oceanography*, *8*(4), 191–279. https://doi.org/10.1016/0079-6611(79)90002-8

Hickey, B. M. (1989). Patterns and Processes of Circulation over the Washington continental shelf and slope. In *Coastal Oceanography of Washington and Oregon* (pp. 41–115). Elsevier Science Publishers B.V.

Hickey, B. M. (1997). The Response of a Steep-Sided, Narrow Canyon to Time-Variable Wind Forcing. *Journal of Physical Oceanography*, *27*(5), 697–726. https://doi.org/10.1175/1520-0485(1997)027<0697:TROASS>2.0.CO;2

Hickey, B. M., & Banas, N. S. (2003). Oceanography of the U.S. Pacific Northwest Coastal Ocean and estuaries with application to coastal ecology. *Estuaries*, *26*(4), 1010–1031. https://doi.org/10.1007/BF02803360

Hickey, B. M., & Banas, N. S. (2008). Why is the Northern End of the California Current System So Productive ? *Oceanography*, *21*(4), 90–107.

Hickey, B. M., MacFadyen, A., Cochlan, W. P., Kudela, R. M., Bruland, K., & Trick, C. G. (2006). Evolution of chemical, biological, and physical water properties in the northern California Current in 2005: Remote or local wind forcing? *Geophysical Research Letters*, *33*(22), L22S02. https://doi.org/10.1029/2006GL026782

Hickey, B. M., Trainer, V. L., Michael Kosro, P., Adams, N. G., Connolly, T. P., Kachel, N. B., & Geier, S. L. (2013). A springtime source of toxic pseudo-nitzschia cells on razor clam beaches in the pacific northwest. *Harmful Algae*, *25*, 1–14. https://doi.org/10.1016/j.hal.2013.01.006

Hickey, B. M., Geier, S. L., Kachel, N. B., Ramp, S., Kosro, P. M., & Connolly, T. P. (2016). Alongcoast structure and interannual variability of seasonal midshelf water properties and velocity in the Northern California Current System. *Journal of Geophysical Research: Oceans*, *121*(10), 7408–7430. https://doi.org/10.1002/2015JC011424

Huntsman, S. A., & Barber, R. T. (1977). Primary production off northwest Africa: the relationship to wind and nutrient conditions. *Deep Sea Research*, *24*(1), 25–33. https://doi.org/10.1016/0146-6291(77)90538-0

Huyer, A. (1977). Seasonal variation in temperature , salinity , and density over the continental shelf off Oregon. *Limnology and Oceanography*, *22*, 442–453.

Huyer, A. (1983). Coastal upwelling in the California current system. *Progress in Oceanography*, *12*(3), 259–284. https://doi.org/10.1016/0079-6611(83)90010-1

Huyer, A. (2003). Preface to special section on enhanced Subarctic influence in the California Current, 2002. *Geophysical Research Letters*, *30*(15), 1–4. https://doi.org/10.1029/2003GL017724

Huyer, A., & Smith, R. L. (1985). The signature of El Niño off Oregon, 1982–1983. *Journal of Geophysical Research*, *90*(C4), 7133. https://doi.org/10.1029/JC090iC04p07133

Huyer, A., Fleischbein, J. H., Keister, J., Kosro, P. M., Perlin, N., Smith, R. L., & Wheeler, P. A. (2005). Two coastal upwelling domains in the northern California Current system. *Journal of Marine Research*, *63*(5), 901–929. https://doi.org/10.1357/002224005774464238

Jacox, M. G., Fiechter, J., Moore, A. M., & Edwards, C. A. (2015). ENSO and the California Current coastal upwelling response. *Journal of Geophysical Research: Oceans*, *120*(3), 1691–1702. https://doi.org/10.1002/2014JC010650

Jacox, M. G., Hazen, E. L., & Bograd, S. J. (2016). Optimal Environmental Conditions and Anomalous Ecosystem Responses: Constraining Bottom-up Controls of Phytoplankton Biomass in the California Current System. *Scientific Reports*, *6*(1), 27612. https://doi.org/10.1038/srep27612

Jacox, M. G., Edwards, C. A., Hazen, E. L., & Bograd, S. J. (2018). Coastal Upwelling Revisited: Ekman, Bakun, and Improved Upwelling Indices for the U.S. West Coast. *Journal of Geophysical Research: Oceans*, *123*(10), 7332–7350. https://doi.org/10.1029/2018JC014187

Kadko, D. C., Washburn, L., & Jones, B. (1991). Evidence of Subduction Within Cold Filaments of the Northern California Coastal Transition Zone. *Journal of Geophysical Research - Oceans*, *96*(C8), 14,909-14,926.

Kalnay, E., Kanamitsu, M., Kistler, R., Collins, W., Deaven, D., Gandin, L., et al. (1996). The NCEP/NCAR 40-Year Reanalysis Project. *Bulletin of the American Meteorological Society*, *77*(3), 437–471. https://doi.org/10.1175/1520-0477(1996)077<0437:TNYRP>2.0.CO;2

Keister, J. E., Di Lorenzo, E., Morgan, C. A., Combes, V., & Peterson, W. T. (2011). Zooplankton species composition is linked to ocean transport in the Northern California Current. *Global Change Biology*, *17*(7), 2498–2511. https://doi.org/10.1111/j.1365-2486.2010.02383.x

Kosro, P. M. (2002). A poleward jet and an equatorward undercurrent observed off Oregon and northern California, during the 1997-98 El Niño. *Progress in Oceanography*, *54*(1–4), 343–360. https://doi.org/10.1016/S0079-6611(02)00057-5

Kosro, P. M. (2003). Enhanced southward flow over the Oregon shelf in 2002: A conduit for subarctic water. *Geophysical Research Letters*, *30*(15), 10–13. https://doi.org/10.1029/2003GL017436

Kudela, R. M., Cochlan, W. P., Peterson, T. D., & Trick, C. G. (2006). Impacts on phytoplankton biomass and productivity in the Pacific Northwest during the warm ocean conditions of 2005. *Geophysical Research Letters*, *33*(22), L22S06. https://doi.org/10.1029/2006GL026772

Largier, J. L., Lawrence, C. A., Roughan, M., Kaplan, D. M., Dever, E. P., Dorman, C. E., et al. (2006). WEST: A northern California study of the role of wind-driven transport in the productivity of coastal plankton communities. *Deep Sea Research Part II: Topical Studies in Oceanography*, *53*(25–26), 2833–2849. https://doi.org/10.1016/j.dsr2.2006.08.018

Lathuilière, C., Echevin, V., Lévy, M., & Madec, G. (2010). On the role of the mesoscale circulation on an idealized coastal upwelling ecosystem. *Journal of Geophysical Research*, *115*(C9), C09018. https://doi.org/10.1029/2009JC005827

Lefebvre, K. A., Bargu, S., Kieckhefer, T., & Silver, M. W. (2002). From sanddabs to blue whales : the pervasiveness of domoic acid, *40*.

Lentz, S. J. (1992). The Surface Boundary Layer in Coastal Upwelling Regions. *Journal of Physical Oceanography*. https://doi.org/10.1175/1520-0485(1992)022<1517:TSBLIC>2.0.CO;2

Lentz, S. J., & Fewings, M. R. (2012). The Wind- and Wave-Driven Inner-Shelf Circulation. *Annual Review of Marine Science*, *4*(1), 317–343. https://doi.org/10.1146/annurev-marine-120709-142745

Lévy, M., Ferrari, R., Franks, P. J. S., Martin, A. P., & Rivière, P. (2012). Bringing physics to life at the submesoscale. *Geophysical Research Letters*, *39*(14), 1–14. https://doi.org/10.1029/2012GL052756

Di Lorenzo, E., Schneider, N., Cobb, K. M., Franks, P. J. S., Chhak, K., Miller, A. J., et al. (2008). North Pacific Gyre Oscillation links ocean climate and ecosystem change. *Geophysical Research Letters*, *35*(8), 2–7. https://doi.org/10.1029/2007GL032838

Di Lorenzo, E., Fiechter, J., Schneider, N., Braceo, A., Miller, A. J., Franks, P. J. S., et al. (2009). Nutrient and salinity decadal variations in the central and eastern North Pacific. *Geophysical Research Letters*, *36*(14), 2003–2008. https://doi.org/10.1029/2009GL038261

MacCready, P., Banas, N. S., Hickey, B. M., Dever, E. P., & Liu, Y. (2009). A model study of tide- and wind-induced mixing in the Columbia River Estuary and plume. *Continental Shelf Research*, *29*(1), 278–291. https://doi.org/10.1016/j.csr.2008.03.015

MacCready, P., McCabe, R. M., Siedlecki, S. A., Lorenz, M., Giddings, S. N., Bos, J., et al. (2020). Estuarine Circulation, Mixing, and Residence Times in the Salish Sea. *Journal of Geophysical Research - Oceans*.

MacFadyen, A., & Hickey, B. M. (2010). Generation and evolution of a topographically linked, mesoscale eddy under steady and variable wind-forcing. *Continental Shelf Research*, *30*(13), 1387–1402. https://doi.org/10.1016/j.csr.2010.04.001

MacFadyen, A., Hickey, B. M., & Foreman, M. G. G. (2005). Transport of surface waters from the Juan de Fuca eddy region to the Washington coast. *Continental Shelf Research*, *25*(16), 2008–2021. https://doi.org/10.1016/j.csr.2005.07.005

MacFadyen, A., Hickey, B. M., & Cochlan, W. P. (2008). Influences of the Juan de Fuca Eddy on circulation, nutrients, and phytoplankton production in the northern California Current System. *Journal of Geophysical Research*, *113*(C8), C08008. https://doi.org/10.1029/2007JC004412

Mass, C. F., Albright, M., Ovens, D., Steed, R., MacIver, M., Grimit, E., et al. (2003). Regional environmental prediction over the pacific nothwest. *Bulletin of the American Meteorological Society*, *84*(10), 1353-1366+1328. https://doi.org/10.1175/BAMS-84-10-1353

McCabe, R. M., Hickey, B. M., Dever, E. P., & MacCready, P. (2015). Seasonal Cross-Shelf Flow Structure , Upwelling Relaxation , and the Alongshelf Pressure Gradient in the Northern California Current System *. *American Meteorological Society*, *45*(1981), 209–227. https://doi.org/10.1175/JPO-D-14-0025.1

McCabe, R. M., Hickey, B. M., Kudela, R. M., Lefebvre, K. A., Adams, N. G., Bill, B. D., et al. (2016). An unprecedented coastwide toxic algal bloom linked to anomalous ocean conditions. *Geophysical Research Letters*, *43*(19), 10,366-10,376. https://doi.org/10.1002/2016GL070023

McKibben, S. M., Peterson, W., Wood, A. M., Trainer, V. L., Hunter, M., & White, A. E. (2017). Climatic regulation of the neurotoxin domoic acid. *Proceedings of the National Academy of Sciences*, *114*(2), 239–244. https://doi.org/10.1073/pnas.1606798114

McLaskey, A. K., Keister, J. E., McElhany, P., Olson, M. B., Busch, D. S., Maher, M., & Winans, A. K. (2016). Development of Euphausia pacifica (krill) larvae is impaired under pCO2 levels currently observed in the Northeast Pacific. *Marine Ecology Progress Series*, *555*, 65–78. https://doi.org/10.3354/meps11839

Meinvielle, M., & Johnson, G. C. (2013). Decadal water-property trends in the California Undercurrent, with implications for ocean acidification. *Journal of Geophysical Research: Oceans*, *118*(12), 6687–6703. https://doi.org/10.1002/2013JC009299

Metzger, J. E., Smedstad, O. M., Thoppil, P. G., Hurlburt, H. E., Cummings, J. A., Wallcraft, A. J., et al. (2014). US Navy Operational Global Ocean and Arctic Ice Prediction Systems. *Oceanography*, *27*(3), 32–43. https://doi.org/10.5670/oceanog.2014.66

National Marine Fisheries Service. (2017). *Fisheries of the United States, 2017 Report*. Retrieved from https://www.fisheries.noaa.gov/feature-story/fisheries-united-states-2017-report

Nelder, J. A., & Wedderburn, R. W. M. (1972). Generalized Linear Models. *Journal of the Royal Statistical Society. Series A (General)*, *135*(3), 370–384.

Noble, M., Jones, B., Hamilton, P., Xu, J., Robertson, G., Rosenfeld, L., & Largier, J. (2009). Cross-shelf transport into nearshore waters due to shoaling internal tides in San Pedro Bay, CA. *Continental Shelf Research*, *29*(15), 1768–1785. https://doi.org/10.1016/j.csr.2009.04.008

Pelland, N. A., Eriksen, C. C., & Lee, C. M. (2013). Subthermocline Eddies over the Washington Continental Slope as Observed by Seagliders, 2003–09. *Journal of Physical Oceanography*, *43*(10), 2025–2053. https://doi.org/10.1175/JPO-D-12-086.1

Peterson, J. O., Morgan, C. A., Peterson, W. T., & Di Lorenzo, E. (2013). Seasonal and interannual variation in the extent of hypoxia in the northern California Current from 1998–2012. *Limnology and Oceanography*, *58*(6), 2279–2292. https://doi.org/10.4319/lo.2013.58.6.2279

Pierce, S. D., Smith, R. L., Kosro, P. M., Barth, J. A., & Wilson, C. D. (2000). Continuity of the poleward undercurrent along the eastern boundary of the mid-latitude north Pacific. *Deep Sea Research Part II: Topical Studies in Oceanography*, *47*(5–6), 811–829. https://doi.org/10.1016/S0967-0645(99)00128-9

Pierce, S. D., Barth, J. A., Thomas, R. E., & Fleischer, G. W. (2006). Anomalously warm July 2005 in the northern California Current: Historical context and the significance of cumulative wind stress. *Geophysical Research Letters*, *33*(22), L22S04. https://doi.org/10.1029/2006GL027149

Pierce, S. D., Barth, J. A., Shearman, R. K., & Erofeev, A. Y. (2012). Declining Oxygen in the Northeast Pacific. *Journal of Physical Oceanography*, *42*(3), 495–501. https://doi.org/10.1175/JPO-D-11-0170.1

Pitcher, G. C., Figueiras, F. G., Hickey, B. M., & Moita, M. T. (2010). The physical oceanography of upwelling systems and the development of harmful algal blooms. *Progress in Oceanography*, *85*(1–2), 5–32. https://doi.org/10.1016/j.pocean.2010.02.002

Ribal, A., & Young, I. R. (2020). Calibration and cross validation of global ocean wind speed based on scatterometer observations. *Journal of Atmospheric and Oceanic Technology*, *37*(2), 279–297. https://doi.org/10.1175/JTECH-D-19-0119.1

Ritzman, J., Brodbeck, A., Brostrom, S., McGrew, S., Dreyer, S., Klinger, T., & Moore, S. K. (2018). Economic and sociocultural impacts of fisheries closures in two fishing-dependent communities following the massive 2015 U.S. West Coast harmful algal bloom. *Harmful Algae*, *80*(August), 35–45. https://doi.org/10.1016/j.hal.2018.09.002

Rivas, D., & Samelson, R. M. (2011). A Numerical Modeling Study of the Upwelling Source Waters along the Oregon Coast during 2005. *Journal of Physical Oceanography*, *41*(1), 88–112. https://doi.org/10.1175/2010JPO4327.1

Rossi, V., López, C., Sudre, J., Hernández-García, E., & Garçon, V. (2008). Comparative study of mixing and biological activity of the Benguela and Canary upwelling systems. *Geophysical Research Letters*, *35*(11), 1–5. https://doi.org/10.1029/2008GL033610

Rossi, V., López, C., Hernández-García, E., Sudre, J., Garcon, V. C., & Morel, Y. G. (2009). Surface mixing and biological activity in the four Eastern Boundary Upwelling Systems. *Nonlinear Processes in Geophysics*, *16*(4), 557–568. https://doi.org/10.5194/npg-16-557-2009

Ruzicka, J. J., Brink, K. H., Gifford, D. J., & Bahr, F. (2016). A physically coupled end-to-end model platform for coastal ecosystems: Simulating the effects of climate change and changing upwelling characteristics on the Northern California Current ecosystem. *Ecological Modelling*, *331*, 86–99. https://doi.org/10.1016/j.ecolmodel.2016.01.018

Rykaczewski, R. R., & Checkley, D. M. (2008). Influence of ocean winds on the pelagic ecosystem in upwelling regions. *Proceedings of the National Academy of Sciences*, *105*(6), 1965–1970. https://doi.org/10.1073/pnas.0711777105

Schwing, F. B., O'Farrel, M., Steger, J. M., & Baltz, K. (1996). Coastal Upwelling Indices, West Coast of North America, 1946-1995. *NOAA Technical Memorandum NMFS-SWFSC-231*, *671*, 1–45.

Schwing, F. B., Murphree, T., DeWitt, L., & Green, P. M. (2002). The evolution of oceanic and atmospheric anomalies in the northeast Pacific during the El Niño and La Niña events of 1995–2001. *Progress in Oceanography*, *54*(1–4), 459–491. https://doi.org/10.1016/S0079-6611(02)00064-2

Shchepetkin, A. F., & McWilliams, J. C. (2005). The regional oceanic modeling system (ROMS): a split-explicit, free-surface, topography-following-coordinate oceanic model. *Ocean Modelling*, *9*(4), 347–404. https://doi.org/10.1016/j.ocemod.2004.08.002

Siedlecki, S. A., Banas, N. S., Davis, K. A., Giddings, S. N., Hickey, B. M., MacCready, P., et al. (2015). Seasonal and interannual oxygen variability on the Washington and Oregon continental shelves. *Journal of Geophysical Research: Oceans*, *120*(2), 608–633. https://doi.org/10.1002/2014JC010254

Smith, S. D. (1988). Coefficients for sea surface wind stress, heat flux, and wind profiles as a function of wind speed and temperature. *Journal of Geophysical Research*, *93*(C12), 15467. https://doi.org/10.1029/JC093iC12p15467

Stone, H. B., Banas, N. S., & MacCready, P. (2018). The Effect of Alongcoast Advection on Pacific Northwest Shelf and Slope Water Properties in Relation to Upwelling Variability. *Journal of Geophysical Research: Oceans*, *123*(1), 265–286. https://doi.org/10.1002/2017JC013174

Strub, P. T., Kosro, P. M., & Huyer, A. (1991). The nature of the cold filaments in the California Current system. *Journal of Geophysical Research*, *96*(C8), 14743. https://doi.org/10.1029/91JC01024

Sutherland, D. A., MacCready, P., Banas, N. S., & Smedstad, L. F. (2011). A Model Study of the Salish Sea Estuarine Circulation. *Journal Of Physical Oceanography*, *41*(6), 1125–1143. https://doi.org/10.1175/2011JPO4540.1

Thomson, R. E., & Krassovski, M. V. (2010). Poleward reach of the California Undercurrent extension. *Journal of Geophysical Research*, *115*(C9), C09027. https://doi.org/10.1029/2010JC006280

Tinis, S. W., Thomson, R. E., Mass, C. F., & Hickey, B. M. (2006). Comparison of MM5 and meteorological buoy winds from British Columbia to Northern California. *Atmosphere-Ocean*, *44*(1), 65–81. https://doi.org/10.3137/ao.440105

Trainer, V. L., Adams, N. G., Bill, B. D., Stehr, C. M., Wekell, J. C., Moeller, P., et al. (2000). Domoic acid production near California coastal upwelling zones, June 1998. *Limnology and Oceanography*, *45*(8), 1818–1833. https://doi.org/10.4319/lo.2000.45.8.1818

Trainer, V. L., Hickey, B. M., & Horner, R. A. (2002). Biological and physical dynamics of domoic acid production off the Washington coast. *Limnology and Oceanography*, *47*(5), 1438–1446.

Trainer, V. L., Hickey, B. M., Lessard, E. J., Cochlan, W. P., Trick, C. G., Wells, M. L., et al. (2009). Variability of Pseudo-nitzschia and domoic acid in the Juan de Fuca eddy region and its adjacent shelves. *Limnology and Oceanography*, *54*(1), 289–308. https://doi.org/10.4319/lo.2009.54.1.0289

Trainer, V. L., Bates, S. S., Lundholm, N., Thessen, A. E., Cochlan, W. P., Adams, N. G., & Trick, C. G. (2012). Pseudo-nitzschia physiological ecology, phylogeny, toxicity, monitoring and impacts on ecosystem health. *Harmful Algae*, *14*, 271–300. https://doi.org/10.1016/j.hal.2011.10.025

Visser, A. (1997). Using random walk models to simulate the vertical distribution of particles in a turbulent water column. *Marine Ecology Progress Series*, *158*, 275–281. https://doi.org/10.3354/meps158275

Ware, D. M. (1992). Production characteristics of upwelling systems and the trophodynamic role of hake. *South African Journal of Marine Science*, *12*(1), 501–513. https://doi.org/10.2989/02577619209504721

Ware, D. M., & Thomson, R. E. (2005). Bottom-Up Ecosystem Trophic Dynamics Determine Fish Production in the Northeast Pacific. *Science*, *308*(5726), 1280–1284. https://doi.org/10.1126/science.1109049

Wilkerson, F. P., Lassiter, A. M., Dugdale, R. C., Marchi, A., & Hogue, V. E. (2006). The phytoplankton bloom response to wind events and upwelled nutrients during the CoOP WEST study. *Deep Sea Research Part II: Topical Studies in Oceanography*, *53*(25–26), 3023–3048. https://doi.org/10.1016/j.dsr2.2006.07.007

Willmott, C. J. (1982). Some Comments on the Evaluation of Model Performance. *Bulletin of the American Meteorological Society*, *63*, 1309–1313. https://doi.org/10.1175/1520-0477(1982)063<1309:SCOTEO>2.0.CO;2

Yokomizo, H., Botsford, L. W., Holland, M. D., Lawrence, C. A., & Hastings, A. (2010). Optimal wind patterns for biological production in shelf ecosystems driven by coastal upwelling. *Theoretical Ecology*, *3*(1), 53–63. https://doi.org/10.1007/s12080-009-0053-5

VITA

Hally B. Stone grew up outside of Buffalo, NY. After graduating from Williamsville South High School in 2007, she attended Boston University to study Astronomy & Physics, where she became interested in oceanography. She graduated with a B.A. in Astronomy & Physics and Marine Science in 2011. After working a few different jobs in Boston, MA, she decided to apply to graduate school to study coastal oceanography and moved to Seattle, WA to attend the University of Washington in 2013. While in graduate school, she became interested in science policy through her involvement in the UW's Integrative Graduate Education and Research Traineeship (IGERT) Program on Ocean Change. In addition to her interest in coastal upwelling dynamics and in science policy, Hally enjoys baking pies, cooking with her partner Garrett, hiking with her dog Peppa, and hanging out with her cat Benji.